ABSTRACT

MEHTA, YASH. Manipulating Light-Matter Interaction in Organic Small Molecules and Hybrid Organic-Inorganic Perovskites (Under the direction of Dr. Franky So).

Light emission in semiconducting material remains a technologically relevant field of study after J. C. Maxwell laid down the mathematical formalism unifying classical electromagnetism and its interaction with matter in the early 1860s. Since then, there have been groundbreaking developments to the framework resulting in unification of the quantum mechanics with electromagnetism into quantum electrodynamics (QED). This newfound understanding has shed light on photon-photon and photon-matter scattering, quantum entanglement, and non-classical light sources. In this dissertation, I study both traditional and well understood optoelectronic devices like OLEDs (organic light emitting diodes), perovskite-based lasers, along with incipient phenomena like cooperative emission in perovskites based on their light emission mechanism.

OLEDs are representative p-n diodes consisting of organic material sandwiched between two electrodes on either end. When current is injected through the electrodes they propagate through the layers and eventually undergo radiative recombination at the emissive layer. The radiative charge recombination is governed by spontaneous emission process and emits lambertian light which is used extensively in solid-state lighting fixtures and handheld displays. A developing area of application has been for near-eye display like V/R and A/R glasses which requires light emission along certain directions while suppression in other. To achieve this, we used diffractive optical elements integrated into the device structure to demonstrate directional and polarized light emission. By selectively extracting the TE mode which is optimized for high intensity and simultaneously suppressing other modes by tuning the layer thickness, the farfield emission pattern

was shown to have a low beam divergence of $\sim 4^{\circ}$ with an external quantum efficiency (EQE) of 7%. To our knowledge this was the first ever demonstration of such a device architecture.

Next, I studied how the stimulated emission process in perovskite lasers can be optimized for greater amplification efficiency through optical cavity redesign. Metal halide perovskites (MHP) are versatile, solution-processed materials with high internal quantum efficiency (IQE), optical gain, and light emission properties identical to traditional inorganic semiconductors making them appealing for laser applications. However traditional solution-processed lasing devices rely on a single cavity architecture for optical feedback. In this work we combined a 2^{nd} order distributed feedback (DFB) cavity with a transverse Fabry-Pérot cavity – hereafter referred to as a Hybrid cavity – to demonstrate a low threshold multimode lasing device in the visible spectrum. The DFB serves as the primary oscillatory feedback element while for the Fabry-Pérot cavity a thin silver mirror is fabricated at the interface between the glass substrate and the perovskite gain medium. On comparing the amplified spontaneous emission (ASE) property of the conventional structure with the hybrid structure a noticeable improvement was observed. The threshold fluence for the ASE peak was more than halved from 36.9 $\mu J.cm^{-2}$ to 17.5 $\mu J.cm^{-2}$ which was attributed to the increased photon density of states (PDOS) in the hybrid cavity and a concurrent longer cavity photon lifetime of 62 fs compared to only 27 fs in the conventional cavity as evident from the slope efficiency in the ASE input-output curve.

Eventually, I study non-classical Superfluorescent light emission in MHP. Superfluorescence is an ultrafast burst of coherent light resulting from intricate dipole-dipole correlations. The system of individual emitters develops a macroscopic dipole moment over a finite delay time with a common phase making it coherent and distinct from spontaneous and stimulated emission. However, due to the stochastic origin of the dipole synchronization process

the characteristic timescales, namely the delay time and the pulse width, are random limiting its potential for novel applications. To overcome this, we encapsulated the perovskite material in a low-Q cavity and by tuning the cavity resonance with respect to the material resonance we show a deterministic control over the light-matter interaction strength as evident from the ultrafast time-resolved study. We demonstrated statistical control over the time dynamics with the delay time having a variability from 7.5 ps to 9.1 ps while the pulse width having a variability from 3.6 ps to 4 ps for the planar reference sample and the on-resonant sample respectively at threshold fluence. Additionally, by modeling the pulse broadening effect of the cavity we extrapolated the group delay dispersion (GDD) value for perovskites which is a critical parameter for soliton propagation in an optical communication network.

Manipulating Light-Matter Interaction in Organic Small Molecules and Hybrid Organic-Inorganic Perovskites

by
Yash Mehta

A dissertation submitted to the Graduate Faculty of
North Carolina State University
in partial fulfillment of the
requirements for the degree of
Doctor of Philosophy

Material Science and Engineering

Raleigh, North Carolina
2024

APPROVED BY:

Franky So Committee Chair	Joseph Tracy
Kenan Gundogdu	Yin Liu

DEDICATION

This dissertation is dedicated to my family for their unconditional love and support.

BIOGRAPHY

Yash Mehta was born in Mumbai, India. He completed his B.E. in Instrumentation Engineering from Mumbai University and was always passionate about physics and math, but it was during his BE years that he decided to pursue physics. He enrolled in the physics program at Appalachian State University, North Carolina as a M.S. student. While taking physics coursework he joined Prof. Francois Amet's lab where he worked on the intersection of superconductivity and the Quantum Hall effect in Josephson junctions based on graphene heterostructures. He then joined North Carolina State University in 2018 as a doctorate student in the Materials Science and Engineering dept. and eventually Prof. So's group in the Fall of 2019. His research focused on optical characterization of organic optoelectronic devices and halide perovskite films.

When not in the lab, you will find him at one of the several greenways in the area either taking a walk or running. He rediscovered his love for football (people here called it soccer, don't understand the logic there, but anyway) and joined a recreational soccer team where he connected with people from all backgrounds at NCSU. Recently, reading books related to human ontology and philosophy in general has been his favorite pastime.

ACKNOWLEDGMENTS

First and foremost, I would like to express my heartfelt gratitude to my mentor, Prof. Franky So, for his continuous support throughout my time at NCSU. Over the past five years, I was always inspired by his immense breadth of knowledge in several research areas and his internal drive to constantly learn new things. I, for the most part of my PhD journey, was free to work on problems that interested me which is quite a luxury and would like to thank him for this opportunity and his patience and encouragement throughout the process. I refer to him as a mentor rather than an academic advisor is because I learned a lot of other important life lessons from him. His advice to remain flexible in selecting a professional career has been one of the most important takeaway for me. I would also like to thank Prof. Francois Amet, my master's research advisor, for his guidance and from whom I learned the rigors of physics and math. Next, I would like to thank the group's previous postdocs Xiangyu Fu, Liping Zhu, and Carr Ho for their guidance through the initial years of my PhD. Current and past group members Neha, Rui, Shichen (Mason), Yusen, Jingshan, Yusuf, Apurva, Qi, Lei, Stephen, Hossein, Hamna, Dong-Hun, Mona, Emory, and Yashas with whom I have had all kinds of discussions (and sometimes fights) spanning the spectrum from intellectual to stupid making the journey that much more enjoyable and worthwhile. I also want to thank my colleagues Gamze, Melike, and Seyitliyev for educating me on optical setups and allowing me to share their labspace.

I am also grateful to Prof. Joseph Tracy, Prof. Kenan Gundogdu, and Prof. Yin Liu for serving as my committee members and advisors and providing me with valuable insights to carry my research forward. I would like to especially thank Prof. Gundogdu for his guidance throughout the PhD process.

TABLE OF CONTENTS

LIST OF TABLES

LIST OF FIGURES

CHAPTER 1: Fundamentals of light emission in organics and perovskites

Certain sections of this chapter are excerpts based on previously published results:

Moon, J., Mehta, Y., Gundogdu, K., So, F., Gu, Q., Metal-Halide Perovskite Lasers: Cavity Formation and Emission Characteristics. Adv. Mater. 2023, 2211284. https://doi.org/10.1002/adma.202211284

In this chapter we will introduce the material properties of metal halide perovskite (MHP) and organic small molecules that make them appealing for light emitting applications. We also discuss the different regimes of light radiation and highlight the distinctions between them.

1.1. Organic light emitting diode (OLED)

OLEDs are made from π-conjugated small molecules with sp^2 hybridization with the remaining delocalized p-orbital electrons responsible for electrical conduction.[1] These small molecules can be thermally evaporated which allows for intricate device stacks and separation of layers based on their functions for instance transport layer, blocking layer, injection layer, and so on as seen in a representative schematic in Figure 1.1. The injected carriers from the end electrodes (holes through the anode and electrons through the cathode) hop through the layers and form excitons in the emitting layer (EML) which eventually spontaneously recombine to generate photons. Owing to the layered heterostructure design and the difference in relative permittivity of the medium, a portion of the emitted light is trapped inside the device while the remaining travels outside the device forming a solid angle of emission resulting in a Lambertian profile. The figure of merit to quantify the outcoupled light to the number of injected charges in the device is given by the external quantum efficiency (EQE).

The efficiency and lifetime of OLEDs have increased steadily over the past three decades after the first promising demonstration by Tang and VanSlyke.[2] The industrial success of OLED in the display and solid-state lighting is already well documented and building on the technological maturity a new application area is being envisaged: virtual and augmented reality display. Depending on the face from which the light exits the device we either have back-emitting OLED (BEOLEDs) or top-emitting OLED (TEOLEDs) where the former is preferred for lighting fixtures and the latter for display applications.

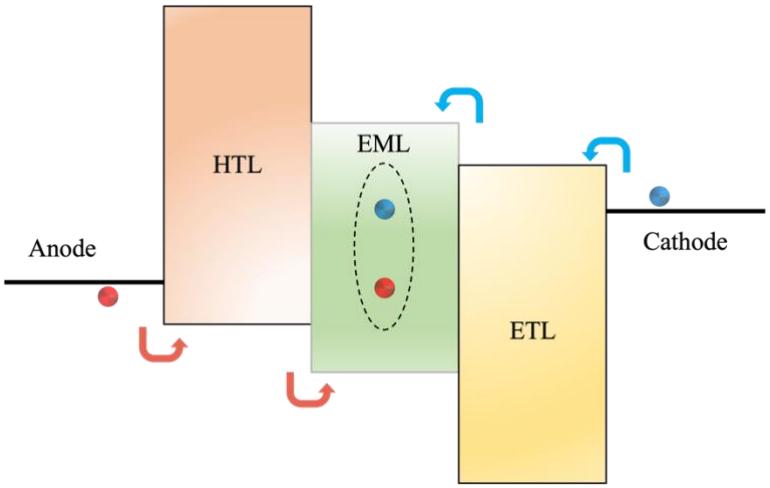

Figure 1.1: Charge transport and recombination in band-aligned OLED heterostructure.

1.1.1. Spontaneous emission

The physical picture of light emission in OLED architecture corresponds to an oscillating dipole in a weak Fabry-Pérot due to the surrounding reflective electrodes. Depending on the spin state of the recombining charges it can either be fast fluorescent emission from singlet states or relatively slow phosphorescent emission from triplets. Though the spin-selection rules are important, generally the probability of transition can be described by Fermi's Golden rule,

$$\Gamma_{if} = \frac{2\pi}{\hbar} |\langle g|d.E|e\rangle|^2 \rho$$

where d is the dipole moment operator, E is the electric field strength and ρ is the density of states. The formula represents the probability of an excited state $|e\rangle$ to relax radiatively to the ground state $|g\rangle$ driven by reservoir electric field and the material's dipole moment dependent on the density of available states (DOS) at the concerned energy levels. Coincidentally, A. Einstein in 1917 derived a fundamental relation for optical transition based on simple differential equations to account for the state population in a two-level system, equivalent to Fermi's Golden rule, and showed that the spontaneous emission probability is exactly equal to the absorption probability except for a minus sign indicating the direction of the process.

Despite the almost unity internal quantum efficiency (IQE) of current fluorescent and phosphorescent material that rely on maximizing the spontaneous emission probability, there are still open challenges that need to be solved one of which is improving the light outcoupling efficiency and wavefront control which is critical for near-eye display (NED) technology. This thesis will focus on making use of nanostructures to redistribute the trapped light energy inside one of the several multilayers in OLED to useful leaky modes that can be extracted as useful radiation. Additionally, the use of integrated diffractive nonstructural elements allows for wavefront shaping which would otherwise require bulky optical components outside the OLED pixel adding to the weight and design complication for virtual/augmented reality glass and near-eye display technology.

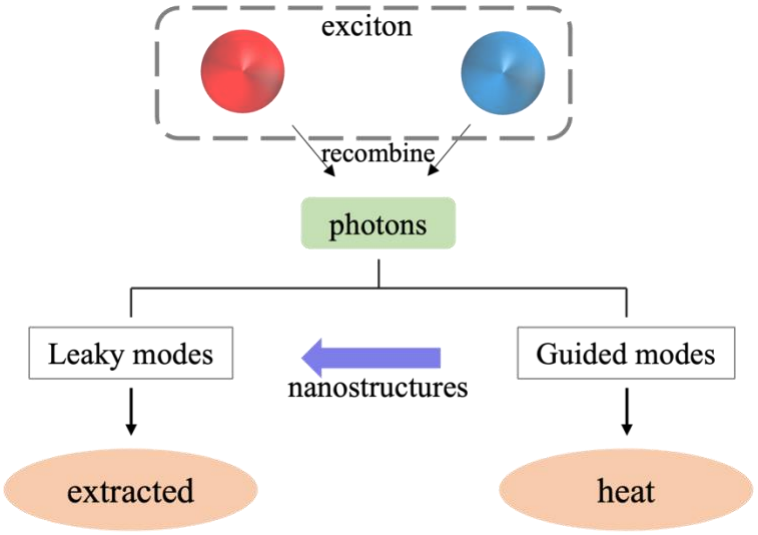

Figure 1.2: Exciton recombination can be either radiative or non-radiative. The radiative pathway can be further divided into leaky mode and guided modes which, if not extracted, can result in heating losses. Using a well parameterized nanostructure at the right interface can convert some of the guided modes to leaky modes which eventually escapes the device as useful light radiation. After extraction guided modes retain their wavevector information which can be useful for beam shaping applications.

1.2. Metal Halide Perovskite (MHP)

Hybrid metal-halide perovskites (MHPs) have shown remarkable optoelectronic properties as well as facile and cost-effective processability. With the success of MHP solar cells and light-emitting diodes, they have also exhibited great potential as gain media for on-chip lasers. The family of perovskites has a stoichiometry of ABX_3, consisting of a network of corner-sharing BX_6 octahedra (Figure 1.3). 'A' and 'B' refer to cations, and 'X' refers to an anion. The Goldschmidt's tolerance factor (t) and the octahedral factor (μ) describe the stability of crystal structures of different sizes and charges of ions. By controlling compositions in the ABX_3 stoichiometry, bandgap tuning over the visible and near-IR spectral ranges — regions that are most suitable for

photovoltaic and light emitting devices — can be easily achieved. MHPs also has a long carrier diffusion length and a long carrier lifetime for efficient solar cells, as well as high color purity, high brightness, and a narrow emission peak for applications in LEDs and lasers.[3,4] In addition to MHPs, low-dimensional metal halides have also attracted considerable attention for LEDs and lasers due to their better humidity stability.[5]

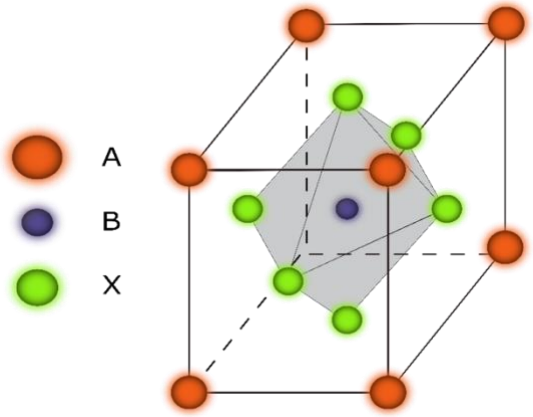

Figure 1.3: Schematic of the octahedral geometry of metal halide perovskite with ABX_3 stoichiometry. Due to the soft and dynamic lattice, perovskites are prone to undergo phase transition from cubic to tetragonal and to orthorhombic as temperature decreases.

Despite the significant progress in the growth of single-crystal MHP, spin-coated polycrystal MHP films are still widely used as the gain medium in MHP lasers because of ease of fabrication, and the quick turnaround time for device prototyping. Moreover, the fact that single-mode lasers generally require thickness in the range of 100 to 300 nm ($\geq \lambda/(2n_{eff})$), and for emission wavelength λ in the range of 405 to 1080 nm, the effective refractive index of the cavity mode n_{eff} is usually close to the refractive index of MHP of ~2.[6] Making thin single crystalline MHP of less than 300 nm is extremely challenging, whereas making thin spincoated MHP films is relatively easier due to the wide degree of processing conditions.

Since the crystal quality, fabrication methods, and the optical environment can affect the emission characteristics of perovskites, it is essential to distinguish between different emission regimes. Depending on the nature of the light-matter interaction and the dipole-dipole correlation strength, the emission can either display spontaneous emission, amplified spontaneous emission (ASE), stimulated emission, or superfluorescence (SF) behavior. Next, we present a simple dipole model that qualitatively determines the emission mechanism.

1.3. Verification of emission behavior in MHP thin films

Because the crystal quality and fabrication methods affect the emission characteristics of laser cavities, as discussed in the previous sections, it is essential to study how to verify laser emission from MHP laser cavities and how the emission differs from amplified spontaneous emission (ASE) from MHP thin films without a cavity. Depending on the nature of the light-matter interaction, the emission can either display the more commonly observed spontaneous emission, amplified spontaneous emission, stimulated emission, and superfluorescence (SF) emission due to macroscopic quantum phase transition. Here, we present a simple dipole model that qualitatively determines the emission mechanism, then show examples of each type of emission in MHP thin films and cavities.

1.3.1. Dipole model

In semiconductor gain materials, excited electron-hole pairs can emit photons that differ in their characteristics depending on the initial preparation conditions, external perturbations, the phase of the dipoles, and the ambient environment, among other factors. In general, most of the steady-state characteristics of an emitter can be understood from the classical dipole oscillator model, as its behavior is like an atom if one does not consider material complications such as lattice

interaction. The classical Equation of motion for a dipole in a periodic quadratic potential V is given by[7]

$$m\ddot{\mu}(t) = -\gamma\dot{\mu}(t) - K\mu + e^2\mathcal{E}(t) \quad (1)$$

where m and $\mu(t)$ is the dipole mass and displacement respectively, γ is the damping coefficient, K is the constant of the restoring force, and $\mathcal{E}(t)$ is the magnitude of an externally applied electric field. Simplifying this expression by using the oscillator's natural resonance frequency $\omega_a = \sqrt{k/m}$ with k being the wave number, and solving for the dipole displacement $\mu(t)$ results in

$$\mu(t) = \mu(t_o)\exp\left[-\frac{\gamma}{2}(t - t_o) + j\omega_a'(t - t_o) + j\phi_o\right] \quad (2)$$

The natural frequency ω_a gets modified by the damping from inter-particle and lattice interactions, resulting in $\omega_a' = \sqrt{\omega_a^2 - \left(\frac{\gamma}{2}\right)^2}$, with ϕ_o being the phase of the dipole at time t_o.

If we assume that all N dipoles oscillate unperturbed and in phase with each other, the macroscopic polarization of the gain medium $p(t)$ can be obtained by summing over all individual dipoles labeled by index i,

$$p(t) = V^{-1}\sum_{i=1}^{NV}\mu_i(t) = N\mu(t_o)\exp\left[-\frac{\gamma}{2}(t - t_o) + j\omega_a'(t - t_o) + j\phi_o\right] \quad (3)$$

Because of the physical proximity and in-phase oscillations of dipoles, the net polarization of the system gets amplified, leading to a coherently oscillating system with the same phase and radiating energy proportional to $|N\mu_o|^2$, and hence proportional to N^2 – a consequence of the formation of a coherent macroscopic polarization and a signature of coherent cooperative emission.

Unfortunately, perturbations are pervasive and distort the phase evolution of the dipoles, which impedes the formation of a coherent macroscopic polarization. The most prominent type of

perturbation is scattering or collision among dipoles. Other forms of perturbations include doppler dephasing due to the distribution of the velocity of particles exhibiting Brownian motion and thermal vibration which changes the interparticle distances thereby changing the resonance frequency ω_a'. As a result, the initial phase ϕ_o now gets scrambled on a local scale with each of these dephasing events, leading to an attenuation of the macroscopic polarization. After a time period *t* that is longer than the characteristic dephasing time T_2 , the mean value of the dipole displacement becomes zero, i.e., $\langle \sum_i^N \mu(t) \rangle = 0$ and the macroscopic polarization is completely lost. In this case, each dipole oscillates individually and with no phase relationship with each other (i.e., random phases), radiating energy $N|\mu_o|^2$ which is the well-known spontaneous emission, and it differs from cooperative emission by an amplifying factor N instead of N^2. From this, we can conclude that for cooperative effects to be dominant and manifest themselves in the system the population evolution should be faster than the dephasing time, which we will discuss in more detail in Section 1.3.4.

With T_2 describing the characteristic time of dephasing events in a homogeneous medium (T_2^* for an inhomogeneous medium), the population dynamics for the decaying dipoles can be written as[8]

$$\dot{N} = -N(t)/T_2 \tag{4}$$

whose solution is,

$$N(t) = N_o \exp\left(-\frac{t - t_o}{T_2}\right) \tag{5}$$

resulting in a macroscopic polarization

$$p(t) = N_o \mu(t_o) \exp\left[\left(-\frac{\gamma}{2} + \frac{1}{T_2}\right)(t - t_o) + j\omega_a'(t - t_o) + j\phi_o\right] \tag{6}$$

We can therefore confer that the amplitude of the decay rate of a dipole now gets modulated by dephasing events as $(-\gamma/2 + 1/T_2)$. This expression is also then the homogenous linewidth of the dipole transition – a consequence of Fourier transforming from the time domain to the frequency domain. Compared to Equation 3, the dephasing events cause the decay of macroscopic polarization much more rapidly, resulting in a loss of coherence.

Three emission processes that have unique spectral features are ASE, stimulated emission, and superfluorescence. ASE and superfluorescence are both spontaneous emission processes, with the level of dipole coherence distinguishing the two phenomena. Meanwhile, stimulated emission is a coherent amplification process that typically requires an external optical cavity. In the following, we describe their similarities and differences, and how each process can be experimentally verified.

1.3.2. Amplified Spontaneous emission (ASE)

Spontaneous emission is the only optical process that doesn't require the presence of a photon in the initial state and is inherently stochastic in nature. Materials with large optical gain can achieve population inversion and amplify the spontaneously emitted radiation even without a resonant cavity, resulting in a quasi-coherent beam referred to as ASE.[9–11] For example, spontaneously emitted photons can induce more spontaneous emission from the population inverted dipoles when propagating through MHP gain medium in a single pass in a thin film configuration.[7]

Compared to spontaneous emission-dominated PL, ASE has a higher peak intensity and narrower linewidth (Figure 1.4a-left) and is more directional with moderate spatial coherence. Emission directionality is a consequence of amplification along the light propagation axis of the gain media. The medium then acts as an aperture diffracting light in a cone shape over a solid

angle $\theta = a/L$ (Figure 1.4b). The level of ASE from thin films can be directly correlated with the material gain coefficient; ASE can thus provide insight into the amplifying ability of the gain medium.[12] Regarding spectral features, ASE manifests as a narrowband Gaussian lineshape compared to the wideband Gaussian lineshape of spontaneous emission. In MHP, ASE can be as narrow as a few nanometers, while spontaneous emission is tens of nanometers in linewidth.[13,14]

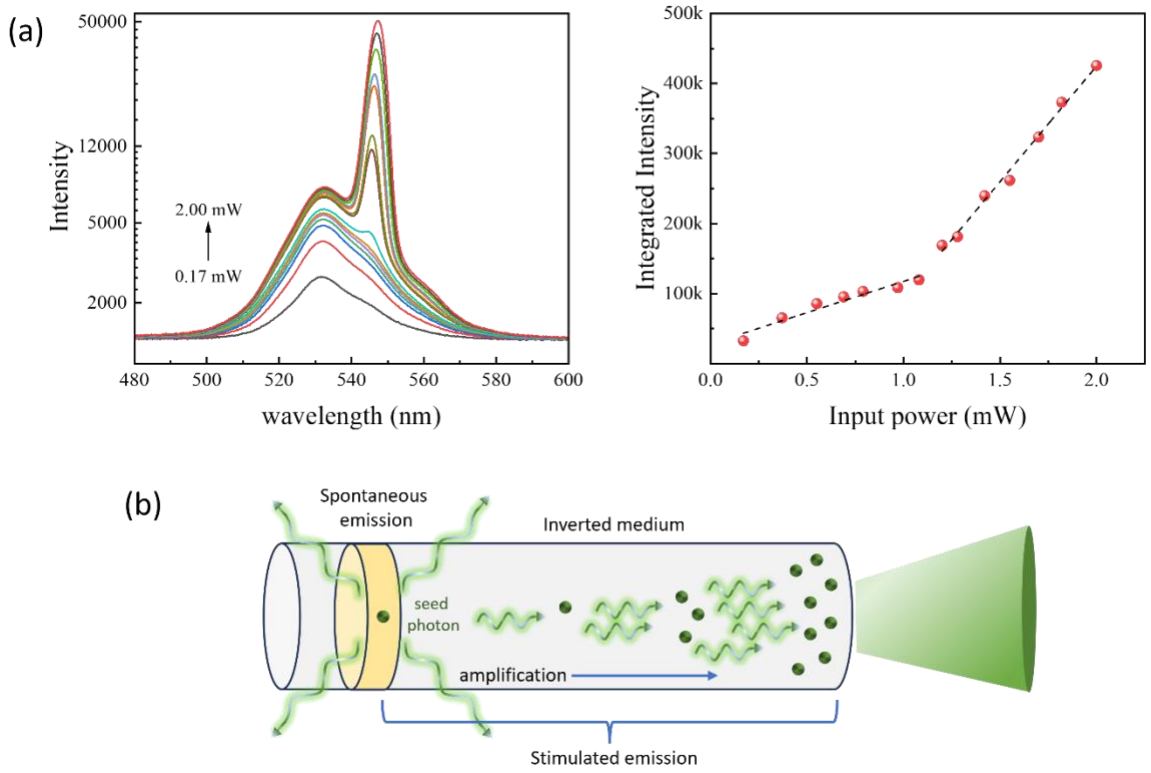

Figure 1.4: (a) PL spectrum of an oriented quasi-2D $CsPbBr_3$ film as a function of the excitation fluence showing the evolution from the broadband PL to the narrowband ASE (left). L-L curve with a kink indicates the ASE onset threshold (right). (b) Emission cone for ASE resulting in directional emission.

The intensity of ASE strongly depends on the excitation spot size and shape.[9,15] In thin films, ASE grows with the length of the excited gain medium L as $I \propto e^{(\alpha L)}$, where α is the optical

gain coefficient. The optical gain of MHP can be measured via the variable stripe method. [16] Using the waveguide mode of MHP thin films, optical gain is determined by $I(L) = \frac{\Omega}{\alpha}\left(e^{(\alpha L)} - 1\right)$ where Ω is a proportionality parameter that contains information about the photophysical property of the active region. Depending on the type/quality of MHP films and measurement conditions (e.g., temperature and pulse width), gain values of 12 – 3200 cm^{-1} have been reported from MHP thin films.[17–22]

At low excitation densities, spontaneous emission is dominant; at high excitation densities approaching the ASE threshold, the material loss is fully compensated by gain leading to amplified emission over a narrow spectral region of the PL spectrum. The light input – light output (light-light) curve shows a "kink", signifying the ASE threshold as seen in Figure 1.4a-right. ASE has many features similar to lasing -- like threshold behavior, linewidth narrowing, and spatial coherence. However, due to the lack of optical feedback, ASE lacks temporal coherence and presents an intermediate stage between an incoherent spontaneously emitting thermal source and a coherent laser source.[15,23]

1.3.3. Stimulated emission

In a resonant cavity at high pumping levels, the dipole population in the gain material becomes inverted, and an incoming photon stimulates the excited dipoles to coherently emit a photon cascading into an amplification process. Unlike spontaneous emission in which emitted photons have different phases, electronic dipoles are excited by photons of the same wavelength in lasing. The emitted photons thus retain their temporal and phase information of the excitation photon. Typical features of lasing include narrow emission linewidth, a threshold behavior (a "kink") in the light-light curve, emission directionality, and good spatial coherence. Figure 1.5a shows a cross-sectional SEM image and emission characteristics of a DFB laser with quasi-2D

$(PEA)_2FA_{n-1}Pb_nBr_{3n+1}$ dissolved in NMP as the gain medium. The quasi-2D DFB laser exhibits narrow linewidth (Figure 1.5b), TE-polarized nature of emission (Figure 1.5b-inset), threshold behavior (Figure 1.5c), and far-field interference pattern of the DFB laser with a bright central fringe (Figure 1.5c-inset), which are indicative of lasing.

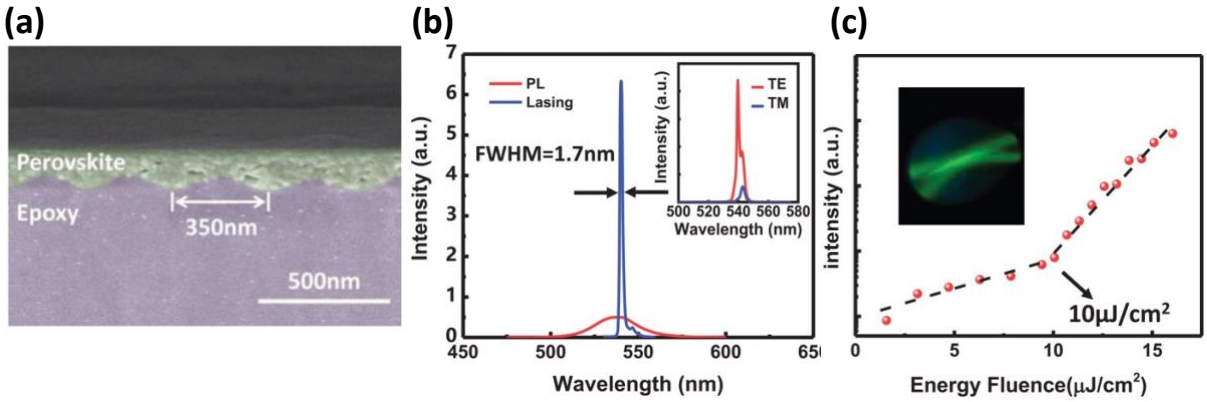

Figure 1.5: (a) Cross-sectional SEM of 1D sinusoidal DFB grating with solution-processed MHP. (b) The broad PL spectrum is shown in red, and the narrow lasing transition is shown in blue with an FWHM of 1.7 nm; the inset shows the TE-polarized nature of the laser emission. (c) The integrated intensity with a distinct "kink" indicates lasing onset at a lasing threshold of 10 μJ/cm^2; the inset shows the far-field interference pattern, showing spatial coherence of the emission. (a)–(c) Reproduced with permission.[11] Copyright 2020, Wiley-VCH.

In the last two decades, advancements in nanofabrication and the incorporation of metal into laser cavity design have allowed the realization of subwavelength-sized lasers, i.e., nanolasers.[24] Nanolasers feature small mode volumes and moderate Q factors, and several perovskite nanolasers have been demonstrated.[25–27] Because of the small cavity size, a nanolaser can support only a few resonant modes in the spectral window of gain. As a result, the spontaneous emission factor β (the fraction of spontaneous emission channeled into the lasing mode) can be high. In the case that only one resonant mode is supported, a unity β can be achieved. While high-

β is generally desired due to the efficient channeling of spontaneous emission into the lasing mode, the distinction between lasing from ASE and even spontaneous emission becomes even more complex.[28] As depicted in Figure 1.6a, as β increases from the typical 1×10^{-3} in micro-scale lasers to near unity in nanolasers, the "kink" in the current-in light-out curve that signifies the lasing threshold gets diminished. In addition, the emission linewidth does not approach the Schawlow-Townes limit.[29,30] Such high-β lasers are controversially termed thresholdless lasers due to the lack of a "kink" feature in the light-light curve and the lack of linewidth narrowing in spectral evolution.[31] Nevertheless, these peculiar emission features make the distinction between spontaneous and stimulated emission more ambiguous.

Due to many similar features between ASE and lasing, such as threshold behavior, linewidth narrowing, polarization, and spatial coherence, there is skepticism when distinguishing between these two. However, the difference between ASE and lasing originates from the feedback mechanism provided by the optical cavity that produces a high Q-factor and allows for stronger light-matter interaction. In 2009, Samuel and colleagues proposed to address the uncertainty in determining lasing with a list of experiments, which has now become the standard checklist to confirm lasing.[32] Lasers will in general 1) have a spectrally narrow emission linewidth, usually below a few nanometers; 2) have spatial coherence in the form of a diffraction-limited collimated beam; 3) exhibit a threshold behavior wherein after a certain excitation fluence, the emission grows exponentially which is accompanied by linewidth narrowing. This exponential rise should be consistent with the value of the optical gain of the medium, the cavity length, and the excitation spot size to rule out other effects. However, some authors claim that the above-listed signatures are still inconclusive to prove lasing behavior.[33,34]

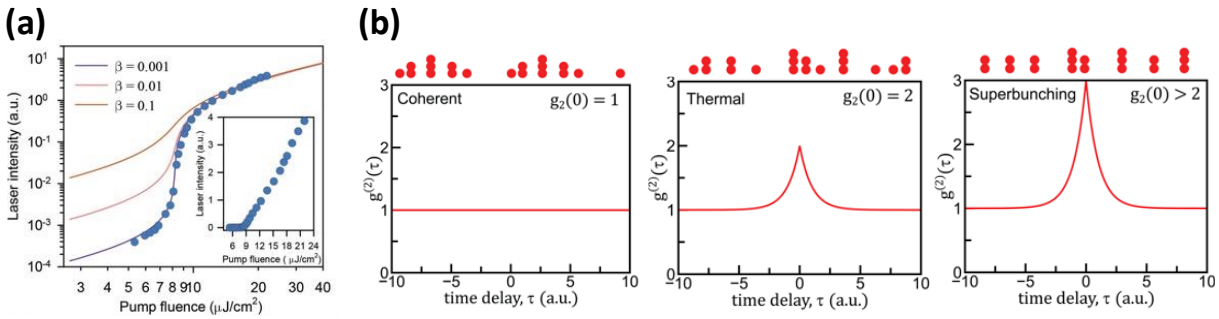

Figure 1.6: (a) L-L curve showing the "kink" feature vanishing with increasing β value. a) Reproduced with permission.[35] Copyright 2017, Wiley-VCH. (b) $g^{(2)}$ value at zero-time delay for coherent lasing emission, thermal emission, and superbunching emission respectively. The top of each figure is a graphical representation of the photon arrival time, highlighting the statistical nature of the emission. b) Reproduced with permission.[36] Copyright 2021, Wiley-VCH.

Measurement of the second-order intensity correlation function of emission

$$g^{(2)}(\tau) = \frac{\langle I(t)I(t+\tau)\rangle}{\langle I(t)\rangle\langle I(t+\tau)\rangle}$$

is a more definitive way to confirm lasing or the lack thereof, as it relies on principles of photon statistics which is unique for each emission mechanism. τ is the delay time between the field intensities measured at a common incident plane and the $\langle\cdot\rangle$ indicates the time average. It is a way of quantizing photon coincidence events as a function of delayed time measurement since intensity *I* in the above expression can be replaced by the photon number *n* since the two are directly related. The corresponding interference experiments gives direct access to the photon statistic of the source under consideration. For a perfectly coherent emission, the mean photon variance follows a Poisson distribution. For different emission mechanisms, the photon variance is modified by an intensity fluctuating term which is a measure of the overlap between adjacent photon wave packets.

It is known that incoherent light sources exhibit intensity fluctuations, which lead to a photon bunching peak in $g^2(\tau)$ near zero-time delay (i.e., $|\tau| \approx 0$), namely, $g^{(2)}(0) > 1$. For instance, Figure 1.6(b) shows $g^{(2)}(t)$ from different emission mechanisms. Stimulated emission from lasers follows Poisson statistics, implying that the variance is equal to the mean in the absence of fluctuations, such that $g^{(2)}(0) = 1$ and therefore, photons do not bunch.[37,38] $g^{(2)}(0) = 2$ is for an ideal thermal source such as a perfect black body emitter with a representation of bunching photon wave packets. For light sources in which spontaneous emission dominates, $1 < g^{(2)}(0) < 2$ highlights the thermal origins of such radiation.[37,38] Meanwhile, for cooperative emission processes like superfluorescence, photons can exhibit superbunching, leading to $g^{(2)}(0) > 2$, where the fluctuating term has a dominant contribution to the mean photon number. The experimental setup to measure the second-order intensity correlation $g^2(\tau)$ is the well-known Hanbury Brown and Twiss interferometer. However, due to the limited temporal resolution of the detectors compared to the emission linewidth of nano- and micro-scale light sources, such measurements are often difficult to perform and analyze.[39,40]

On a fundamental level, the "nature" of light emission can be classified based on the degree of coherence or correlation functions as mentioned before. There are several orders to this function but the most referred to in literature are the 1st and the 2nd order correlation functions or the field and intensity correlation function respectively. The fluctuations are based on the statistical properties of light sources which can be different among different mechanisms. One can intuitively understand this when comparing the transmission of light through a 50-50 beam-splitter as shown in Figure 1.7.

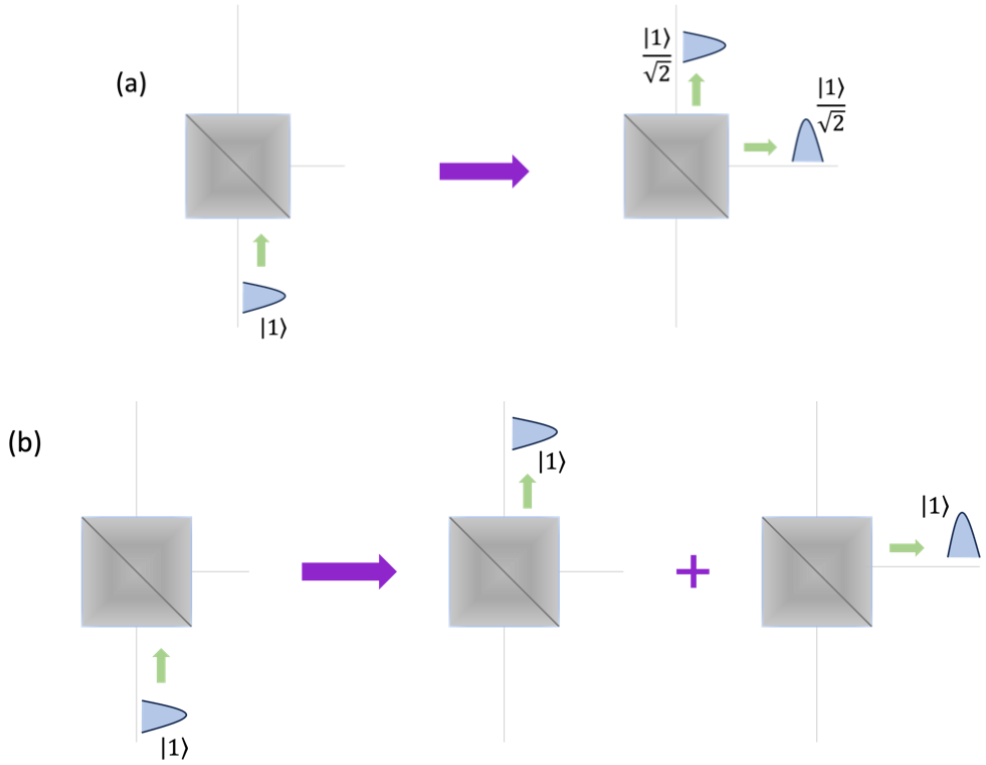

Figure 1.7: Transmission through a 50% beam splitter (a) classical coherent light source from a laser being split with equal probability in both output arms. (b) a non-classical light source consisting of a single photon being split with an equal probability of two superposition states.

1.3.4. Superfluorescence emission

As seen from the above dipole model, cooperative effects can have a measurable effect on the emission characteristics. Initially, an excited dipole population has a random phase distribution. As the dipoles begin to relax radiatively, vacuum field fluctuations cause phase synchronization of these dipole oscillators, and after a characteristic delay time (τ_D), the ensemble of dipoles becomes phase-locked, and the system transitions into the Dicke Superradiant state.[41] In this coherent state, the ensemble collectively acts like a "giant dipole" and interacts with the radiation field, emitting a high-intensity short burst of photons (Figure 1.8a). This phase transition of an

ensemble of incoherent dipoles into a coherent macroscopic quantum state and its collective radiation is called superfluorescence.

Because the dipoles are in phase, the superfluorescence intensity $I \propto N^2$, with N being the number of participating dipoles. Superfluorescence by nature is an ultra-short pulse with a characteristic pulse width τ_p which is several times smaller than the pulse width of an ensemble of N incoherent dipoles emitting simultaneously (Figure 1.8b). Therefore, the entire emission intensity is concentrated in an intense short burst, causing the population to deplete completely with a characteristic decay time of $\tau_R = 8\pi\tau_{SP}/3\rho\lambda^2 L$ where τ_{SP} is the single dipole spontaneous emission decay time, ρ is the density of participating dipoles, and L is the gain media length. Additionally, a certain density of dipoles is required for them to undergo cooperative emission. An expression for this critical density was later derived by Arecchi-Courtens et al.[42] and is labeled as the cooperation number, given by

$$N_c = 8\pi c T_1 A/3\lambda^2 L$$

where A is the cross-sectional area of the excited region and T_1 is the inverse of Einstein A coefficient, and L is the length over which the interaction happens. The cooperation number was later verified experimentally.[43,44]

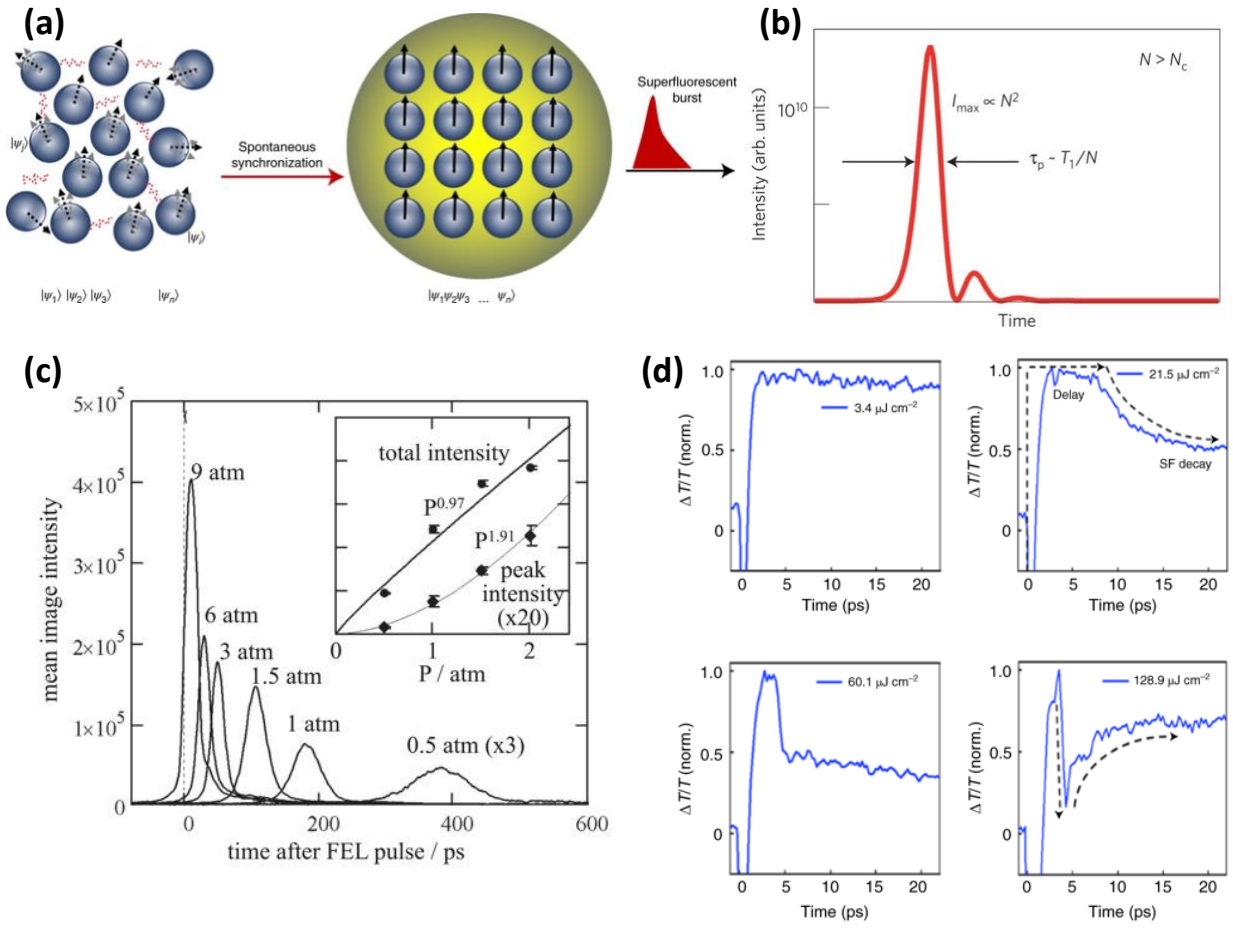

Figure 1.8: (a) Dipole-dipole correlation leading to a macroscopic coherent dipole that relaxes by emitting an intense superfluorescence burst. (a) Reproduced with permission.[45] Copyright 2021, Nature Portfolio. (b) Characteristic superfluorescence features include high intensity, extremely fast decay rate, and ringing. (b) Reproduced with permission.[46] Copyright 2012, Nature Portfolio. (c) Time-delayed nature of superfluorescence in Helium gas. (c) Reproduced with permission.[47] Copyright 2011, American Physical Society. (d) Transient absorption spectroscopy to measure the population dynamics of the tetragonal domains in MAPbI3 at 78 K. (d) Reproduced with permission.[45] Copyright 2021, Nature Portfolio.

One can distinguish between superfluorescence and other emission processes based on the time dynamics. As mentioned in Section 1.3.1, dephasing events can hamper the buildup of a

macroscopic polarization. As a result, superfluorescence occurs when the dephasing time T_2 for a homogeneous medium is longer than the characteristic time scale for superfluorescence. More precisely, the regime of $T_2 \gg (\tau_R \tau_D)^{0.5}$ corresponds to superfluorescence while the regime of $\tau_R < T_2 < (\tau_R \tau_D)^{0.5}$ is characteristic of ASE as predicted by Schuurmans and Polder.[48,49] Furthermore, the transition from superfluorescence to ASE was experimentally observed by Malcuit et al.,[50] in a KCl:O_2^- system. Since the dephasing rate is proportional to the third power of temperature, the authors swept the temperature from 10 K (superfluorescence is the dominant emission mechanism) to 27 K (the system completely transitions to ASE), with 23 K being the critical transition temperature. Temperature influences whether the emission is superfluorescence because dephasing time T_2 decreases with increasing temperature, thus affecting the comparison between T_2 and $(\tau_R \tau_D)^{0.5}$. Another such experimental observation from ASE to superfluorescence was recorded using an ultrafast streak camera in a system consisting of Li vapors.[51] The transition was controlled by varying the active atomic number density undergoing the emission process. Superfluorescence has many characteristics similar to ASE and lasing, such as narrow linewidth, high intensity, and directionality. Therefore, to confirm superfluorescence, unique features of superfluorescence, such as delay time τ_D needs to be measured. Figure 1.8c shows time-resolved PL spectroscopy results that show delayed superfluorescence in Helium gas at different gas pressures, which plots the integrated pulse intensity as a function of the superfluorescence pulse arrival time, with *t=0* being the excitation reference. At higher gas pressures, due to the faster dipole synchronization, the emitted light shows earlier time delays and narrower temporal linewidths, which is a distinct feature of superfluorescence. Because of the delay with characteristic time τ_D, the superfluorescence signal rises later than PL, which is an instant process. In addition to time-resolved PL spectroscopy, transient absorption spectroscopy can also be used

to track ultrafast dynamics, which can distinguish superfluorescence from other emission mechanisms. In a study by Maki et al.,[49] an expression for the ensembled averaged time-dependent intensity was provided, which consists of contributions from both ASE and superfluorescence. In fact, a similar expression was given by Haake et al. for an inhomogeneously broadened medium.[52] According to the expression, for different time scales, different terms are dominant and are characterized by either ASE or superfluorescent behavior. The time scales correlate with the dephasing time T_2 and the characteristic superfluorescence time τ_R and τ_D as mentioned earlier. There have also been a few reports of superfluorescence in halide perovskites,[45,53,54] some even at room temperature.[55] Biliroglu and Findik et. al. observed superfluorescence in $MAPbI_3$ thin films at 78 K and later in quasi-2D PEA:$CsPbBr_3$ films at room temperature.[45,55] Their results clearly show signatures of superfluorescence, including delay time, enhanced intensity, extremely fast decay rate and Burnham-Chiao ringing. Furthermore, the authors used transient absorption spectroscopy to analyze the carrier population dynamics in tetragonal domains of $MAPbI_3$ at 77 K as shown in Figure 1.88d. At the threshold fluence, the dynamics changes from a monotonically exponential decay — a characteristic of PL emission — to an abrupt decay after a certain waiting time corresponding to the delay time τ_D. After the sudden drop in carrier population, an intense burst of light follows. This intense burst of light is called superfluorescence.

Another way to ascertain superfluorescence is through the intensity correlation function. $g^{(2)}(0) > 1$[56,57] in superfluorescence because of photon bunching, which originates from the correlation among the different emitters in the same macroscopic coherent state. Therefore, it depends on the number of emitters in proximity. Raino et al.[54] measured the second-order correlation function in a superlattice of $CsPbBr_3$ nanocrystals at 4 K and found that due to correlated emission, $g^{(2)}(0) > 1$, showing bunching of photons. In the meantime, some

extremely well-correlated regions in the superlattice had $g^{(2)}(0) \approx 3$, showing photon super-bunching. For further verification, the authors measured $g^{(1)}$ correlation function using a Michaelson interferometer and were able to extract the phase coherence time. For uncoupled QDs, the coherence time was about 38 fs; for coupled QDs, the phase coherence time increases by $\sim$4 times, reaching 140 fs.

1.4. Conclusion

In this chapter we looked at the material properties of small molecules and perovskite that determine the light-emitting behavior. The dominant radiative mechanism in OLEDs is spontaneous light emission driven by recombing Frenkel-type excitons. By modeling the emission of a dipole as a simple harmonic motion we were able to qualitatively distinguish between individual and cooperative effects in light emission. We also discussed the various degrees of coherence that can be achieved in perovskite based on the optical environment and the strength of the light and matter interaction and concluded that based on the quantitative 2nd order correlation functions a definite distinction can be made between stimulated emission, amplified spontaneous emission and superfluorescent emission along with other time-resolved characteristic signature.

1.5. References

1. Martin Pope & Charles E. Swenberg. *Electronic Processes in Organic Crystals and Polymers*. (Oxford University Press, 1999).

2. Tang, C. W. & VanSlyke, S. A. Organic electroluminescent diodes. *Appl Phys Lett* **51**, 913–915 (1987).

3. Kim, J. Y., Lee, J. W., Jung, H. S., Shin, H. & Park, N. G. High-Efficiency Perovskite Solar Cells. *Chem Rev* **120**, 7867–7918 (2020).

4. Lei, L., Dong, Q., Gundogdu, K. & So, F. Metal Halide Perovskites for Laser Applications. *Adv Funct Mater* **31**, 1–21 (2021).

5. Akkerman, Q. A. & Manna, L. What Defines a Halide Perovskite? *ACS Energy Lett* 604–610 (2020) doi:10.1021/acsenergylett.0c00039.

6. Gholipour, S. & Saliba, M. *Bandgap tuning and compositional exchange for lead halide perovskite materials*. *Characterization Techniques for Perovskite Solar Cell Materials* (Elsevier Inc., 2019). doi:10.1016/B978-0-12-814727-6.00001-3.

7. Siegman, A. E. *Lasers*. *Lasers* (University Science Books, 1986).

8. Skinner, J. L. & Hsu, D. Pure dephasing of a two-level system. *Journal of physical chemistry (1952)* **90**, 4931–4938 (1986).

9. Cho, C. *et al.* Controlling and Optimizing Amplified Spontaneous Emission in Perovskites. *ACS Appl Mater Interfaces* **12**, 35242–35249 (2020).

10. Brenner, P. *et al.* Continuous wave amplified spontaneous emission in phase-stable lead halide perovskites. *Nat Commun* **10**, 1–7 (2019).

11. Lei, L. *et al.* Efficient Energy Funneling in Quasi-2D Perovskites: From Light Emission to Lasing. *Advanced materials (Weinheim)* **32**, e1906571-n/a (2020).

12. Milanese, S. *et al.* Amplified Spontaneous Emission Threshold Dependence on Determination Method in Dye-Doped Polymer and Lead Halide Perovskite Waveguides. *Molecules* **27**, 4261 (2022).

13. Muniz-Cánovas, P., Barmenkov, Y. O., Kir'yanov, A. v, Cruz, J. L. & Andrés, M. v. ASE narrow-band noise pulsing in erbium-doped fiber amplifier and its effect on self-phase modulation. *Opt Express* **27**, 8520–8528 (2019).

14. Donati, S. & Giuliani, G. Noise in an optical amplifier: formulation of a new semiclassical model. *IEEE J Quantum Electron* **33**, 1481–1488 (1997).

15. Peters, G. I. & Allen, L. Amplified spontaneous emission I. The threshold condition. *Journal of Physics A: General Physics* **4**, 238–243 (1971).

16. Shaklee, K. L. & Leheny, R. F. DIRECT DETERMINATION OF OPTICAL GAIN IN SEMICONDUCTOR CRYSTALS. **475**, 1–4 (2015).

17. Xing, G. *et al.* Low-temperature solution-processed wavelength-tunable perovskites for lasing. *Nat Mater* **13**, 476–480 (2014).

18. Sutherland, B. R. *et al.* Conformal Organohalide Perovskites Enable Lasing on Spherical Resonators. 10947–10952 (2014).

19. D'Innocenzo, V., Srimath Kandada, A. R., de Bastiani, M., Gandini, M. & Petrozza, A. Tuning the light emission properties by band gap engineering in hybrid lead halide perovskite. *J Am Chem Soc* **136**, 17730–17733 (2014).

20. Yakunin, S. *et al.* Low-threshold amplified spontaneous emission and lasing from colloidal nanocrystals of caesium lead halide perovskites. *Nat Commun* **6**, 1–8 (2015).

21. Li, M. *et al.* High Optical Gain of Solution-Processed Mixed-Cation CsPbBr3 Thin Films towards Enhanced Amplified Spontaneous Emission. *Adv Funct Mater* **31**, 1–8 (2021).

22. Sutherland, B. R. *et al.* Perovskite thin films via atomic layer deposition. *Advanced Materials* **27**, 53–58 (2015).

23. Allen, L. & Peters, G. I. Amplified spontaneous emission III. Intensity and saturation. *Journal of Physics A: General Physics* **4**, 564–573 (1971).

24. Gu, Q. & Fainman, Y. *Semiconductor Nanolasers*. (Cambridge University Press, 2017).

25. Wang, K., Wang, S., Xiao, S. & Song, Q. Recent Advances in Perovskite Micro- and Nanolasers. *Adv Opt Mater* **6**, 1–27 (2018).

26. Cho, S., Yang, Y., Soljačić, M. & Yun, S. H. Submicrometer perovskite plasmonic lasers at room temperature. *Sci Adv* **7**, (2021).

27. Huang, C. *et al.* Formation of Lead Halide Perovskite Based Plasmonic Nanolasers and Nanolaser Arrays by Tailoring the Substrate. *ACS Nano* **12**, 3865–3874 (2018).

28. Ning, C. Z. What is Laser Threshold? *IEEE journal of selected topics in quantum electronics* **19**, 1503604 (2013).

29. Schawlow, A. L. & Townes, C. H. Infrared and Optical Masers. *Physical review* **112**, 1940–1949 (1958).

30. Mohideen, U., Slusher, R. E., Jahnke, F. & Koch, S. W. Semiconductor microlaser linewidths. *Phys Rev Lett* **73**, 1785–1788 (1994).

31. YOKOYAMA, H. Physics and Device Applications of Optical Microcavities. *Science (American Association for the Advancement of Science)* **256**, 66–70 (1992).

32. Samuel, I. D. W. W., Namdas, E. B. & Turnbull, G. A. How to recognize lasing. *Nat Photonics* **3**, 546–549 (2009).

33. Ryglowski, L., Cyprych, K. & Mysliwiec, J. The differentiation procedure between amplified spontaneous emission and lasing phenomena. *Opt Commun* **510**, 127939- (2022).

34. Vallés-Pelarda, M. *et al.* High Optical Performance of Cyan-Emissive CsPbBr3 Perovskite Quantum Dots Embedded in Molecular Organogels. *Adv Opt Mater* **9**, (2021).

35. Chen, S., Zhang, C., Lee, J., Han, J. & Nurmikko, A. High-Q, Low-Threshold Monolithic Perovskite Thin-Film Vertical-Cavity Lasers. *Advanced Materials* **29**, (2017).

36. Wang, Z. *et al.* Optically Driven Giant Superbunching from a Single Perovskite Quantum Dot. *Adv Opt Mater* **9**, 2100879 (2021).

37. Choi, Y.-S. *et al.* Evolution of the onset of coherence in a family of photonic crystal nanolasers. *Appl Phys Lett* **91**, 31108- (2007).

38. Chow, W. W., Jahnke, F. & Gies, C. Emission properties of nanolasers during the transition to lasing. *Light Sci Appl* **3**, e201–e201 (2014).

39. Hayenga, W. E. *et al.* Second-order coherence properties of metallic nanolasers. *Optica* **3**, 1187- (2016).

40. Pan, S. H., Gu, Q., el Amili, A., Vallini, F. & Fainman, Y. Dynamic hysteresis in a coherent high-β nanolaser. *Optica* **3**, 1260- (2016).

41. Scully, M. O. & Svidzinsky, A. A. The Super of Superradiance. *Science (American Association for the Advancement of Science)* **325**, 1510–1511 (2009).

42. Arecchi, F. T. & Courtens, E. Cooperative Phenomena in Resonant Electromagnetic Propagation. *Phys Rev A (Coll Park)* **2**, 1730–1737 (1970).

43. Kumarakrishnan, A. & Han, X. L. Superfluorescence from optically trapped calcium atoms. *Phys Rev A* **58**, 4153–4162 (1998).

44. Kumarakrishnan, A., Chudasama, S. & Han, X. Collision-induced superfluorescence. *J Opt Soc Am B* **22**, 1538- (2005).

45. Findik, G. *et al.* High-temperature superfluorescence in methyl ammonium lead iodide. *Nat Photonics* **15**, 676–680 (2021).

46. Timothy Noe II, G. *et al.* Giant superfluorescent bursts from a semiconductor magneto-plasma. *Nat Phys* **8**, 219–224 (2012).

47. Nagasono, M. *et al.* Observation of free-electron-laser-induced collective spontaneous emission (superfluorescence). *Phys Rev Lett* **107**, 193603 (2011).

48. Schuurmans, M. F. H. & Polder, D. Superfluorescence and amplified spontaneous emission: A unified theory. *Phys Lett A* **72**, 306–308 (1979).

49. Maki, J. J., Malcuit, M. S., Raymer, M. G., Boyd, R. W. & Drummond, P. D. Influence of collisional dephasing processes on superfluorescence. *Phys Rev A (Coll Park)* **40**, 5135–5142 (1989).

50. MALCUIT, M. S., MAKI, J. J., SIMKIN, D. J. & BOYD, R. W. Transition from superfluorescence to amplified spontaneous emission. *Phys Rev Lett* **59**, 1189–1192 (1987).

51. Okada, J., Ikeda, K. & Matsuoka, M. Streak camera investigation of superradiance development. *Opt Commun* **27**, 321–323 (1978).

52. Haake, F., Haus, J., King, H., Schröder, G. & Glauber, R. Delay-Time Statistics and Inhomogeneous Line Broadening in Superfluorescence. *Phys Rev Lett* **45**, 558–561 (1980).

53. Zhong, Y. *et al.* Ultrafast Optical Properties of Cavity-Enhanced Superfluorescence. *Adv Opt Mater* **10**, 2102290-n/a (2022).

54. Rainò, G. *et al.* Superfluorescence from lead halide perovskite quantum dot superlattices. *Nature (London)* **563**, 671–675 (2018).

55. Biliroglu, M. *et al.* Room-temperature superfluorescence in hybrid perovskites and its origins. *Nat Photonics* **16**, 324–329 (2022).

56. Dicke, R. H. Coherence in Spontaneous Radiation Processes. *Physical review* **93**, 99–110 (1954).

57. Leymann, H. A. M., Foerster, A., Jahnke, F., Wiersig, J. & Gies, C. Sub- and Superradiance in Nanolasers. *Phys Rev Appl* **4**, (2015).

CHAPTER 2: Directional Polarized Light Emission from Thin-Film Light-Emitting Diodes

The chapter is an excerpt based on our previously published results:

Fu, X., Mehta, Y., Chen, Y.-A., Lei, L., Zhu, L., Barange, N., Dong, Q., Yin, S., Mendes, J., He, S., Gogusetti, R., Chang, C.-H., So, F., Directional Polarized Light Emission from Thin-Film Light-Emitting Diodes. *Adv. Mater.* 2021, 33, 2006801. https://doi.org/10.1002/adma.202006801

The initial device idea presented here was conceived by Dr. Xiangyu Fu. I performed the FDTD simulation for different grating pitch and layer thicknesses for optimized OLED design. Based on the simulation results I fabricated the OLED device and performed angle-resolved electroluminescence spectroscopy (ARES) for the green emitter. I have trimmed the publication to only include the OLED device concept and demonstration for which I was a part of.

2.1. Introduction

Light emitting diodes (LEDs) with directional and polarized light emission have many photonic applications, and beam shaping of these devices is fundamentally challenging because they are Lambertian light sources. In this work, using organic LEDs (OLEDs) for demonstrations, by selectively diffracting the TE waveguide mode while suppressing other optical modes in a nanostructured LED, we first demonstrated highly directional light emission from a full-area organic LED with a small divergence angle less than 3°, and a TE to TM polarization extinction ratio of 13. The highly selective diffraction of only the TE waveguide mode is possible due to the planarization of the device stack by thermal evaporation and solution processing.

With the rapid growth in portable displays, thin-film light emitting diodes (LEDs) have attracted great attention due to their low fabrication cost and high efficiency compared with inorganic LED and liquid crystal display. Typical thin-film LEDs are less than two hundred

nanometers in thickness, consisting of an indium tin oxide (ITO) anode, hole and electron transport layers, an emitting layer, and a metal cathode. Depending on the emitting material, thin-film LEDs can be categorized into organic LEDs (OLEDs),[1] polymer LEDs (PLEDs),[2] quantum dot LEDs (QLEDs) [3] and perovskite LEDs (PeLEDs).[4]

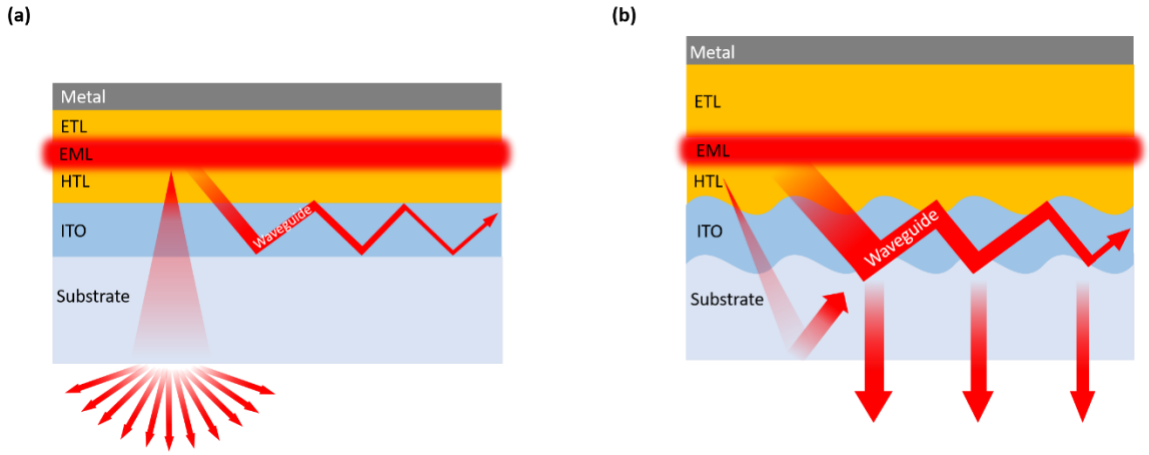

Figure 2.1: (a) A conventional thin-film LED with a Lambertian air mode emission profile. (b) A waveguide emission thin-film LED emitting directional light by suppressing the air mode and extracting the waveguide mode.

A thin-film LED stack forms a microcavity between a metal electrode and an ITO anode (Figure 2.1a). Usually the cavity length of the device is optimized to achieve a maximum light outcoupling efficiency, resulting in a Lambertian-like air mode emission profile due to the weak cavity effects.[5] Controlling the emission profile of a thin-film LED is desirable for many applications and is referred to as beam-shaping.[6] In particular, highly directional beam shapes lead to many interesting applications in solid-state lighting,[7] stereoscopic displays,[8] holographic displays,[9] optical communication[10,11] and integrated lasers.[12]

In recent years, near-eye displays such as virtual reality (VR) and augmented reality (AR) have gained great momentum in various applications.[13] Despite the rapid progress, VR displays

are often bulky and heavy due to the light collimating refractive lenses.[14] In contrast, AR displays use micro-displays and waveguide optical components to project the images which leads to a smaller form factor. However, the throughput from the input-output diffractive/holographic components are only 10%, resulting in an overall outcoupling efficiency less than 2%.[15] One way to improve both AR and VR displays is to use image sources with directional light emission (Figure 2.2). This eliminates the need for light collimator or optical combiners, thus reducing the display size while improving the outcoupling efficiency.

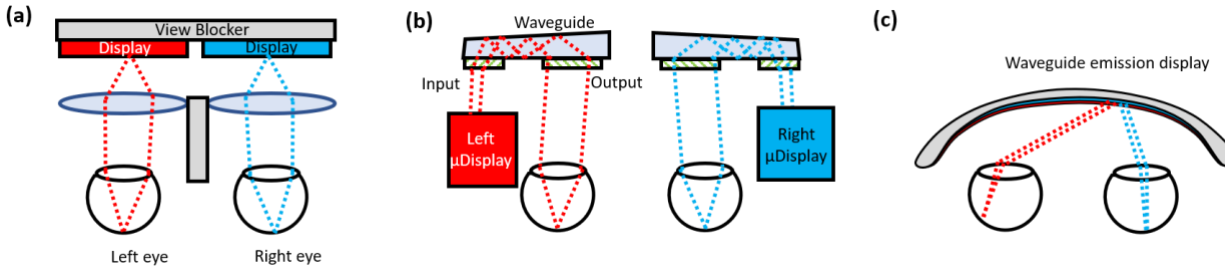

Figure 2.2: Schematic drawing of (a) a VR headset using refractive lenses to collimate light, (b) an AR headset using diffractive/holographic optical elements to input and output the images. (c) Concept of a compact 3-D display using waveguide emission display to directly project the images to the user's eyes.

Several beam-shaping approaches have been demonstrated in thin-film LEDs and they have their merits and limitations. Distributed Bragg reflectors (DBRs) can significantly enhance the cavity resonance to achieve directional emission and even lasing (Figure S2.1a).[16–20] The layered structure of DBRs is compatible with thin-film LED fabrication, but the emission direction is sensitive to the cavity length and its emission spectrum is highly angle dependent (Figure S2.2). Alternatively, thin-film LED pixels can be made into line or point sources with microlens arrays to collimate the emitted light (Figure S2.1b).[21] This approach has been used in white emitting

OLEDs to demonstrate a small beam divergence angle of 9°.[22,23] But due to its small pixel size, the maximum brightness per area is limited and therefore this approach is not practical.

Instead of beam-shaping the air mode, diffractive optical elements (DOEs) have been used to extract thin-film optical modes for directional emission. Because the optical cavity length of a thin-film LED is close to the wavelength of light, it only supports the low order transverse optical modes, which have a highly quantized mode dispersion. By incorporating a DOE into a thin-film LED, the optical modes can be extracted to a narrow range of angles through Bragg diffraction (Figure S2.1c). Zhang et al. patterned the OLED emitting layer with 2D square array of pillars, and the resulting corrugated Ag electrode diffracts the waveguide modes.[24] However, with this device the corrugated metal cathode extracts the transverse electric (TE) waveguide mode, the transverse magnetic (TM) waveguide mode, and the surface plasmon polariton (SPP) mode, resulting in a complex emission profile with the presence of the background air mode. An alternative approach is to laterally separate the LED pixel from the DOE pixel in the device stack, such that the air mode emitted from the LED pixel can be blocked,22 and subsequently emitted photons are coupled into a thin-film waveguide stripe and extracted by the DOE pixel, yielding directional emission (Figure S2.3).23 But due to the low coupling efficiency and high waveguide loss, the device efficiency is less than 1%.

Another important aspect of thin film LEDs that is often overlooked is how to achieve polarized emission. One approach is to mechanically align the emitting molecules, resulting in polarized emission from the device.[27,28] Alternatively, a fine metallic grating is used as an external polarizer to selectively transmit the TM light and reflect the TE light.[29] However, these approaches are not practical. Uniaxial alignment inevitably induces contamination to the emission layer and damages to the devices, and the metallic grating wastes the TE light and reduces the outcoupling

efficiency by half.[30] Therefore, it is desirable to have a light source intrinsically emitting polarized light.

In this chapter, we demonstrate full-area highly directional polarized light emission from organic LEDs on nanostructured substrates to selectively extract the TE waveguide mode while suppressing the SPP, TM waveguide, and air modes (Figure 2.2b). We first demonstrate such a device concept using an OLED with an Ir-complex emitter. By tuning the thickness of the OLED stack, the corrugation is mostly planarized at the cathode and the diffraction of TM waveguide mode and SPP mode is highly suppressed. To further suppress the emission from the air mode, the thickness of the electron transport layer (ETL) is tuned to its valley thickness in the air mode profile (Figure S2.4) so the emission from the OLED cavity is blocked by total internal reflection from glass to air. The resulting waveguide emitting LED shows only strong TE waveguide emitted light with a high TE to TM mode extinction ratio. We then apply a similar architecture to an OLED with an Eu-complex emitter having a narrow emission spectrum to demonstrate the highly directional beam shape with a divergence angle less than 3°.

2.2. Result and Discussion

2.2.1. Device Architecture

To achieve waveguide-only emission in a thin-film LED, the device architecture needs to extract the waveguide mode while suppressing emission from the air, TM waveguide, and SPP modes. The air mode emission of a thin-film LED is determined by the cavity effect. Because the reflectivity is 85% for the Al cathode but 2% for the ITO anode, the cavity effect is mostly determined by the distance between the emitting layer (EML) and the reflective electrode, which is the thickness of the ETL in most thin-film LEDs. Herein, we use a typical OLED having a structure of glass substrate/ITO/hole transport layer (HTL)/ EML/ETL/cathode to demonstrate the

waveguide emission architecture. A common Ir-complex tris[2-phenylpyridinato-C^2,N]iridium(III) ($Ir(ppy)_3$) is used as the emitter, which has an EL peak at 520 nm.

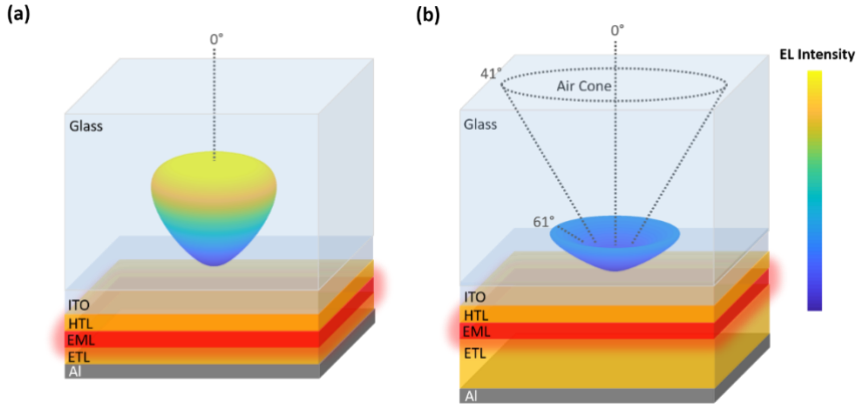

Figure 2.3: Simulated angular emission profile in the substrate at (a) 60 nm ETL (maximal air mode) and (b) 140 nm ETL (minimal air mode). The wavelength of the light is 520 nm, corresponding to the EL peak of $Ir(ppy)_3$.

To achieve pure TE waveguide emission, our first task is to suppress the emission from the air mode. Based on the optical mode distribution, the air mode intensity changes periodically with the ETL thickness (Figure S2.4). From the peak to the valley, the air mode contribution drops from 26% to 3% while the substrate mode increases from 21% to 42%. To understand the difference in the mode distribution, we simulate the angular emission profile inside the glass substrate at the air mode peak (60 nm ETL) and valley (140 nm ETL), respectively (Figure 2.3). With a 60-nm-thick ETL, the emission profile is acorn-shaped with a strong distribution in the normal direction, therefore light can easily escape from the substrate, resulting in the air mode being the strongest. With a 140-nm-thick ETL, the emission profile becomes bowl-shaped, and the peak angle shifts to 61°, above the critical angle of 41° from glass to air, which results in the total internal reflection of the light and a strong reduction of the air mode. When the ETL thickness increases above 140

nm, a higher order cavity mode appears, and the air mode intensity increases again (Figure S2.4). These simulation results indicate we can suppress the air mode emission from the thin film LED cavity by simply tuning the ETL thickness.

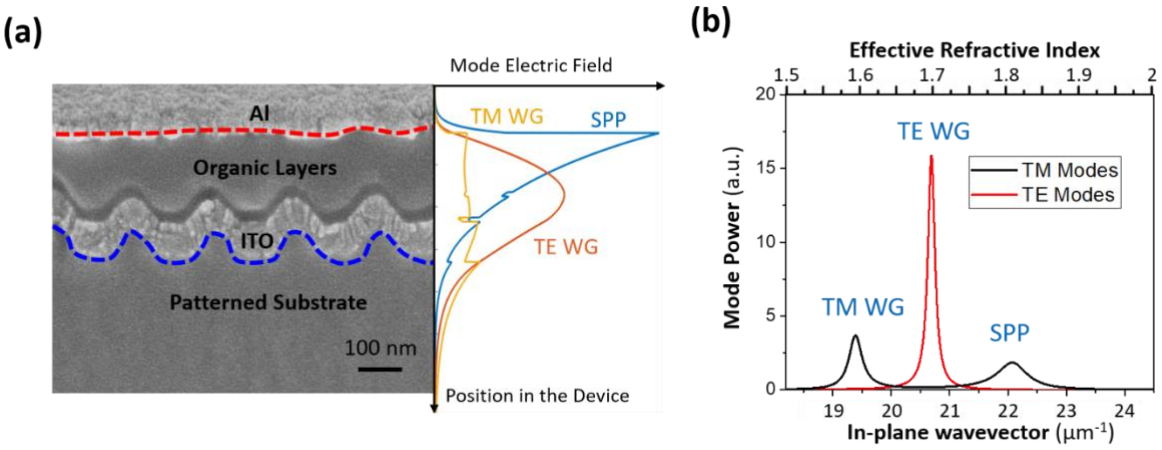

Figure 2.4: (a) Cross-section SEM of the waveguide emission OLED fabricated on a 1-D grating, and the corresponding electric field ($|E|^2$) distribution of the optical modes from FDTD simulation. (b) The mode dispersion of a reference OLED with 140 nm ETL.

Next, we use optical simulation to characterize the waveguide modes in an OLED. Because the refractive index of ITO is higher than that of the organic layers and the glass substrate, it forms a slab thin-film waveguide. We use the finite-difference time-domain (FDTD) method to simulate the electric field distribution of the optical modes in an OLED with a 140-nm ETL (Figure 2.4a). The results confirm that the TE waveguide mode is located at the vicinity of the ITO anode, therefore having a corrugated ITO anode will allow effective extraction of the TE waveguide mode by diffraction. The diffraction process is described by the Bragg equation $\vec{k} = \vec{k}_{WG} - \vec{G}$, where $\vec{k}$ and $\vec{k}_{WG}$ are the in-plane wavevectors of the diffracted and the original waveguide mode respectively, and $\vec{G}$ is the grating vector defined by the periodicity of the corrugation Λ, such

that $G = 2\pi / \Lambda$. When k is smaller than the vacuum wavevector $k_0 = 2\pi / \lambda$, the waveguide mode is extracted into air at the angle of $\theta = \sin^{-1}\left(k / k_0\right)$. Figure 2.4b shows the mode dispersion of the OLED device. Because the TE waveguide mode is confined in the low-loss ITO anode, it has a narrow dispersion peak, which translates to a small divergence angle from the waveguide emission OLED (Figure S2.5).

It is important to note that in addition to the TE waveguide mode, there are one TM waveguide mode and one SPP mode present in the simulated OLED. To achieve a strongly directional and polarized emission, we need to extract the TE waveguide mode while suppressing the emission from the air, TM waveguide, and SPP modes. To suppress the air mode, the thickness of the ETL should be 140 nm, which corresponds to the air mode valley in the optical mode profile plot. In a conventional OLED where the air mode is optimized, the ETL thickness should be about 60 nm, which corresponds to the air mode maximum. Typically, having such a thin ETL in a corrugated OLED will also result in a corrugation in the Al electrode, which will diffract the SPP as well as the TM waveguide mode as these modes have strong distribution at the metal interface. On the other hand, since we need to have a thick ETL to suppress the air mode, this thermally evaporated thick ETL will render the top cathode to be almost planarized (Figure 2.4a).[31] As a result, the diffraction of both the TM waveguide and SPP modes is strongly suppressed. The residual corrugation depth is not sufficient to extract the TM modes, as they have shorter propagation length due to the absorption from the metal. Further, the planarized cathode also ensures the cavity effect is preserved such that the background emission can be efficiently suppressed by increasing the ETL thickness.

2.2.2. Waveguide Emission OLED Based on Ir-complex Emitter

To validate our device design, we fabricate OLED devices to study the effects of both the substrate corrugation and the ETL thickness (60 nm vs 140 nm). The corrugated substrates are patterned by soft imprinting using a master mold which consists of 1-D gratings having a 350 nm period and 100 nm depth. The modest corrugation depth ensures good conductivity on the ITO anode, as well as serves to minimize its influence on the OLED cavity (Figure S2.6). We then sputtered ITO and evaporated the organic/metallic layers on the substrates to fabricate the OLED devices. Angle-resolved emission spectra measurements were used to characterize the air mode dispersion in both TE and TM polarizations.[32,33] For OLEDs on the 1-D grating substrates, the measurement plane is normal to the grating grooves. To show the effect of beam-shaping, the air mode is tuned to show the angular emission profile at 520 nm, corresponding to the peak wavelength of the green emitter $Ir(ppy)_3$.

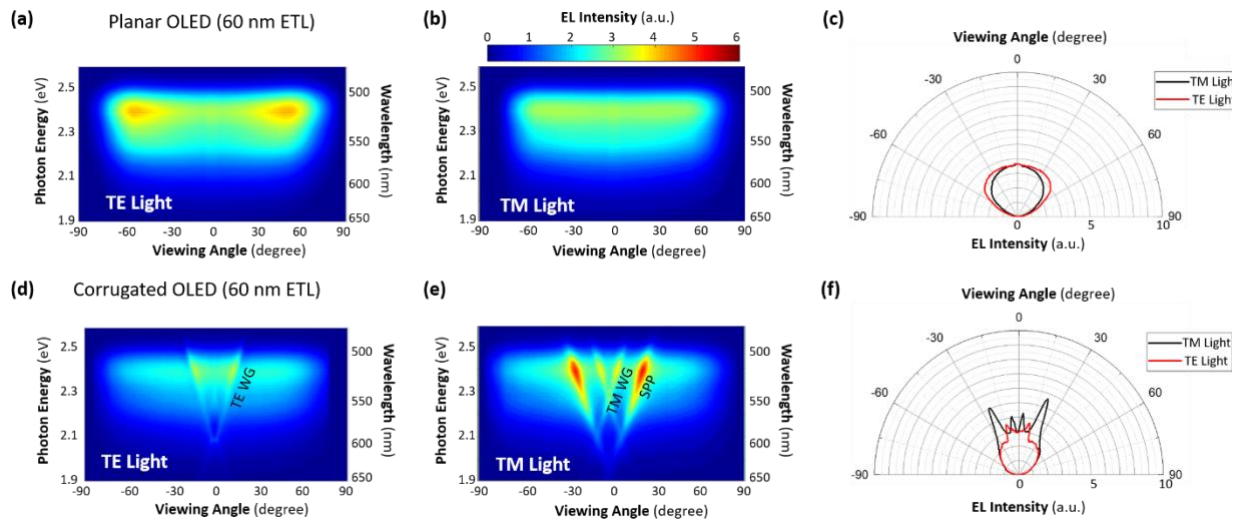

Figure 2.5: Measured mode dispersion in TE and TM polarizations for (a)(b) a planar OLED with 60 nm ETL and (d)(e) a corrugated OLED with 60 nm ETL. (c)(f) are the angular profiles at 520 nm for each OLED. From (d) we can see a faint feature corresponding to TE waveguide mode at 0°. This is because the corrugated substrate has larger surface area and has an overall higher film thickness than the simulated planar OLED.

For the planar OLED with a 60 nm-thick ETL, we observe the typical broad air mode background (Figure 2.5a-b). The emission profile shows a Lambertian-like pattern, with similar TE and TM emission profiles (Figure 2.5c). With a corrugated substrate, the OLED shows additional multiple diffraction features in addition to the featureless background from the air mode (Figure 2.5d-e). Based on the polarization and in-plane wavevector, the diffraction features are identified as the diffracted TE waveguide mode, TM waveguide mode and SPP mode.[34] The strong TM waveguide mode and SPP mode diffraction is caused by the corrugated Al with a depth of around 60 nm, which is confirmed in the cross-section SEM image (Figure S2.7). Due to the light scattering from the corrugated Al, the cavity effect is weakened, and the background emission is

reduced. Because several optical modes are diffracted into the air mode, the emission profile of the corrugated OLED has multiple peaks in both TE and TM polarizations (Figure 2.5f). The two TE polarized peaks come from the diffracted TE waveguide mode propagating at opposite directions. The TM polarized peaks can be attributed to the diffracted SPP modes at ±20° and the diffracted TM waveguide modes at ±4°. The magnitude of the SPP peaks is higher than the waveguide peaks, because the SPP mode percentage of a device with a 60 nm thick ETL is higher than the waveguide modes and is strongly diffracted at the highly corrugated Al cathode.

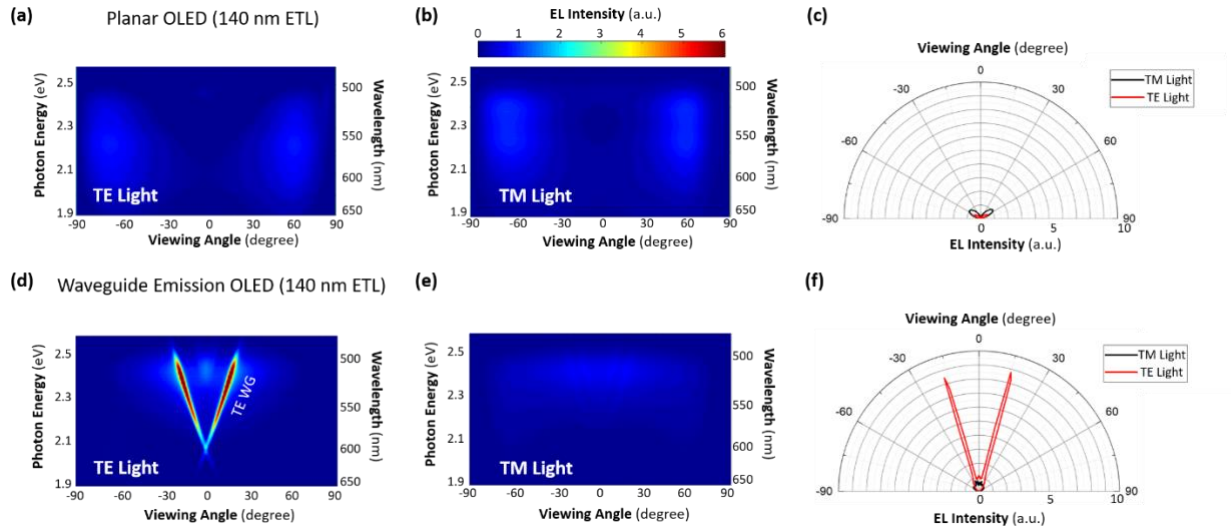

Figure 2.6: Measured mode dispersion in TE and TM polarizations for (a)(b) a planar OLED with 140 nm ETL and (d)(e) a waveguide emission OLED with 140 nm ETL. (c)(f) are the angular profiles at 520 nm for each OLED.

For the planar OLED with a 140 nm ETL, the measured mode dispersion is very different. Both the TE and TM polarized air modes almost completely vanished due to the suppression of the air mode emission (Figure 2.6a-c). With a corrugated substrate, the OLED still shows a negligible air mode background as expected, but with distinct TE waveguide mode diffraction features in the TE light profile. It is important to note that there are almost no TM waveguide mode

or SPP mode features in the TM light profile (Figure 2.6d-f). The vanishing of the TM waveguide and SPP features is resulted from the 140 nm thick ETL layer which efficiently planarized the Al cathode and suppressed the diffraction of the TM waveguide and SPP modes. From the emission profile, we can only see a highly directional emission peak corresponding to the TE waveguide emission, with a full-width at half-maximum (FWHM) divergence angle between 3.5° to 4.1°, depending on the wavelength (Figure S2.11). Due to the effective suppression of both the air mode background and diffraction of the TM polarized modes, the emission is highly polarized. We calculate the TE/TM extinction ratio for each wavelength at the corresponding waveguide emission peak (Figure 2.7c). A high extinction ratio of 13 is obtained between 520 nm and 540 nm, where the air mode emission is strongly suppressed using the cavity effect. Such highly polarized light is potentially useful for 3-D displays and displays which use a circular polarizer to reduce the reflection from ambient light.

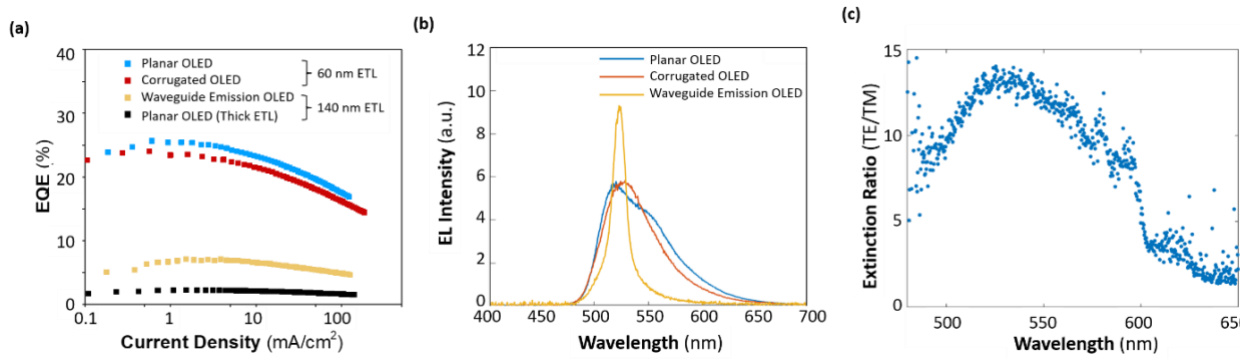

Figure 2.7**:** (a) EQE and (b) EL spectra comparison of the planar OLEDs, corrugated OLED and waveguide emission OLED. The EL spectra are measured at 18° viewing angle where the spectrum FWHM of the waveguide emission OLED is the smallest. (c) The extinction ratio of the waveguide emission OLED at each wavelength.

We compare the EQEs of the planar OLED and the waveguide emission OLED in Figure 2.7a. For the planar OLED having a 60 nm thick ETL, the outcoupling efficiency is maximized and the device has an EQE of 25%. When the ETL is increased to 140 nm, the outcoupling efficiency is minimized and the EQE is reduced to 2%. By incorporating corrugation in the device to extract the TE waveguide mode, the EQE of the waveguide emission OLED is increased to 7%, indicating the TE waveguide mode emission contributes an additional 5% of the EQE. This efficiency is much lower than the 21% TE waveguide mode distribution based on the optical simulation results, which estimates to a 24% TE waveguide mode extraction efficiency (Table S1). The inefficient extraction of the waveguide mode can be attributed to two factors. First, diffraction due to the grating is limited by the shallow corrugation depth of 100 nm and the small index contrast between the ITO and grating. Second, the propagation length of the TE waveguide mode is limited by the residual optical absorption from ITO, Al and grating, which limits the chance of diffraction. There are two approaches to improve the extraction efficiency of the TE waveguide mode. First, we can reduce the absorption with a more reflective Ag top electrode. Second, we can improve the corrugation geometry and the index contrast of the grating, which requires further optimization of the grating design and fabrication.

In addition to the directionality and polarization, the waveguide emission OLED also shows stronger EL peak intensity and smaller FWHM (Figure 2.7b). At 18° viewing angle, the EL peak of the waveguide emission OLED is 1.6 times higher than the reference OLED, while the FWHM is only 20 nm, much narrower than the planar OLED which has a 65 nm wide emission peak. In comparison, the corrugated OLED with a 60 nm ETL has a similar FWHM as the planar OLED because of the strong air mode emission. The smaller FWHM in a waveguide emission OLED stems from the narrow dispersion of the TE waveguide mode which is confined in the low-

loss 110-nm-thick ITO anode (Figure 2.4b). In Figure S2.8, we plot the normalized air mode dispersion of the Ir-complex waveguide emission OLED, which eliminated the influence of the emitter spectrum and reveals the line-shape of the TE waveguide mode.[35] The spectral width of the extracted TE waveguide mode is 18 nm, much narrower than the spectral width of $Ir(ppy)_3$, therefore the FWHM of the emitted light is significantly reduced. However, it also means a large portion of the emitter spectrum does not contribute to the waveguide emission at a given angle. As a result, the luminance of the waveguide emission OLED, which is a convolution of the EL spectra with the luminosity function, is actually lower than the planar OLED.

2.3. Conclusion

In summary, we designed a highly directional and polarized waveguide emission thin-film LED on a corrugated substrate such that the resulting gratings only extract the TE waveguide mode while suppressing light emission from other optical modes. To achieve these emission characteristics, the corrugation at the top cathode is planarized by thermal evaporation of a thick organic stack. This not only reduces the background air mode emission, but also suppresses the diffraction of SPP and TM waveguide modes, resulting in highly directional with a small divergence angle of 3° and polarized light emission from the TE waveguide mode having a TE/TM extinction ratio of 13. Because the device is simple to fabricate and can be easily scaled-up, our discovery of this strong directional and polarized light emission from OLEDs has important applications for displays, lighting and other photonic applications.

2.4. Methods

2.4.1. Fabrication of 1-D Gratings

The 1-D grating nanostructures on silicon substrate are patterned using a combination of interference lithography (IL)[36,37] and transferred using reactive ion etching (RIE). To begin with, a silicon substrate is spin-coated with 100 nm antireflection coating (ARC i-con-7, Brewer Science) and 180 nm positive photoresist (PFI-88A2, Sumitomo). The antireflection coating film is used to reduce the reflection from silicon substrate during interference lithography. The 1-D periodic grating nanostructures in photoresist are patterned using 325 nm wavelength HeCd laser exposure in a Lloyd's mirror IL setup. Two coherent laser beams are interfered to create periodic intensity pattern in Lloyd's mirror IL setup. Then, the periodic grating pattern is transferred to the underlying silicon substrate using O_2 and Cl_2 RIE. After etching, an RCA cleaning process is used to remove the organic contaminants on the substrate surface. The surfaces of the molds are then treated with silane to mitigate adhesion for the subsequent soft-imprinting process.

2.4.2. Fabrication of Waveguide Emission OLEDs

For the waveguide emission OLEDs, we first fabricate a corrugated substrate through soft-imprinting. A polydimethylsiloxane (PDMS) stamp is used to replicate the pattern from the master mold. The glass substrates are cleaned with standard ultrasonication procedure in acetone and isopropyl alcohol for 15 minutes each. Then a small amount of NOA-81 epoxy (from Norland Products Inc.) is dropcast on the glass substrate. The stamp is pressed on the epoxy to remove air gaps in between. Then the substrate with stamp is treated under 365 nm UV light (Jelight UVO cleaner Model 42) for 4 minutes to cure the epoxy. Afterwards the stamp is removed to leave behind the corrugated substrate.

For the Ir-complex based OLED, the device structure is ITO (110 nm) /MoO_x (10 nm) / 4,4′-Cyclohexylidenebis[N,N-bis(4-methylphenyl)benzenamine] (TAPC) (40 nm) / 4,4′-Bis(N-carbazolyl)-1,1′-biphenyl (CBP) (20 nm): 5% Tris[2-phenylpyridinato-C2,N]iridium(III) ($Ir(ppy)_3$) / 4,7-Diphenyl-1,10-phenanthroline (Bphen) (60 nm) / Bphen: 12% Cs_2CO_3 (80 nm)/ Cs_2CO_3 (2 nm)/ Al (100 nm). Because a thick ETL is used in the waveguide emission OLED, we dope Cs_2CO_3 in the Bphen layer to enhance electron transport and maintain good charge balance.[38] The reference Ir-based OLED has a similar structure, with only 60 nm Bphen as the ETL.

2.4.3. Characterization of OLEDs

The device voltage - current density curves are measured using a Keithley 2400 SourceMeter. The EQE is measured in an integration sphere (Labsphere Illumia). The edge of the substrates are covered to block the substrate mode leakage. The current efficiency is measured with a LS-100 luminance meter. For the angular EL spectra measurements, we setup a spectral goniometer using an automatic rotary stage (Griffin Motion, RTS-DD-100). Light from the operating device is collected and sent to the spectrometer (Ocean Optics HR4000) by an optical fiber (Thorlabs Ø200 μm, 0.22 NA) from 20 cm away. A wire grid polarizer (Thorlabs WP25L-VIS) is used to measure TE and TM light, respectively. For full-angle (-90° to 90°) measurements, the angle step is 1°. To determine the divergence angle FWHM, a finer angle step of 0.2° is used within a smaller angle range. A schematic drawing of the ARES setup is shown in Figure S2.10.

2.5. Supplementary Information

2.5.1. Beam Shaping in Thin-Film LEDs

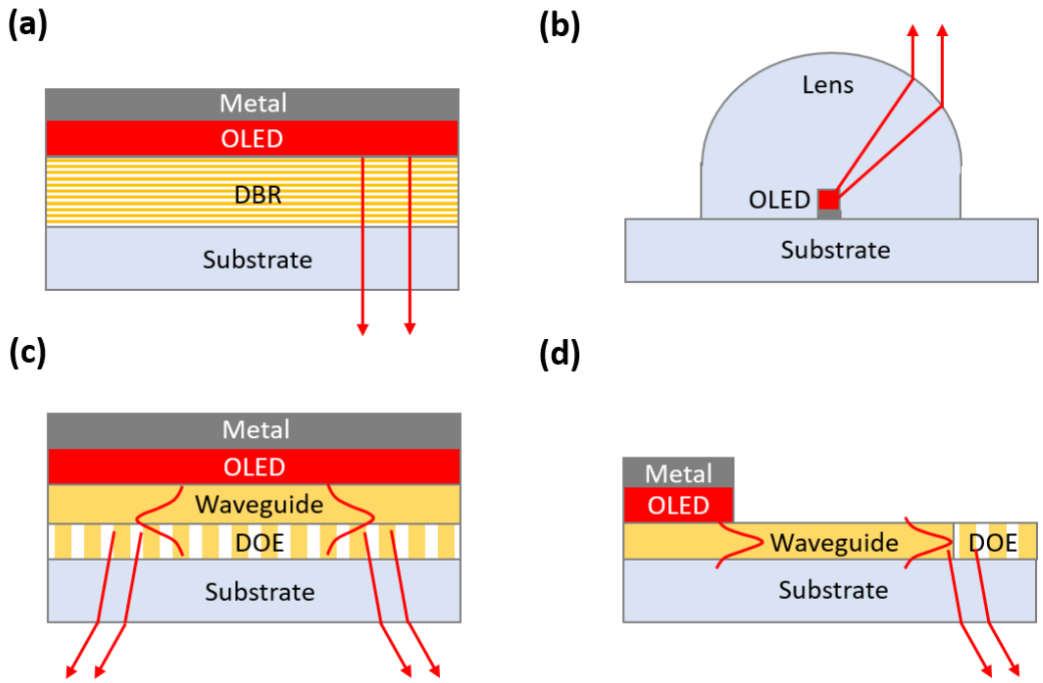

Figure S2.1: Different beam-shaping approaches for OLEDs. (a) Using a distributed Bragg reflector (DBR) to enhance the cavity resonance. (b) Using a point OLED source and a microlens to focus the light. (c) Vertically stacking the DOE and the waveguide with the OLED for more efficient waveguide coupling and extraction. (d) Coupling light from an OLED line source to a thin-film waveguide and using a diffractive optical element (DOE) to extract the waveguide mode.

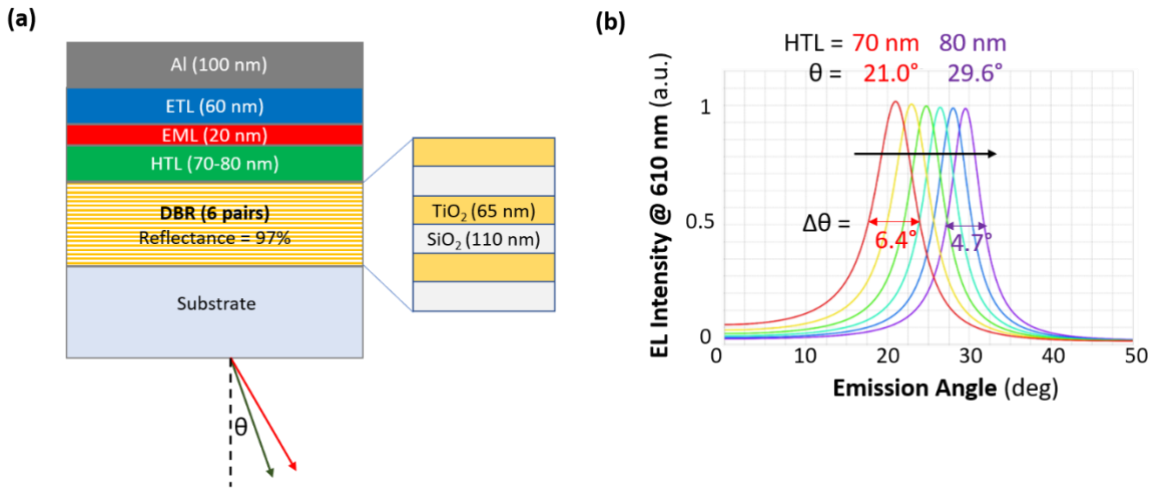

Figure S2.2: (a) An OLED device with a strong cavity using an embedded DBR structure. The DBR is designed to have 97% reflectance at $\lambda = 610$ nm to enhance the cavity effect. (b) Angular profile of a DBR OLED at $\lambda = 610$ nm. When the HTL thickness shifts from 70 nm to 80 nm, the emission peak shifts by 9°. The high sensitivity to the cavity length makes the design impractical. In addition, the FWHM divergence angles ($\Delta\theta$) are around 5.5°, too large to be considered as good directional light source.

2.5.2. Directional emission by extracting the substrate or waveguide modes (separate pixels)

In this approach, light from the OLED pixel is coupled into the substrate or a waveguide stripe, then a diffractive optical element (DOE) is used to extract the substrate or waveguide mode. In [Ref 22], Zhang et al. uses glass and polyethylene terephthalate (PET) substrates as the waveguide, a 2D square array of pillars as the DOE and demonstrated directional emission with <15° beam divergence. Because a thick substrate ($d >> \lambda$) supports a continuous range of waveguide modes propagating at angles above the critical angle, narrow beam divergence is achieved by reducing the size of the DOE and increasing its distance from the OLED pixel, so only a subset of the substrate modes can reach the DOE pixel (Figure S2.3a, b).

Instead of spatially screening the waveguide modes, a thin-film waveguide ($d < \lambda$) can be used so only a single waveguide mode is supported. In [Ref 23], Ramuz et al. couples light from an OLED evanescently into a 150 nm Ta_2O_5 Thin-Film waveguide with a coupling efficiency of 3.2% (Figure S2.3c, d). But due to the absorption loss from the metallic electrode and the ITO, only 20~30 μm of the OLED pixel can effectively couple light into the waveguide. This range can be increased by adding a spacer to separate the OLED emitting layer with the waveguide layer, but it also reduces the waveguide coupling.

Due to the filtering of the in-plane propagating directions (Figure S2.3b, d), this method yields a true parallel beam, compared to the full area grating structure (Figure S2.1c) which emits symmetrical arcs. However, it also has low efficiency because most of the substrate or waveguide modes are not accepted by the DOE.

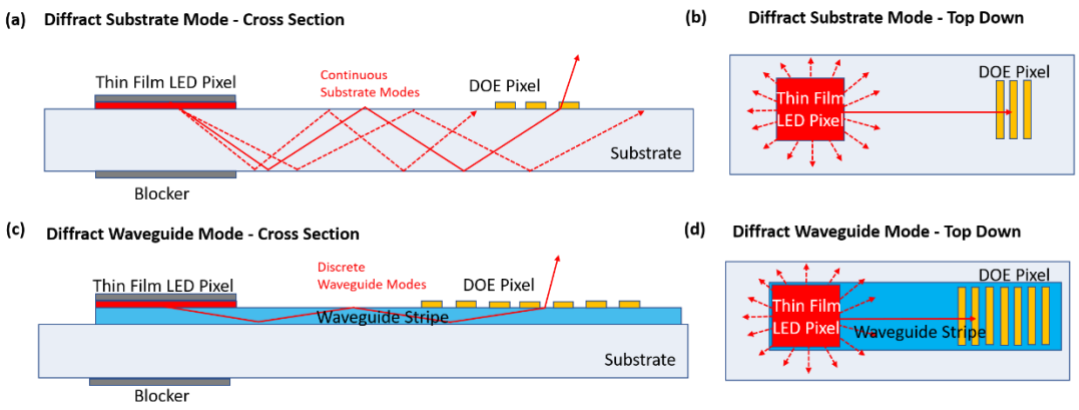

Figure S2.3: Achieving directional emission by (a)(b) diffracting the substrate mode and (c)(d) diffraction the waveguide mode. The dashed lines represent substrate or waveguide modes that cannot be diffracted by the DOE pixel.

2.5.3. Suppressing Air Mode and Extracting Waveguide Mode

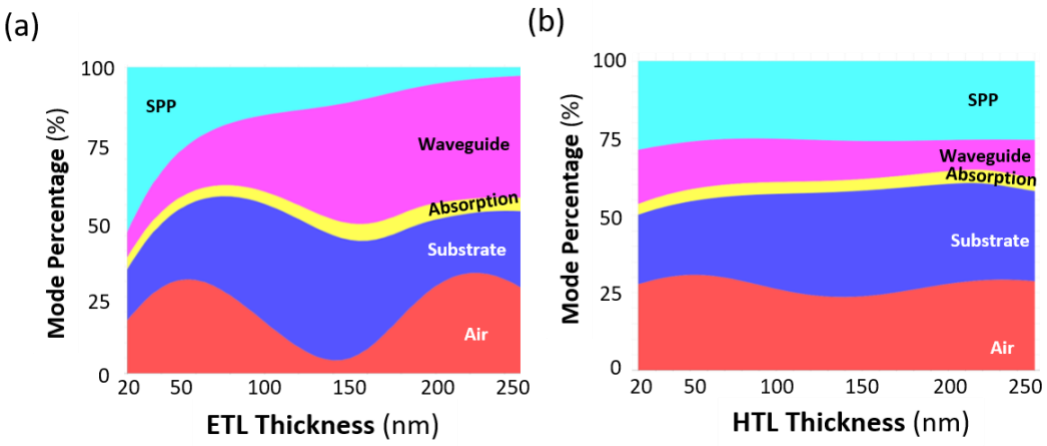

Figure S2.4: Simulated mode distribution of a bottom emitting OLED at 520 nm wavelength by changing the (a) ETL thickness (HTL = 60 nm) and (b) HTL thickness (ETL = 60 nm). A much greater fluctuation is observed in air mode intensity when we vary the ETL thickness, which indirectly confirms that the cavity effect is predominantly determined by the top Al cathode rather than the bottom ITO anode.

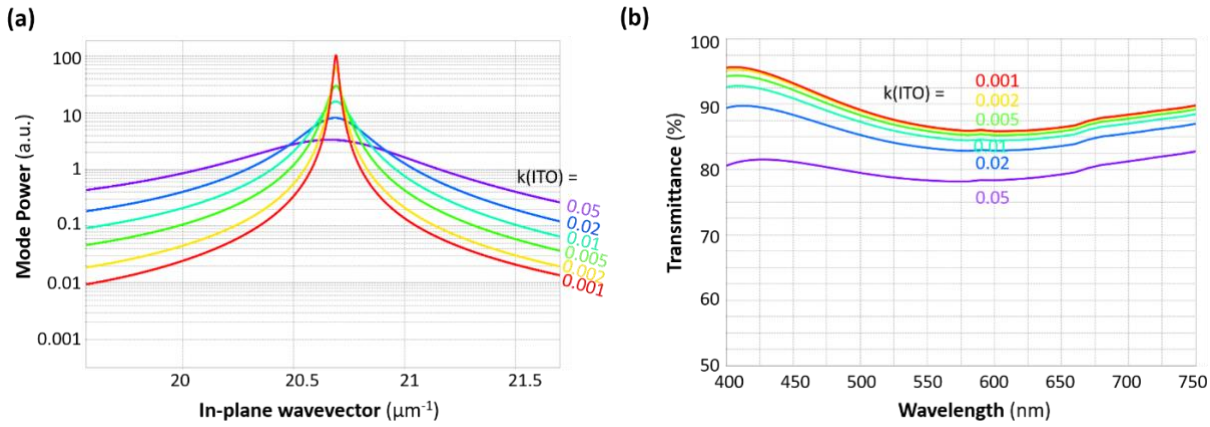

Figure S2.5: (a) The TE waveguide mode dispersion for a 100 nm ITO with different extinction coefficient *k*(ITO), simulated at λ = 520 nm. Using a 1-D grating with 300 nm period, the TE waveguide mode is diffracted to the normal direction. The FWHM divergence angle of the waveguide emission is 3.3° at *k*(ITO) = 0.05 and 0.2° at *k*(ITO) = 0.001. (b) The transmittance of the ITO on top of a glass substrate for each *k*(ITO). The measurement result of the sputtered ITO resembles the *k* = 0.01 curve, which is the value used in the simulation for this study.

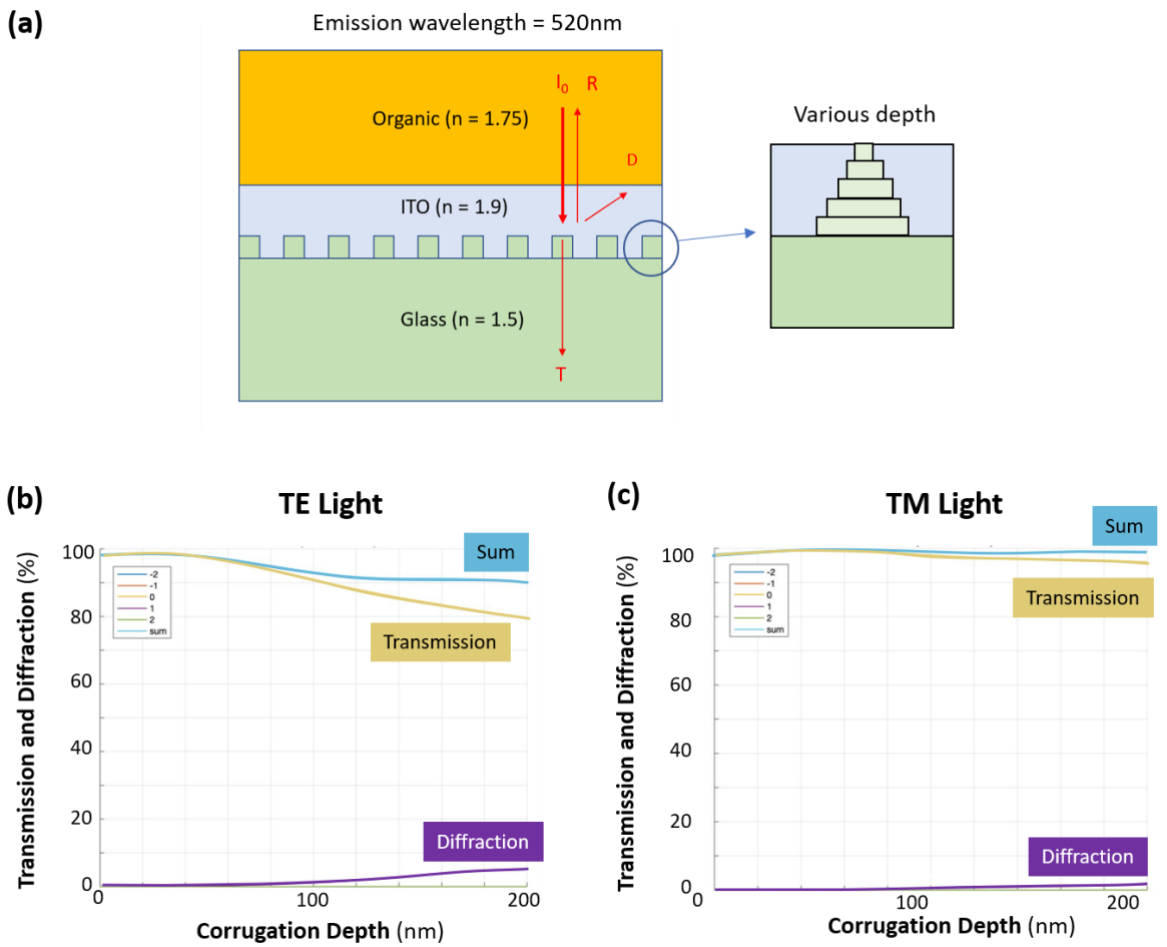

Figure S2.6: Rigorous-coupled wave analysis (RCWA) simulation of the transmittance and diffraction for light incident on a corrugated substrate in the normal direction. The corrugation depth is varied from 0 to 200 nm. At 0 nm, the transmittance is 98%; At 100 nm, the TE and TM light transmittance is 91% and 98%, respectively. This confirms that the 100 nm corrugation only has a small impact on the reflectance of the bottom ITO anode, and thus the cavity effect.

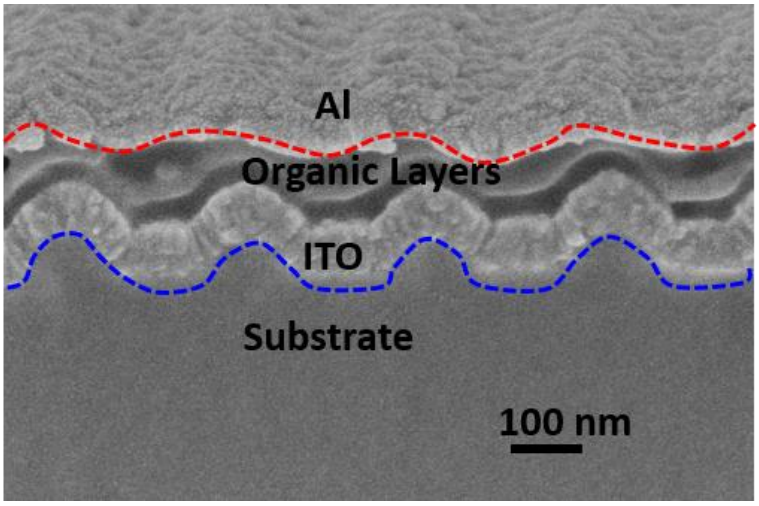

Figure S2.7: Cross-section SEM of a corrugated OLED with 60 nm ETL, showing the corrugation at the Al cathode

2.5.4. Waveguide Emission OLED

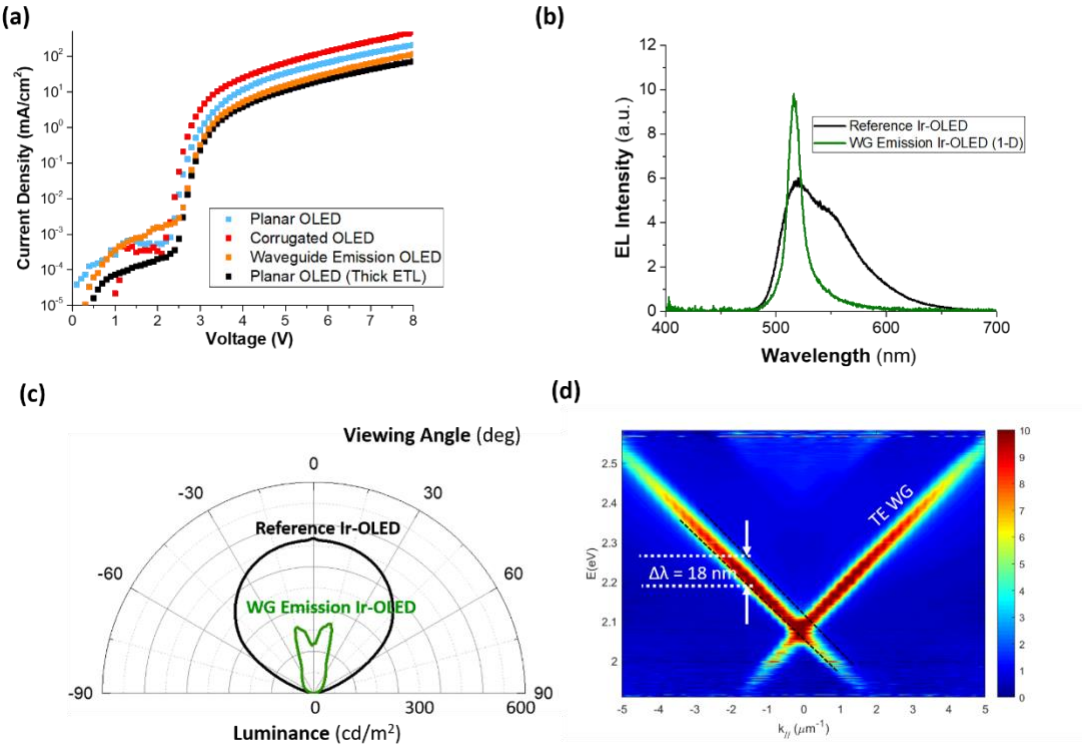

Figure S2.8: (a) Current density – voltage relation of the various Ir-OLED configurations. (b) The EL spectra measured at θ = 18°. (c) The angular luminance profile calculated from the air mode dispersion. Luminance is calibrated to the reference Ir-OLED. (d) Normalized mode dispersion of the Ir-complex waveguide emission OLED to show the spectral width of the diffracted TE waveguide modes. The in-plane wavevector is chosen between -5 μm^{-1} and 5 μm^{-1} to emphasize on the TE waveguide features.

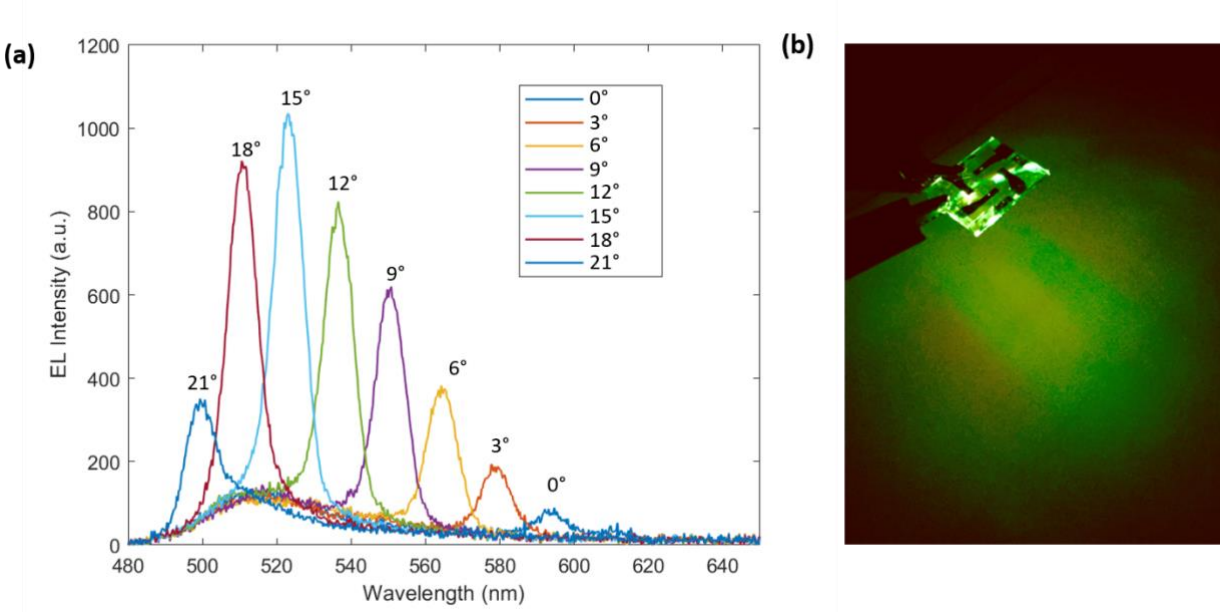

Figure S2.9: (a) Angular EL spectra of $Ir(ppy)_3$ based waveguide emission OLED. Due to the broad spectrum of $Ir(ppy)_3$, the waveguide emission peak shifts from 595 nm to 495 nm as the viewing angle shifts from 0° to 21°. (b) The spatial pattern of the emission from the OLED.

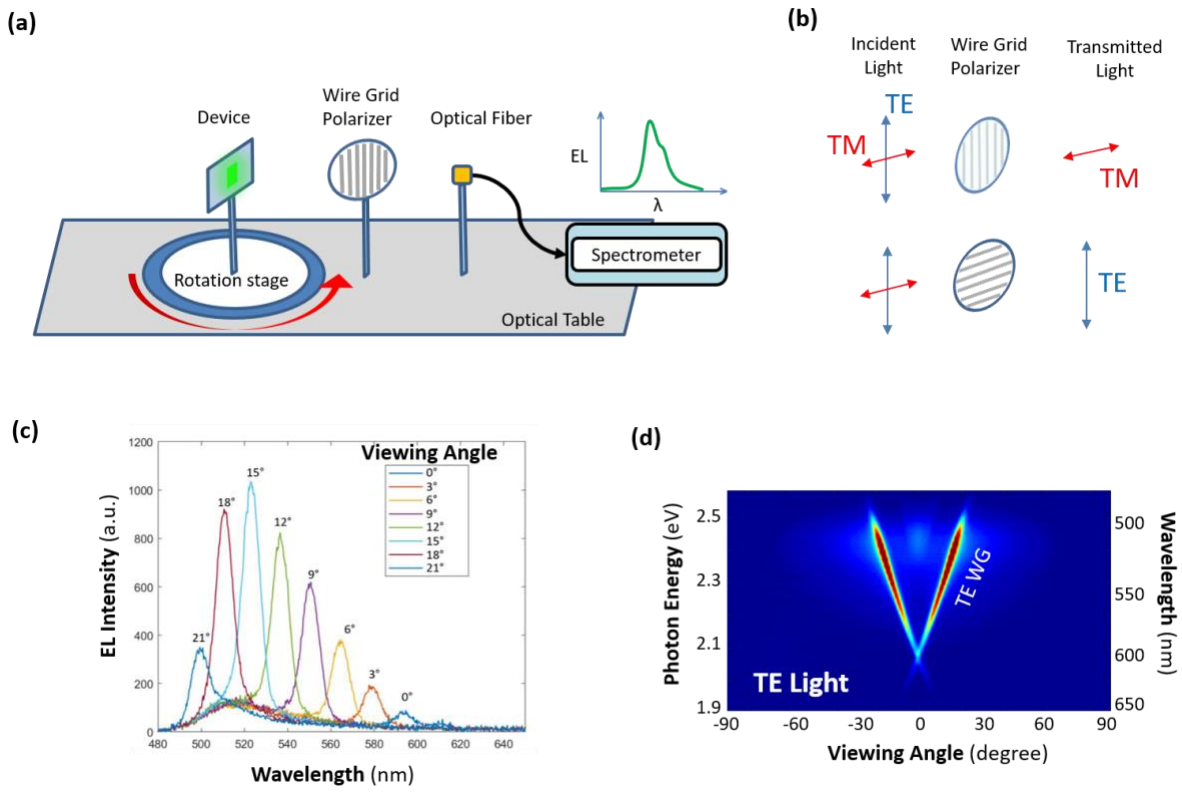

Figure S2.10: (a) Schematic drawing of the ARES setup. (b) Orientation of the wire grid polarizer and the transmitted mode. The arrows indicate the oscillating direction of the electric field. (c) Example of the measured ARES of a green waveguide emission OLED at selected angles with a polarizer to allow through only the TE light. (d) The air mode dispersion plotted corresponding to the ARES measurement.

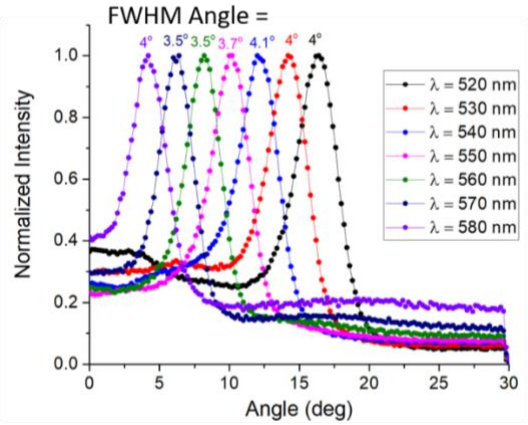

Figure S2.11: Determination of the wavelength dependent divergence angle FWHM of the (a) waveguide emission OLED with Ir-complex emitter.

2.5.5. Optical Simulation Method

The simulation of the optical modes and emission profile is conducted in Setfos 5.0. Setfos uses the oscillating dipole model to simulate the emitter radiative decay, and the transfer matrix method to simulate the optical modes and emission properties in a multilayer structure. The refractive indices used for the OLED and PeLED simulation are (λ = 520 nm): n(ITO) = 1.92+ 0.01·i, n(MoOx) = 1.99, n(PEDOT:PSS) = 1.5, n(TAPC) = 1.68, n_o(CBP) = 1.8, n_e(CBP) = 1.74, n(Bphen) = 1.73, n_o(TPBi) = 1.75, n_e(TPBi) = 1.72, n($(PEA)_2(FA)_3Pb_4Br_{13}$) = 2.3 + 0.04·i, n(Al) = 0.68+ 5.3·i. The refractive indices of the organic layers refer to *Adv. Funct. Mater*. **2019**, 1808803. The refractive indices of the ITO anode, MoOx, PEDOT:PSS and Al cathode are from the material database of Setfos 5.0.

The optical mode distribution plots shown in Figure S2.4 are simulated by inputting the thickness of each layer and varying the thickness of the ETL or HTL layer. Setfos considers the boundary of waveguide and SPP modes based on their in-plane wavevector and the corresponding effective refractive index. To further distinguish the contribution from TE and TM waveguide modes, we simulate the Dissipation Power Analysis which yields the power dissipation by the

effective refractive index at TE and TM polarizations. The waveguide and SPP modes are shown as distinct peaks that are localized around a particular effective refractive index. We then integrate the power under each peak to obtain the absolute power of each mode and divide by the total dissipated power to obtain the relative percentage (shown in Table S1).

The FDTD simulation was performed in Lumerical. The simulation was setup to run in 2-D to help minimize the computing resources required and simultaneously provided insights into the experimental results. The corrugation was designed using a script at the ITO glass interface and its refractive index was set to $n = 1.5$ to match with the epoxy used in the experiment. The depth of the corrugation was designed to be 95nm to avoid mismatch at the ITO/corrugation interface. For the Ir complex based OLED, a mode source at a fixed wavelength of 520nm was used to inject a plan wave in the device structure and the corresponding modes (TE and TM) were determined along with the propagation length.

Table S2.1: Optical mode distribution for planar OLEDs with 60 nm and 140 nm ETL thickness. The emitting zone is set to the center of the EML interface.

ETL Thickness	Optical Mode Percentage in OLED					
	Air	Substrate	TM Waveguide	TE Waveguide	SPP	Absorption
60 nm	26%	21%	7%	7%	34%	5%
140 nm	3%	42%	10%	21%	17%	7%

2.6. References

1. Chen, H., Lee, J., Lin, B., Chen, S. & Wu, S. Liquid crystal display and organic light-emitting diode display : present status and future perspectives. *Nature Publishing Group* **7**, 17113–17168 (2018).

2. Zheng, H. *et al.* All-solution processed polymer light-emitting diode displays. 1–7 (2013) doi:10.1038/ncomms2971.

3. Article, R. Emergence of colloidal quantum-dot light-emitting technologies. **7**, (2013).

4. Kim, Y. *et al.* Multicolored Organic / Inorganic Hybrid Perovskite Light-Emitting Diodes. 1248–1254 (2015) doi:10.1002/adma.201403751.

5. Lee, Jaewon, Neetu Chopra, and F. So. Cavity effects on light extraction in organic light emitting devices. **033303**, 1–4 (2008).

6. Fries, F., Fröbel, M., Ang, P. Y., Lenk, S. & Reineke, S. Real-time beam shaping without additional optical elements. *Light Sci Appl* (2018) doi:10.1038/s41377-018-0014-0.

7. Reineke, S., Leo, K. & Thomschke, M. White organic light-emitting diodes : Status and perspective. **85**, (2013).

8. Fattal, D. *et al.* A multi-directional backlight for a wide-angle, glasses-free three-dimensional display. *Nature* **495**, 348–351 (2013).

9. Lin, W. *et al.* An updatable holographic three-dimensional. **451**, 694–698 (2008).

10. Elgala, H. Indoor Optical Wireless Communication : Potential and State-of-the-Art. 56–62 (2011).

11. Haigh, P. A. & Ghassemlooy, Z. Visible Light Communications Using Organic Light Emitting Diodes. 148–154 (2013).

12. Sandanayaka, A. S. D. *et al.* Indication of current-injection lasing from an organic semiconductor. *Applied Physics Express* **12**, 61010 (2019).

13. Cipresso, P., Alice, I., Giglioli, C., Raya, M. A. & Riva, G. The Past , Present , and Future of Virtual and Augmented Reality Research : A Network and Cluster Analysis of the Literature. **9**, 1–20 (2018).

14. Maimone, A., Labs, F. R., Wang, J. & Labs, F. R. Holographic Optics for Thin and Lightweight Virtual Reality. **39**, (2020).

15. Prospects and challenges in augmented reality displays. *Virtual Real. Intell. Hardw.* **1**, pp.10-20. (2019).

16. Wang, M., Lin, J., Hsiao, Y., Liu, X. & Hu, B. Investigating underlying mechanism in spectral narrowing phenomenon induced by microcavity in OLEDs. *Nat Commun* 1–7 doi:10.1038/s41467-019-09585-0.

17. Murawski, C. *et al.* Narrowband Organic Light-Emitting Diodes for Fluorescence Microscopy and Calcium Imaging. **1903599**, 1–8 (2019).

18. You, A., Be, M. A. Y. & In, I. Dynamics of a high- laser vertical-cavity organic. **181108**, 1–4 (2006).

19. Genco, A. *et al.* High quality factor microcavity OLED employing metal-free electrically active Bragg mirrors. **62**, 174–180 (2018).

20. Phys, A. Optically pumped lasing of an electrically active hybrid OLED-microcavity. **113301**, (2018).

21. Bai, G. *et al.* Theoretical analysis and design for highly collimated planar light source based on organic light-emitting diodes using Fresnel lens.

22. Aratani, S. *et al.* Collimated Light Source Using Patterned Organic Light-Emitting Diodes and Microlens. (2010) doi:10.1143/JJAP.49.042101.

23. Zhou, L. *et al.* using customized lenticular microlens arrays structure Light beam shaping for collimated emission from white organic light- emitting diodes using customized lenticular microlens arrays structure. **201902**, 1–6 (2018).

24. Phys, A. Enhancing the emission directionality of organic light-emitting diodes by using photonic microstructures. **213302**, 10–14 (2013).

25. Zhang, S., Turnbull, G. A. & Samuel, I. D. W. Highly Directional Emission and Beam Steering from Organic Light-Emitting Diodes with a Substrate Diffractive Optical Element. 343–347 (2014) doi:10.1002/adom.201300441.

26. Ramuz, M. *et al.* Coupling light from an organic light emitting diode (OLED) into a single-mode waveguide : Toward monolithically integrated optical sensors Coupling light from an organic light emitting diode „ OLED … into a single-mode waveguide : Toward monolithically. **084508**, (2013).

27. Masahiro Misaki, Yasukiyo Ueda, Shuichi Nagamatsu, Masayuki Chikamatsu, Yuji Yoshida, Nobutaka Tanigaki, and K. Y. Highly polarized polymer light-emitting dioctylfluorene) thin films. *Appl Phys Lett* **243503**, 1–4 (2005).

28. Choi, G. J., Le, Q. Van, Choi, K. S., Kwon, K. C. & Jang, H. W. Polarized Light-Emitting Diodes Based on Patterned MoS 2 Nanosheet Hole Transport Layer. **1702598**, 1–8 (2017).

29. Zschiedrich, L., Greiner, H. J., Burger, S. & Schmidt, F. Numerical analysis of nanostructures for enhanced light extraction from OLEDs. *Proceedings of SPIE* **8641**, 86410B (2013).

30. Zhou, L. *et al.* Tailored Polarization Conversion and Light-Energy Recycling for Highly Linearly Polarized White Organic Light-Emitting Diodes. **1900341**, 1–9 (2020).

31. Will, P. *et al.* Efficiency of Light Outcoupling Structures in Organic Light-Emitting Diodes : 2D TiO2 Array as a Model System. **1901748**, (2019).

32. Wierer, J. J., David, A. & Megens, M. M. III-nitride photonic-crystal light-emitting diodes with high extraction efficiency. *Nat Photonics* **3**, 163–169 (2009).

33. Schwab, T. *et al.* Coherent mode coupling in highly efficient top-emitting OLEDs on periodically corrugated substrates. *Opt Express* **22**, 7524 (2014).

34. Schwab, T. *et al.* Coherent mode coupling in highly efficient top-emitting OLEDs on periodically corrugated substrates. *Opt Express* **22**, 7524 (2014).

35. Xiangyu Fu, Cheng Peng, Monica Samal, Nilesh Barange, Yi-An Chen, Dong-Hun Shin, Yash Mehta, Adam Rozelle, Chih-Hao Chang, and F. S. Mode Dispersion in Photonic Crystal Organic Light Emitting Diodes. *ACS Appl. Electron. Mater.* (2020).

36. Smith, H. I. Low cost nanolithography with nanoaccuracy. *Physica E Low Dimens Syst Nanostruct* **11**, 104–109 (2001).

37. Bagal, A. & Chang, C.-H. Fabrication of subwavelength periodic nanostructures using liquid immersion Lloyd's mirror interference lithography. *Opt Lett* **38**, 2531–2534 (2013).

38. Chen, Y. *et al.* n-Doping-induced efficient electron-injection for high efficiency inverted organic light-emitting diodes based on thermally activated delayed fluorescence emitter. 8400–8407 (2017) doi:10.1039/c7tc02406a.

CHAPTER 3: Hybrid laser cavity design for improved photon lifetime and performance

This chapter is an excerpt from a manuscript currently under review at IEEE Photonics Technology Letters

We report an optical cavity design that combines a distributed feedback (DFB) cavity as the primary feedback element for lasing with a silver mirror acting as a Fabry-Pérot cavity for broadband reflection and mode confinement. To evaluate the design, we studied the effects of the silver mirror by excluding the DFB cavity and compared its amplified spontaneous emission (ASE) properties with the sample without the mirror. In the structure with the mirror, the gain medium undergoes ASE at an excitation fluence of 17.5 μJ cm^{-2} compared to 37 μJ cm^{-2} for the sample without the mirror. This lower ASE threshold is attributed to enhanced mode confinement and photon density of states (PDOS) from the silver mirror increasing the cavity photon lifetime (τ_c). Using this hybrid cavity, a multimode optically pumped laser with a threshold of 42 μJ cm^{-2} is demonstrated. This hybrid cavity design offers an effective solution that can be readily applied to other thin film-based laser devices.

3.1. Introduction

Hybrid organic-inorganic halide perovskites have emerged as a potential candidate for laser applications due to their facile solution processing,[1] narrow emission linewidth and tunability spanning the visible spectrum.[2] Specifically, due to their cascading energy bands, quasi-2D Ruddlesden-Popper perovskites ($A'_2A_{n-1}B_nX_{3n+1}$) are a suitable class of materials for laser applications. These quantum wells are defined by the inorganic $[PbX_6]^{4-}$ octahedral cage surrounded by a dielectric barrier formed by the bulky A′ site organic cations while the A cations

occupy the space between corner-sharing octahedra. The bandgap is determined by the number of adjoining octahedral layers *n*.[3] The appeal of quasi-2D perovskites is that the exciton generated in the large bandgap domains can funnel through the energy staircase to the lower bandgap domain ($n \approx \infty$) where they accumulate with longer excited-state lifetimes, resulting in high radiative recombination efficiency required for lasing.[4]

For a dipole, the transition rate from one energy eigenstate to another depends on its environment according to Fermi's Golden rule. In an optical cavity, the Purcell factor (F_p) quantifies the modified decay rate of a dipole placed inside the cavity through the relation $F_p \propto Q/V$, where Q is the quality factor and V is the mode volume. A high Purcell factor leads to a faster decay, and consequently to a narrower emission linewidth.[5] Thus, by adjusting the Purcell factor it is possible to manipulate the radiation lifetime, which is crucial for attaining population inversion and lasing.

A high Purcell factor requires a cavity with a large quality factor and a high mode confinement (small V). One way to increase mode confinement is to use metallic mirrors as they offer enhanced mode confinement (Γ) by suppressing mode penetration in comparison to cavities formed by dielectric mirrors. This leads to a reduced mode volume (V) and consequently, a higher Purcell factor.[6,7] However, using metallic mirrors within a cavity also has some drawbacks. First, it can result in lossy coupling between the optical modes and the Surface Plasmon Polariton (SPP) mode at the metal interface. Second, the presence of a metallic mirror causes a notable Joule loss due to radiation absorption and consequently gives rise to non-radiative decay.[8]

To circumvent these issues, we propose a 'hybrid' cavity design that combines a DFB cavity with a Fabry-Pérot cavity formed by a planar metallic mirror as pictured in Figure 3.1a. The DFB cavity provides the primary feedback for oscillations while the vertical Fabry-Pérot cavity

confines the optical mode volume. To avoid emission quenching, the gain media is separated from the silver mirror with an interlayer dielectric which also acts as a buffer layer for nanoimprinting the DFB grating. Subsequently, we show that the ASE threshold of this hybrid cavity is reduced by a factor of 2 compared to perovskite-on-glass, indicating a high level of gain efficiency. It should be noted our hybrid cavity design applies to other gain materials. Finally, we demonstrate a multi-mode laser based on this hybrid structure showcasing the characteristics of both DFB and Fabry-Pérot cavity that exhibit long photon lifetime and therefore low operational threshold.

3.2. Experimental Results and Discussion

Lasing in a gain medium is generally supported by trapped waveguided modes in the film. For a non-leaky waveguide mode to be supported, the film must have a minimum thickness of $\lambda/2n_{eff}$, where n_{eff} is the effective refractive index of a mode propagating through the material with a wavevector $\vec{k} = 2\pi/\lambda$. The presence of these trapped modes facilitates population inversion, a prerequisite for stimulated emission.[9] To understand how the trapped mode affects lasing, we study the effect of confinement on the modal gain G_m. Modal gain is related to the intrinsic material gain G_a by the relation $G_m = \Gamma G_a$ where Γ is the confinement factor.[10] With an increase in the mode confinement, the overall modal gain can exceed the material gain resulting in improved light amplification. To ensure the maximum mode confinement factor for a planar perovskite film, we optimized the spin-coating process to yield a smooth 80 ± 10 nm thick film. A film thickness greater than that results in rough surface morphology[11] and supports higher-order leaky waveguided modes reducing the mode utilization efficiency (Figure S3.1).[12] However, due to low reflectivity at the surrounding interfaces such a film is unable to confine waveguided modes causing mode leakage. Therefore, to enhance the mode confinement we introduce a thin silver film

between the glass substrate and the perovskite layer for which the waveguide mode contribution increases to almost 70% as shown in Figure 3.1a.[13]

However, the inclusion of the silver reflector directly below the perovskite layer introduces losses due to the presence of the surface plasmons.[14] As the SPP mode propagates along the metal-dielectric interface it either gets scattered or is absorbed by the metal and dissipated as heat. These losses are determined by the distance separating the emitter and the silver film. SPP mode is dominant for an 80 ± 10 nm thick perovskite film in direct contact with the silver. To mitigate this loss channel, a dielectric interlayer is introduced between the perovskite and the silver reflector to physically separate them thereby reducing the coupling to the metal's surface plasmon. For an interlayer thickness greater than 20 nm, the SPP mode contribution drops rapidly, meanwhile the waveguide mode increases and remains almost constant irrespective of interlayer thickness (Figure 3.1a).[15] Additionally, the interlayer serves as a buffer layer onto which a one-dimensional DFB grating is nanoimprinted (SI).

Apart from the film thickness, the index contrast must be high at the interfaces surrounding the gain medium to prevent mode leakage. From Figure 3.1b, the perovskite-air interface has a reflectance value of 0.37 at 530 nm and is unmodified to facilitate a pathway for optical excitation of the gain medium. For the perovskite-glass interface, the reflectance is only about 0.27 which causes severe mode leakage, but with the introduction of a silver layer the reflectance is significantly improved. The oscillations in the reflectance spectrum is due to the cavity effect resulting from different phase conditions. However, the strength of the cavity effect diminishes as the silver film thickness is increased.

Figure 3.1: (a) Hybrid device structure with DFB and Fabry-Pérot elements; SPP and waveguide mode as a function of the interlayer thickness. The SPP mode contribution drops exponentially at an interlayer thickness of 50 nm meanwhile the waveguide mode contribution remains almost constant (b) top panel-reflectance at the perovskite-air interface, bottom panel-reflectance at the interlayer-Ag interface for different thicknesses of the silver mirror. (c) TE0 field distribution in the presence of the Ag layer causes improved mode confinement in the perovskite gain medium compared to the device without the Ag layer. (d) Comparing the transmittance function for the case of with and without Ag.

(a)

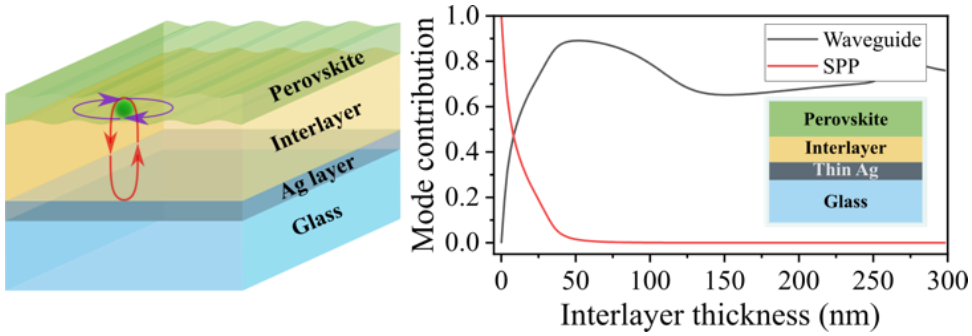
Perovskite
Interlayer
Ag layer
Glass
Mode contribution
Waveguide
SPP
Perovskite
Interlayer
Thin Ag
Glass
Interlayer thickness (nm)

(b)

(c)

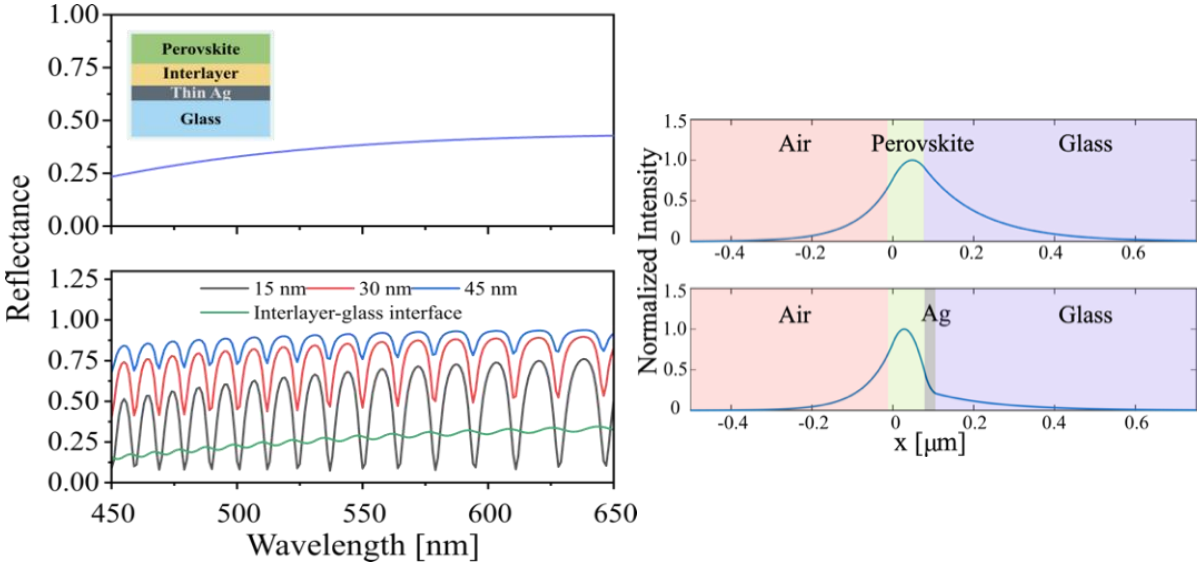
Perovskite
Interlayer
Thin Ag
Glass
Reflectance
15 nm
30 nm
45 nm
Interlayer-glass interface
Wavelength [nm]
Normalized Intensity
Air
Perovskite
Glass
Air
Ag
Glass
x [μm]

(d)

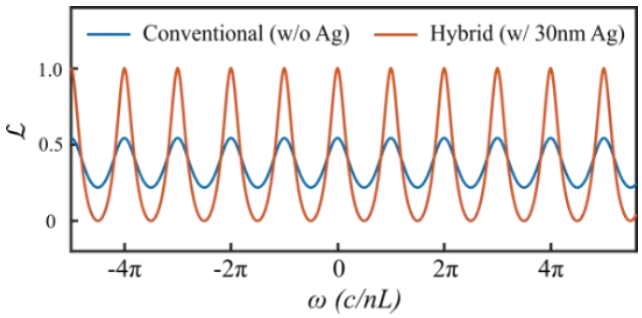
Conventional (w/o Ag)
Hybrid (w/ 30nm Ag)
ℒ
ω (c/nL)

Unlike nanostructured patterns, planar metallic mirror does not modify the magnitude of the wavevector, however, it also does not distinguish between the wavevectors of the modes that provide constructive feedback and the ones that do not. This is undesirable because a frequency-selective cavity can effectively filter out unwanted regions of the emission spectrum that do not contribute to light amplification and can be detrimental to the spatial coherence of the resulting laser emission.[16] Hence, to achieve an optimal balance between high reflectance and a strong cavity effect a 30 nm thick silver film is used. For this thickness, the interface reflectance increases to 0.84 leading to strong mode confinement (Figure 3.1c) and hence a larger PDOS which eventually enhances the Purcell factor.[17]

Stimulated emission is dependent on PDOS,[18] and hence an augmented PDOS facilitates population inversion. Therefore, to indirectly probe this effect we analyzed the modified local photon density of states (LPDOS) due to the silver reflector with respect to the free space PDOS according to the expression,

$$\rho_{cav}(\omega_k, k) = \rho_{free}\mathcal{L}(\omega_k) \tag{1}$$

where $\mathcal{L}(\omega_k)$ is the cavity transmission, and is given by,[10]

$$\mathcal{L}(\omega_k) = \frac{1}{1 + \frac{4\mathcal{F}^2}{\pi^2}\sin^2\left(\frac{\omega_k n L}{c}\right)} \tag{2}$$

where L is the cavity length, $\mathcal{F} = \pi(R_1R_2)^{0.25}/(1-\sqrt{R_1R_2})$ is the cavity finesse, R_1 and R_2 are the reflectance at the perovskite-air and the interlayer-metal interface respectively. A plot of the normalized transmission peak for the device with silver mirror is compared to the conventional case in Figure 3.1d, taking into consideration the numeric values of the film thickness and reflectance as defined above. By incorporating a silver mirror, the interference pattern is pronounced while maintaining the spectral characteristics which indicates an enhanced optical

filtering capability. Because of increased cavity transmission, the LPDOS is enhanced, which can be experimentally verified from the photoluminescence (PL) emission as a function of the silver layer thickness in Figure S3.2 along with the superimposed Fabry-Pérot oscillation.

(a)

b)

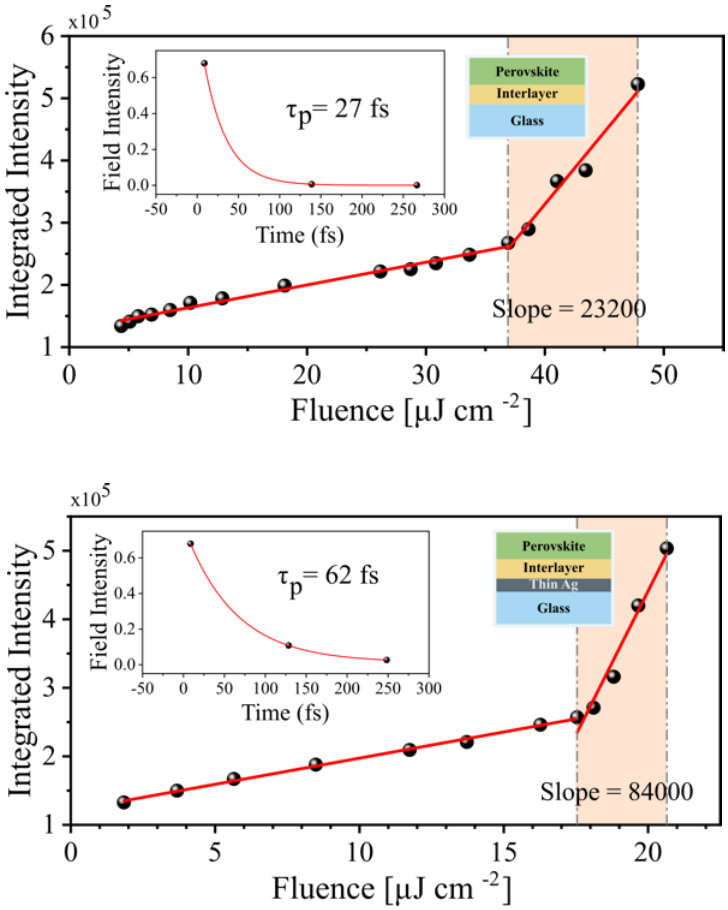

Figure 3.2: Intensity vs fluence curve highlighting the ASE regime (shaded) for (a) without Ag: threshold fluence of 36.9 $\mu J/cm^2$ and (b) with Ag: threshold of 17.5 $\mu J/cm^2$. The slope of the ASE regime is relatively higher for the device with Ag indicating enhanced light amplification. Inset: FDTD simulation results for τ_c.[19]

The modified gain properties of the film can be obtained from the amplified spontaneous emission (ASE) measurements as it propagates through an inverted medium without any feedback.

In Figure 3.2(a-b), the output light intensity vs. excitation fluence curve for a perovskite film on a glass substrate (conventional structure) is compared to the one with a silver reflector. In both configurations at low external pumping power, the integrated intensity of the spontaneous emission peak at 525 nm exhibits a linear progression until it reaches a certain threshold fluence beyond which, the curve demonstrates a noticeably steeper slope due to the ASE peak at 533 nm. The slope of this region, called slope efficiency, is used to assess the photon lifetimes and the effectiveness of the amplification process.[20] The slope efficiency of the device with a silver layer is 3.6 times higher with a lower threshold fluence of 17.5 $\mu J\ cm^{-2}$ than that of the device without a silver reflector having a threshold of 36.9 $\mu J\ cm^{-2}$. This suggests an enhanced photon lifetime and is consistent with the enhanced LPDOS.[21] A high slope efficiency with a low operational threshold implies that an overall higher laser throughput can be achieved for the same gain medium and external pumping scheme.

To confirm the enhancement in the cavity photon lifetime, a Finite Difference Time Domain (FDTD) simulation was performed where a time monitor records the photon wave packet's intensity as a function of time while undergoing back-and-forth reflections at the interfaces surrounding the gain medium. From the inset in Figure 3.2(a-b), the light intensity takes 27 fs and 62 fs to decay in the structure without and with the silver layer respectively. The observed 2.3-times enhancement in photon lifetime provides further evidence that photons have a prolonged existence within the structure with the silver mirror compared to the conventional structure which subsequently assists with light amplification.

(a)

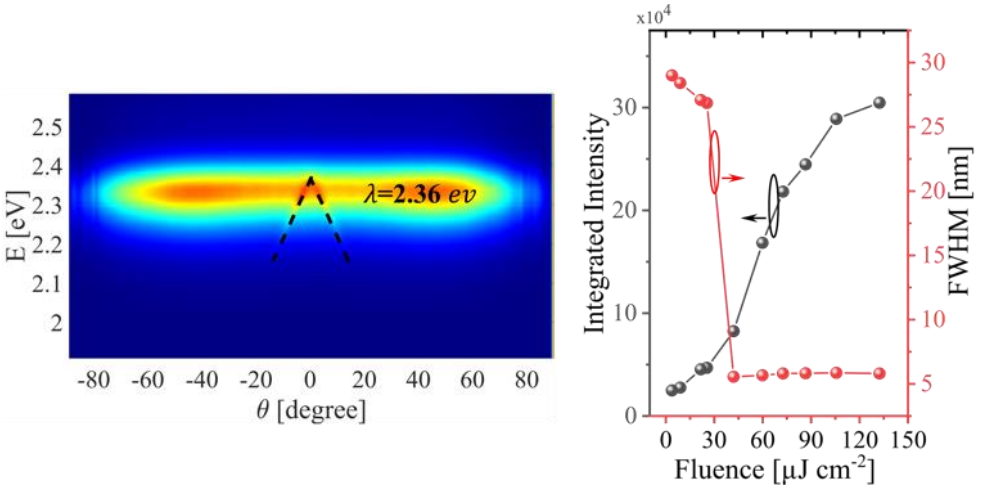

(b)

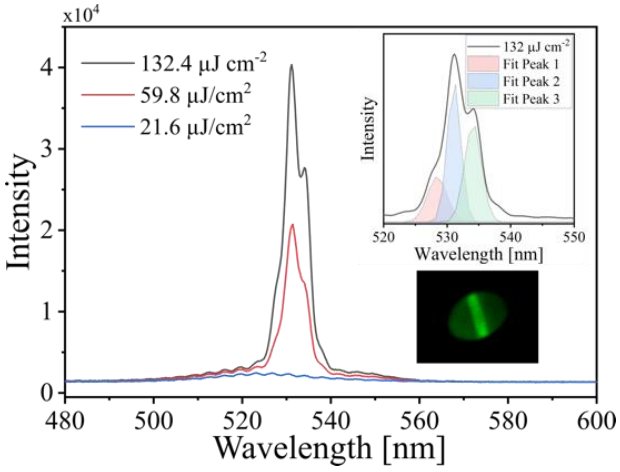

Figure 3.3: (a) ARPL for $\Lambda = 295\,nm$ grating. The input-output laser light curve shows typical signautre of lasing behavior; along with the sudden drop in the FWHM as a function of the excitation fluence. (b) Multimode lasing behavior with the inset showing the composite linewidth, and a photograph of a central bright fringe typical of lasing behavior.

Finally, we fabricated a hybrid lasing structure incorporating DFB cavity with the silver reflector (SI). To determine the optimum grating pitch for the 2nd order DFB cavity we performed angle-resolved photoluminescence (ARPL) measurements to ensure resonance along the normal direction.[22] According to the Bragg's law $\vec{k}' = \vec{k} \pm m\vec{k}_G$, where $\vec{k}_G = 2\pi/\Lambda$ is the grating

wavevector implying that the cavity resonance can be tuned through Λ. From the ARPL results in Figure 3.3a, we found that a grating pitch of $\Lambda = 295 \pm 5$ nm results in a strong intensity modulation in the normal direction.

Equally spaced oscillatory modes superimposed on the PL spectra were observed (Figure 3.3b) for a fluence of 21.6 μJ cm^{-2} which is characteristic of the Fabry-Pérot etalon.[23] From the Free Spectral Range (FSR) given by $\Delta\lambda = \lambda^2/2n_{eff}l$, effective mode index ($n_{eff}$) can be evaluated for a cavity length l. For $l \approx 21$ μm consisting of perovskite and the interlayer, λ =533 nm, $\Delta\lambda = 3.6$ nm, we get $n_{eff} = 1.87$ which agrees well with the TE0 mode index from FDTD simulation (n_{eff}^{FDTD}=1.88). This implies that the mode is predominantly trapped inside the perovskite and the additional modes due to the interlayer have negligible contributions to lasing. It is worth mentioning that the silver mirror interacts strongly only with the 2nd order wavevector from the DFB grating due to its transverse nature leaving the oscillating 1st order mode unperturbed.

As seen from the lasing spectrum in Figure 3.3b, the transverse dimensions of the cavity result in closely spaced Fabry-Pérot modes with a separation of only 5 nm. Due to this close spacing, several cavity modes coexist within the gain bandwidth of perovskite causing multi-mode lasing at a threshold of 42 μJ cm^{-2}. The stimulated emission peak comprises of 3 modes (inset of Figure 3.3b which exhibits linear increase while the other modes remain pinned. From Figure 3.3 the integrated intensity shows a characteristic lasing curve followed by a regime of gain saturation at higher excitation. The FWHM of the composite curve is 4.8 nm with individual modes having a width of 2.4 nm. As added proof for lasing, a central bright fringe is observed in the far-field emission (Figure 3.3 inset), however, due to the multimode lasing behavior the spatial coherence is low causing beam divergence.[9]

3.3. Conclusion

In this work, we combined a distributed feedback (DFB) cavity and Fabry-Pérot etalon to create a hybrid optical cavity. The inclusion of the metal reflector at the bottom interface reduces the mode volume leading to an improved Purcell factor. The increased interface reflectance also facilitates an extended photon interaction time with the perovskite gain media and augments the local photon density of states. The photon lifetime in the hybrid case is enhanced by a factor of ~2.5 resulting in an improved slope efficiency and a decreased threshold for the onset of amplification. Although the lasing linewidth is not as narrow as single-mode perovskite laser, such multimode lasers still have a relatively narrowband compared to incoherent light sources making them useful in applications where intermediate spatial coherence is required.[24]

3.4. Supplementary Information

3.4.1. Perovskite film fabrication

A 0.5 molar of n=4 PEABr: FABr: $PbBr_2$ in the ratio 2:3:4 and MACl 0.05M precursor solution was prepared in 1mL of NMP and continuously stirred on a hotplate at 60 ^oC for 2hr and left stirring overnight room at room temperature. Regular glass substrates were prepared by cleaning them in acetone, and IPA and then followed by UVO for 15 minutes. The solution was then spincoated on these substrates at 3000 rpm for 2 minutes which included chlorobenzene anti-solvent drip at the 26s mark after the start of spincoating. This was followed by annealing at 90 ^oC for 10 minutes. All the above-mentioned steps were performed in a glovebox filled with inert nitrogen gas.[4]

From further simulation (Figure S3.1), we see that a film thickness below 100 nm supports only the fundamental TE and TM modes. However, at a thickness above 100 nm TM1 mode starts to become relevant and due to its higher-order nature carries less energy than the fundamental modes.[25] Hence, we restrict the film thickness to below 100 nm.

3.4.2. Nanoimprinting

The DFB pattern on the epoxy was prepared by nanoimprint lithography. First, PDMS is used as a mold to copy the pattern from the silicon master mold, which is cured at 100 ^oC for an hour. Subsequently, this PDMS stamp is then pressed on to create the nanopattern on a substrate with epoxy (NOA 81) spincoated on it which also serves as the interlayer. With the PDMS stamp still on the substrate, it is treated under a UV lamp (365 nm peak) for 5 minutes in a glovebox filled with nitrogen gas to cure the epoxy after which the PDMS stamp can be peeled off. It should be noted that this method results in an interlayer thickness of 21 μm causing multimode behavior. Ideally, an interlayer thickness of 1-2 μm will result in single-mode operation while minimizing

SPP losses, however, we are experimentally restricted by the thickness we can achieve due to the nature of the stamping process. The DFB patterned substrate is then UVO treated for 30 minutes to improve its wettability for the subsequent perovskite spin coating.

3.4.3. Lasing measurements

PL and ASE spectra were measured using a 400 nm pulsed laser excitation with 150 fs temporal width with a 1 KHz repetition rate. The 400 nm pulse is obtained from a second harmonic generation of an 800 nm pulse from the Quantronix Integra-C laser. The emitted light is then collected by collimating and focusing the Lambertian emission into a spectrometer.

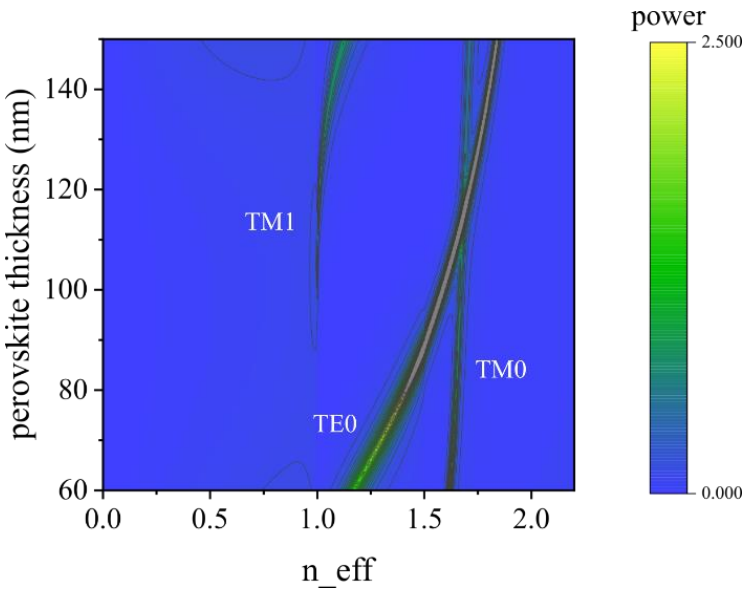

Figure S3.1: Quantized transverse modes as a function of perovskite film thickness. For a film thickness greater than 120 nm an additional TM1 mode appears reducing the mode utilation efficiency

a) b) c)

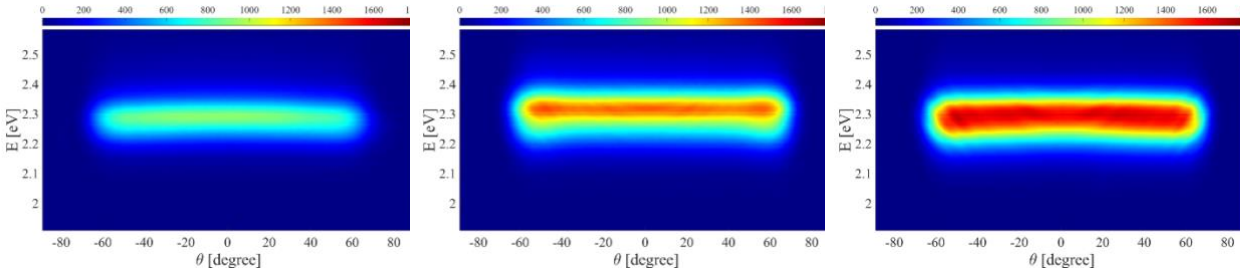

Figure S3.2: Comparing the PL intensity for perovskite on the glass-interlayer stack a) without Ag, b) with 15 nm Ag, and c) 30 nm Ag layer respectively, indicating the enhanced emission intensity due to an increase in the broadband reflectance at the interface.

3.5. References

1. Sadhanala, A. *et al.* Blue-Green Color Tunable Solution Processable Organolead Chloride-Bromide Mixed Halide Perovskites for Optoelectronic Applications. *Nano Lett* **15**, 6095–6101 (2015).

2. Zanetta, A. *et al.* Manipulating Color Emission in 2D Hybrid Perovskites by Fine Tuning Halide Segregation: A Transparent Green Emitter. *Advanced Materials* **34**, (2022).

3. Stoumpos, C. C. *et al.* Ruddlesden-Popper Hybrid Lead Iodide Perovskite 2D Homologous Semiconductors. *Chemistry of Materials* **28**, 2852–2867 (2016).

4. Lei, L. *et al.* Efficient Energy Funneling in Quasi-2D Perovskites: From Light Emission to Lasing. *Advanced Materials* **32**, 1906571 (2020).

5. Romeira, B. & Fiore, A. Purcell Effect in the Stimulated and Spontaneous Emission Rates of Nanoscale Semiconductor Lasers. *IEEE J Quantum Electron* **54**, (2018).

6. Kéna-Cohen, S., Maier, S. A. & Bradley, D. D. C. Ultrastrongly coupled exciton-polaritons in metal-clad organic semiconductor microcavities. *Adv Opt Mater* **1**, 827–833 (2013).

7. Jia, Y. *et al.* Diode-pumped organo-lead halide perovskite lasing in a metal-clad distributed feedback resonator. *Nano Lett* **16**, 4624–4629 (2016).

8. Ding, K. & Ning, C. Z. Metallic subwavelength-cavity semiconductor nanolasers. *Light: Science and Applications* vol. 1 e20–e20 Preprint at https://doi.org/10.1038/lsa.2012.20 (2012).

9. Siegman, A. E. *Lasers*. (University Science Books, 1986).

10. Larry A. Coldren, Milan L. Mashanovitch & Scott W. Corzine. *Diode Lasers and Photonic Integrated Circuits*. (Wiley, 2012).

11. Qin, L. *et al.* Enhanced amplified spontaneous emission from morphology-controlled organic–inorganic halide perovskite films. *RSC Adv* **5**, 103674–103679 (2015).

12. Misirpashaev, T. Sh. & Beenakker, C. W. J. Lasing threshold and mode competition in chaotic cavities. *Phys Rev A (Coll Park)* **57**, 2041–2045 (1998).

13. Tessler, N. Lasers Based on Semiconducting Organic Materials. *Advanced Materials* **11**, 363–370 (1999).

14. Berini, P. & De Leon, I. Surface plasmon–polariton amplifiers and lasers. *Nat Photonics* **6**, 16–24 (2012).

15. van der Pol, T. P. A., Datta, K., Wienk, M. M. & Janssen, R. A. J. The Intrinsic Photoluminescence Spectrum of Perovskite Films. *Adv Opt Mater* **10**, (2022).

16. Hayenga, W. E. & Khajavikhan, M. Unveiling the physics of microcavity lasers. *Light: Science and Applications* vol. 6 e17091–e17091 Preprint at https://doi.org/10.1038/lsa.2017.91 (2017).

17. Yokoyama, H. Physics and Device Applications of Optical Microcavities. *Science (1979)* **256**, 66–70 (1992).

18. Haug, H. Quantum-Mechanical Rate Equations for Semiconductor Lasers. *Physical Review* **184**, 338–348 (1969).

19. Berden, G., Peeters, R. & Meijer, G. Cavity ring-down spectroscopy: Experimental schemes and applications. *Int Rev Phys Chem* **19**, 565–607 (2000).

20. Zeng, S., Zhao, X., Zhu, Y., Dove, C. & Zhu, L. Slope efficiency of integrated external cavity hybrid lasers: A general model and analysis. *AIP Adv* **9**, (2019).

21. Muravitskaya, A. *et al.* Engineering of the Photon Local Density of States: Strong Inhibition of Spontaneous Emission near the Resonant and High-Refractive Index Dielectric Nano-objects. *The Journal of Physical Chemistry C* **126**, 5691–5700 (2022).

22. Fu, X. *et al.* Mode Dispersion in Photonic Crystal Organic Light-Emitting Diodes. *ACS Appl Electron Mater* **2**, 1759–1767 (2020).

23. Mi, Y. *et al.* Fabry–Pérot Oscillation and Room Temperature Lasing in Perovskite Cube-Corner Pyramid Cavities. *Small* **14**, (2018).

24. Ahmad, A., Jayakumar, N. & Ahluwalia, B. S. Demystifying speckle field interference microscopy. *Sci Rep* **12**, 10869 (2022).

25. Wolfgang Demtröder. *Atoms, Molecules and Photons*. (Springer).

CHAPTER 4: Optical manipulation of cooperative emission in Ruddlesden-Popper perovskites

Superfluorescence (SF) is a non-linear and stochastic spontaneous emission process in which the emitter-field coupling induces cooperative effects such that the nature of the light thus emitted is fundamentally different from the well-established spontaneous emission from independent emitter ensemble. We recently reported on superfluorescent light emission in solution-processed perovskite thin films at room temperatures offering the possibility to study this incipient phenomenon on a well-established material platform. SF is a cooperative emission process where the initially incoherent excited emitter population undergoes phase synchronization initiated by quantum fluctuations causing the system to emit coherent and intense bursts of radiation on ultrafast timescales. The system needs to synchronize rapidly to overcome dephasing which can especially be detrimental for a solid-state system, but the strong many-body coulomb interaction in hybrid perovskites is responsible for establishing emitter correlations on an ultrafast scale. However, because of the inherent stochastic nature it has proved challenging to develop applications that harness the many-body physics of SF. Here we report on a statistically deterministic way to manipulate the time dynamics of SF by encapsulating the active perovskite gain media in a low-Q cavity. We illustrate how a continuous modulation of the cavity detuning with respect to the material's SF peak facilitates control over the time evolution of the pulse. This principle relies on modifying the Purcell factor responsible for the spontaneous emission, which is the initial system response that precedes phase synchronization and SF burst. The time-resolved Kerr gate data reveals a strong dependence on the detuning with clear discerning evidence in the delay time and the temporal pulse width of the SF burst. For the sample with zero cavity detuning, the delay occurs at a later time of 9.1 ps compared to 7.5 ps for the planar substrate sample at a

threshold fluence of 18 $\mu J.cm^{-1}$. The difference in delay time further widens as a function of the excitation fluence with the time difference being more than 4 ps at a fluence value of 48 $\mu J.cm^{-1}$. Meanwhile, the temporal pulse width at the threshold fluence for the planar and the on-resonant sample is 3.2 ps and 4 ps respectively, and this gap widens significantly as a function of the fluence being 2.1 ps and 3.5 ps at 48 $\mu J.cm^{-1}$. Additionally, using the pulse broadening data the group delay dispersion (GDD) value was extracted as a function of the fluence for the perovskite material under investigation providing further insights on pulse propagation behavior in these soft materials.

4.1. Introduction

The self-consistent interaction of individual emitters and the radiation field on a mesoscopic scale has been the subject of intense theoretical and experimental studies. The optical properties of N-oscillator interacting with each other through the common radiation mode are substantially different from that of the N-oscillator acting independently. At the initial moment $t = 0$ for superfluorescence, a non-equilibrium inverted state of active emitters is prepared through incoherent pumping i.e., degenerate electron-hole pair states in the gain medium. In such a system the collective coherent oscillator field is initially absent and develops over time due to atom-field correlations which is a distinguishing characteristic of SF when compared to amplified spontaneous emission (ASE) and superradiance (SR).[1] Observation of SF is dependent upon simultaneously present conflicting mechanisms, one where the time required for the emitter ensemble to develop phase coherence competes against the time it takes for scattering events and non-linear motion of the charge carrier to scramble the phase memory. An approximate comparison can be made based on the following time scales for SF emission, i) the inhomogeneous dephasing time T_2^*, defined by the spread of the probability distribution of the eigenfrequency of

the emitter ensemble, and ii) the characteristic decay time for SF τ_{SR}, and the delay time τ_d. Based on these timescales and first-principle calculations, observation of SF is conditional upon the expression: $(\tau_{SR}\tau_d)^{1/2} < T_2^*$ i.e., the product of the time required for phase synchronization and the subsequent relaxation should be smaller than the system's dephasing time.[2–4]

In his original version, Dicke assumed a simplified model of the emitters being confined in a volume much less than the emission wavelength to minimize the spatial variation in the electric field strength over the active volume.[5] This implies that the vector potential appearing in the Hopfield Hamiltonian is homogeneous throughout the volume of interest and imposes phase correlations due to the system of emitter being invariant under emitter permutation.[6] After a finite time has elapsed after the initial excitation, the system undergoes a phase transition and eventually forms a strongly correlated Dicke state with in-phase oscillation of the dipole moments.[5,7] Initially SF was thought to be a classical non-equilibrium phase transition process of the second-order, however after subsequent refinement to the Hamiltonian it was realized to be a quantum phase transition brought forth by quantum fluctuations rather than thermal fluctuations.[8,9] The stochastic nature of these quantum fluctuations leading to the characteristic phase synchronization in a large Hilbert space makes it impractical to write down a thorough analytical and closed-form set of equations of motion for the system. However, attempts have been made that rely on mathematical approximations that provide critical insight into the dynamical behavior of this non-Hermitian system including Liouville-Neumann equations based on the Heisenberg equation of motion and density matrix formalism,[10,11] Monte-Carlo[12,13] simulations along with perturbative cluster expansion[14] techniques. However, these and other approaches have underlying assumptions and boundary conditions that restrict a comprehensive understanding of SF making it inexplicable to

include phase-locking, diffraction, and pulse propagation effects in an extended system under a unified model.

Despite the complexity of the process, there are several experimental demonstrations of SF in gas and liquid phase systems. It is however difficult to realize a Dicke state in a solid-state extended system due to strong coulomb potential and scattering process that can destroy the intricate dipole-dipole interaction and inhibit phase transformation. Nonetheless, we recently reported superfluorescence phase transition in metal halide perovskites at room temperatures.[15] Given the ease of film fabrication and the wide variability in processing conditions it's relatively easy to replicate quantum-well (QW) type structure in solution-processed Ruddlesden-Popper (RP) phase of perovskites otherwise usually only seen in traditional inorganic semiconductor. The well barrier consists of a bulky organic cation (A') while the well itself is made from octahedral BX_6^{2-}, B is the Pb component, X is the halide component with A occupying the space between neighboring octahedra. The overall chemical structure is $A'_2A_{n+1}B_nX_{3n+1}$ where n is the number of continuous octahedral sheets of perovskite cleaved by the barrier layer. The strong spatial confinement of the QW structure lends large exciton binding energy[16–18] which theoretically should support a large superradiant decay rate and makes the charge carriers immune to phonon scattering events to some degree.[19] The large Fermi degeneracy leads to strong exchange potential with many-body interactions favoring spontaneous and cooperative emission. When combined with the large decay rate and the anharmonic band-diagram[20,21] supporting the Dicke state,[22] perovskites are an ideal material testbed for SF investigation.

To develop a non-classical coherent light source based on SF phenomenon it is necessary to have control over the characteristic timescales which is lacking due to the inherent ambiguity in the process.[23] The random nature of the temporal processes was first demonstrated in a statistical

study of single shot SF pulse from O_2^- center in single crystal KCl where the delay time and the pulse width were found to have a significant deviation of a few ns between shots.[24] As established, only systems with a low decoherence rate can exhibit energy damping due to Superfluorescence and an effective way to control the damping magnitude is through an optical cavity that enforces light-matter interaction through the quantized cavity modes. This is known as the Arecchi-Courtens condition[25] and is a major factor when studying extended systems in a cavity where the photon loss rate can be effectively controlled through cavity parameters.[26] Tuning the cavity resonance to the material's emission provides a continuous modulation scheme to regulate the otherwise random SF pulse evolution. Such modulation capability is critical for implementing applications based on SF such as potential substitute for traditional lasing devices,[27,28] as a nonclassical light source,[29] and for quantum computing where a deterministic control over spontaneous emission is required.[30,31] In this work we demonstrate optical control of the expectation value of delay time and pulse width in solution solution-processed RP phase of metal halide perovskite films encapsulated in an optical cavity. To ensure the emission is spontaneous and cooperative rather than stimulated, we operate in the bad cavity limit in which photons can leak out acting as a decay channel providing the required damping and preventing crossover to the lasing regime.

4.2. Results

Figure 4.1: Steady-state PL spectra (a) for a reference planar sample and (b) for the sample encapsulated in a DFB cavity with Λ=300 nm. The inset shows the quadratic intensity scaling of the SF emission peak which is characteristic of cooperative emission. (c) PL spectra for a 1-D DFB grating with Λ=330 nm in resonance with the SF emission. At below threshold fluence (12.22 $\mu J.cm^{-2}$) there's a clear divergence in the PL lineshape due to diffraction from the grating according to Bragg's law. Inset: topographical AFM image of the DFB grating prepatterned onto a glass substrate. (d) Optical Kerr-gate setup for measuring the time-resolved evolution of the SF peak with zero delay defined as the instant both the emission and the gate beam are simultaneously incident on the Kerr medium. The two orthogonally oriented polarizer ensures no light passes through to the detector unless in the presence of the gate beam.

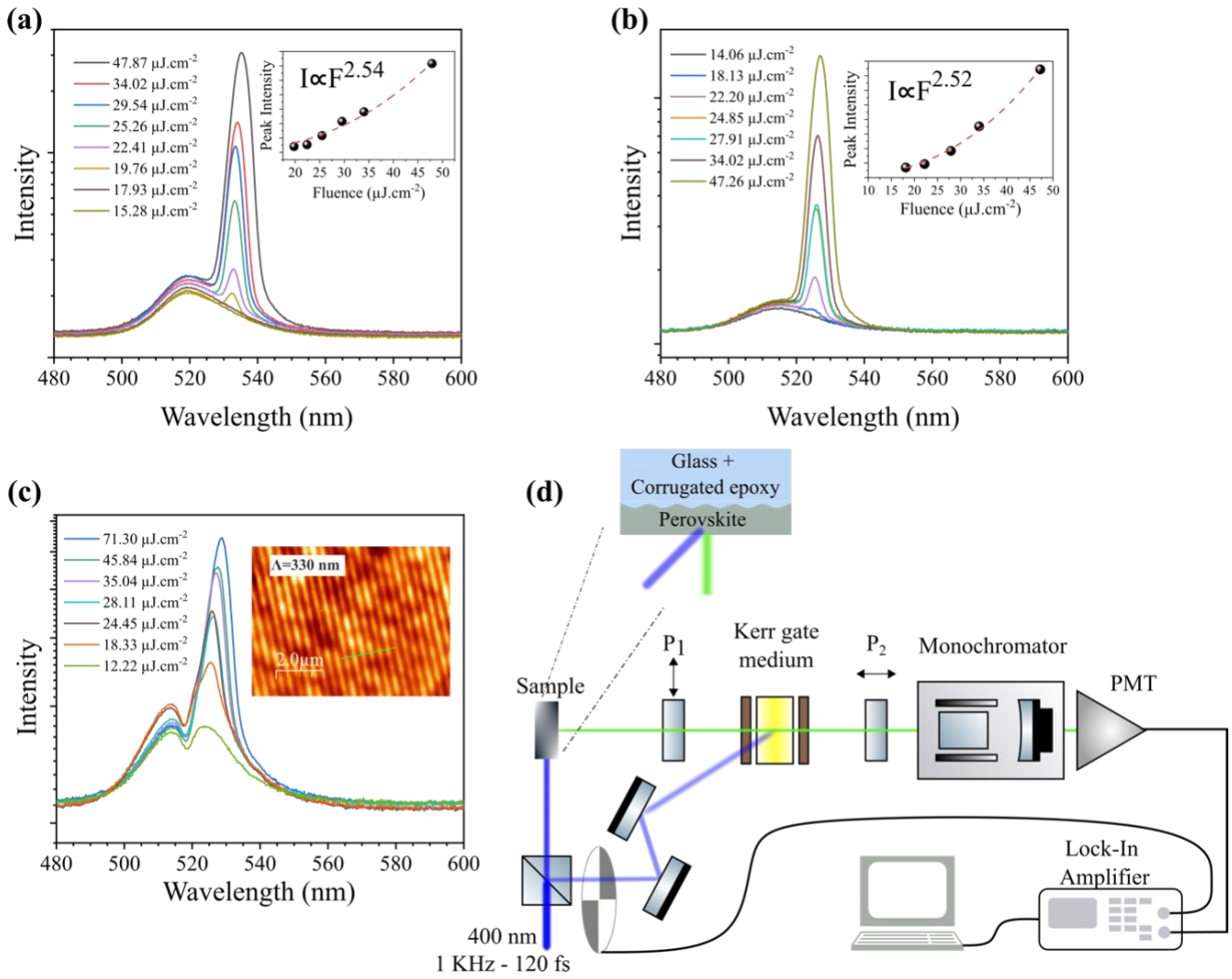
(a)
47.87 µJ.cm-2
34.02 µJ.cm-2
29.54 µJ.cm-2
25.26 µJ.cm-2
22.41 µJ.cm-2
19.76 µJ.cm-2
17.93 µJ.cm-2
15.28 µJ.cm-2
I∝F2.54
Peak Intensity
Fluence (µJ.cm-2)
Intensity
Wavelength (nm)
(b)
14.06 µJ.cm-2
18.13 µJ.cm-2
22.20 µJ.cm-2
24.85 µJ.cm-2
27.91 µJ.cm-2
34.02 µJ.cm-2
47.26 µJ.cm-2
I∝F2.52
Peak Intensity
Fluence (µJ.cm-2)
Intensity
Wavelength (nm)
(c)
71.30 µJ.cm-2
45.84 µJ.cm-2
35.04 µJ.cm-2
28.11 µJ.cm-2
24.45 µJ.cm-2
18.33 µJ.cm-2
12.22 µJ.cm-2
Λ=330 nm
2.0µm
Intensity
Wavelength (nm)
(d)
Glass + Corrugated epoxy
Perovskite
Sample
P1
Kerr gate medium
P2
Monochromator
PMT
Lock-In Amplifier
400 nm
1 KHz - 120 fs

According to Fermi's Golden rule, the emission process is not an intrinsic property but is rather influenced by the strength of the interaction between the material's dipole moment and the local electromagnetic field reservoir modulated by an optical cavity.[32] Therefore under weak coupling the enhancement in the optical transition probability of a system of initially excited emitters depends on its electromagnetic environment through the density of states as outlined by the Purcell effect.[33,34] A more comprehensive expression for the emission enhancement is given by,[35,36]

$$F_P = \left[\frac{3}{4\pi^2}\cdot\frac{Q}{V}\cdot\left(\frac{\lambda}{n}\right)^3\right]\left[\frac{|d.f(r_e)|^2}{|d|^2}\right]\left[\frac{\Delta\omega_c^2}{4(\omega_e-\omega_c)^2+\Delta\omega_c^2}\right]$$

The first term is the simplified form of the Purcell factor depending on the quality factor Q and the mode volume V of an optical cavity. It shows the maximum attainable value under resonance for a one-dimensional chain of dipole located at the field antinode position. The second term is the linear dipole approximation that depends on the weighted oscillator strength depending on the field distribution $f(r_e)$. The last term in the bracket is the Lorentzian distribution of the homogeneous emitters centered around its resonance frequency ω_e with a full-width-at-half maximum of $\Delta\omega_c$ and ω_c is the cavity resonance. Assuming other terms remain constant, the Purcell factor can be influenced by the detuning of the cavity from the emitter transition line thus giving indirect access to the spontaneous emission rate and by extension to the superfluorescence time dynamics. Therefore, by encapsulating the system in a cavity with a confined mode volume we can in theory enhance the light-matter coupling and consequently accelerate the dipole oscillation between the ground and the excited state.[37] For the perovskite film the characteristic SF decay time τ_{SR} is reduced by a factor equal to the cavity finesse compared to free-space emission τ_{SE} resulting in a significantly different superfluorescence evolution.[38,39]

To implement this experimentally we spincoated perovskite on a prefabricated one-dimensional distributed feedback grating (DFB) with a lattice constant (Λ) of 300 nm and 330 nm corresponding to a resonant wavelength of 475 nm and 525 nm respectively (Figure S4.1). The photoluminescence (PL) spectra for a planar reference sample (Figure 4.1a) and for the pre-patterned substrates Λ=300 nm (Figure 4.1b) and Λ=330 nm (Figure 4.1c) corresponding to the off-resonant and resonant behavior respectively with a topographical AFM map of the DFB cavity shown in Figure 4.1 inset. At lower fluences the emission is dominated by excitonic interband recombination with a peak at around 518 nm, while at fluences above the threshold a secondary SF peak appears redshifted relative to the PL at 527 nm. For the on-resonant sample, the additional peak overlapping with the PL peak, seen clearly at below the threshold fluence in Figure 4.1c, corresponds to the diffracted light of wavevector $\vec{k} = \vec{k_i} \pm m\,2\pi/\Lambda$ along the normal direction as per Bragg's law of diffraction. To ensure that the system does not cross over to stimulated emission regime the cavity coherence time has to be negligible compared to the material's radiation lifetime so that the photons can leak out [40–42] for the system to operate in the overdamped SF regime – also known as the 'bad' cavity limit.[39,43] A more quantitative definition of a bad cavity in the context of SF requires the damping time $2Q/\omega$ to be less than the superradiance time τ_{SR}.[44] For the case of the on-resonant cavity with a $Q \approx 50$ the damping time is $\sim 0.3\,fs$ which is significantly less than τ_{SR} of a few ps. Furthermore, due to the emitter ensemble having a constant phase relation the radiation intensity adds coherently and scales quadratically as N^2 where N is the number of actively participating dipoles.[45] The inset in Figure 4.1(a-b) shows the quadratic scaling of intensity as a function of fluence which has a one-to-one correlation with the emitter population. The same intensity analysis is not performed for the on-resonant sample due to the

additional peak from cavity diffraction overlapping the SF peak requiring a complex deconvolution process, however the same trend should hold.

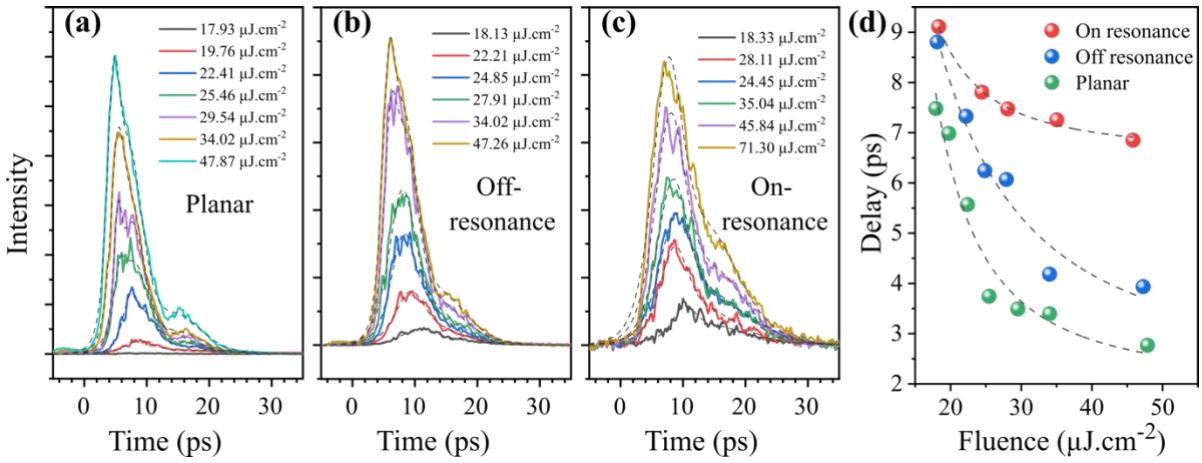

Figure 4.2: Time-resolved Kerr gate data for (a) reference planar sample, (b) the off-resonant sample, and (c) the on-resonant sample with a grating pitch of Λ=300 nm and Λ=330 nm respectively. The SF wavepacket follows a secant-hyperbolic pulse shape with distinct values for the zero-delay and the pulse width among the different samples. (d) The zero-delay is plotted as a function of the excitation fluence and follows $\tau_{SR}\log(N)/N$ law according to which the on-resonant sample has the largest delay followed by the off-resonant and the planar sample. The data is fitted (dashed lines) to extract the superfluorescent time relaxation constant τ_{SR}.

Next, we performed time-resolved Kerr gate experiment (Figure 4.1d) to study the time evolution of the different samples. To perform the experiment the monochromator was fixed on the SF peak at 527 nm the output of which is connected to a PMT and through a delay stage the time evolution of the peak was recorded. The time trace in Figure 4.2(a-c) were averaged over multiple scans to avoid shot-to-shot variations because even if the system is prepared identically the collective radiative emission properties can be unpredictable due to quantum uncertainties.[46] Zero-delay was defined as the time instant at which the spontaneous emission signal begins to rise,

and the delay time (τ_d) was fixed at the peak of the pulse modeled as a secant hyperbolic function.[47] All the samples under study had the same threshold for SF of $\sim 18\,\mu J.cm^{-2}$ to ensure a fair comparison. In the visible spectrum the dephasing process due to Doppler broadening and other nonlinearities can be quite significant[48] compared to longer wavelengths as observed in gas phase SF demonstration.[49] As a response the characteristic timescale for a solid-state system is in the picosecond regime compared to nanoseconds in gases.[50–52]

At the threshold fluence the relatively high signal undulations compared to the data below the threshold is an indication of the phase transitions driven by the quantum fluctuations which eventually fades away at slightly higher fluences. At fluences above the threshold the pulse intensity at *t=0* is the same as spontaneous emission, and the maximum SF intensity occurs after a delay time which corresponds to the formation and subsequent relaxation of coherent polarization.[53] At even higher fluence ($F > 30\,\mu J cm^{-2}$), one can observe a secondary peak in the Kerr intensity data which is apparent in the planar reference sample. The reason for the secondary peaks in the Kerr data is due to the reabsorption and coherent reamplification of the pulse as it propagates through the relaxed medium.[53,54] As a consequence the medium's polarization has spatial variations and evolves at different times resulting in the so called ringing effects.[8,55] Meanwhile the proximity of the two peaks relative to each other depends on the excitation geometry and more specifically the Fresnel number $F = \pi r_o^2/\lambda L$ (r_o and L are the radius and length of the excited sample).[6] For the sample enclosed inside the cavity the effective length L of the inverted medium increases due to multiple reflections at the end facet of the mirror and consequently the Fresnel number decreases. For an excitation spot size of 2 mm the Fresnel number is quite large but with an increase in the effective length $F \to 1$ resulting in the decreased temporal distance between the individual burst and approaching single pulse SF behavior.[56,57]

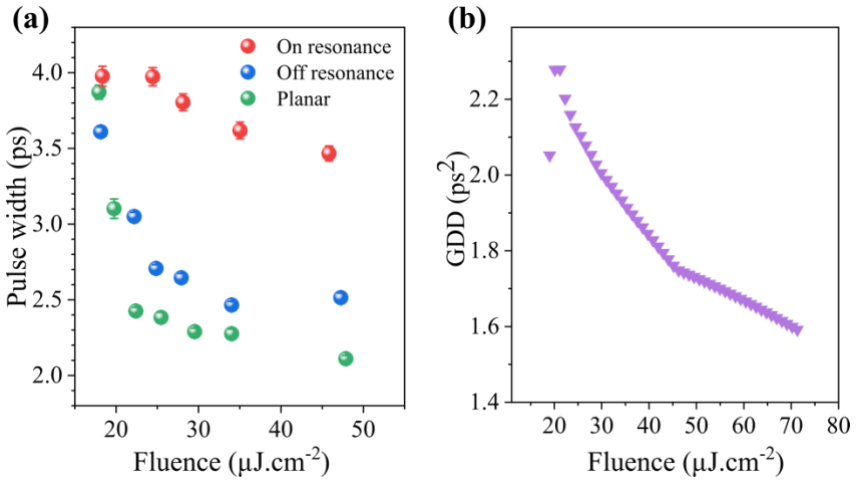

Figure 4.3: Pulse width characteristics. (a) Compares the pulse width for the different samples. The Λ=330 nm sample has the largest pulse width owing to the resonant behavior and the temporal broadening due to chromatic group velocity dispersion (GVD). (b) A positive group delay dispersion (GDD; $GDD = GVD \times L$) as a function of the excitation fluence having a negative slope implying the less frequent roundtrips required to undergo SF phase transition.

The fluctuations in the early stages of the macroscopic dipole formation translate to fluctuation in the delay time.[58] From the Kerr data it is evident that the delay time decreases as a function of increased excitation fluence, a feature unique to SF evolution.[59–61] Quantitatively this variation in the delay time can be described as a functional integral over the zero-point fluctuations resulting in the following expectation value $\langle t_d \rangle = \tau_{SR} \log N/N$.[62] Since the incident fluence is directly proportional to the excited emitter population N, based on the above equation τ_{SR} can be extracted from the Kerr data as shown in Figure 4.2d. For the cavity in resonance, the pulse appears at a later delay which is attributed to the Purcell factor enhancement of the spontaneous emission relaxation time which accelerates the synchronization process $\tau_{SR} = 65.4$ ps compared to the reference sample with a $\tau_{SR} = 133.2$ ps. Meanwhile for the off-resonant sample $\tau_{SR} = 466.6$ ps which validates the Purcell factor inhibition of the spontaneous emission rate.

Notice from the Kerr gate data that the SF pulse originating from an active medium inside a cavity is temporally stretched and has a larger pulse width compared to the reference sample as shown in Figure 4.3a. This is attributed to the material dispersion that stretches the pulse as it undergoes multiple reflections inside the cavity. Additionally, the pulse width decreases as a function of the excitation intensity implying fewer round trips are required to attain the same mean photon number inside the cavity. The sample that is in resonance with the cavity has its pulse stretched the most in comparison to the planar and the off-resonant cavities which have similar pulse widths at the threshold fluence. The pulse broadening can be quantified by group delay dispersion effects (GDD) which is defined as the second-order derivative of the spectral phase evaluated at a central frequency $\beta_2 = \frac{\partial^2 \varphi}{\partial \omega^2}$ and is a quantitative measurement for chromatic dispersion or frequency chirp without affecting the pulse spectrum. For second-order dispersion effects to have a notable effect on the pulse shape the propagation length L of the pulse must be comparable to or larger than the dispersion length L_D.[63,64] Since the lateral dimension of the cavity provides the required propagation length the SF pulse is stretched out at the output side. Unfortunately, it is not quite easy to evaluate the integral for the SF pulse dispersion effects of a secant hyperbolic pulse,[65] and so to a very good first-order approximation a gaussian wavepacket is used instead. For a normalized input Gaussian pulse, $U(0,T) = \exp\left(-\frac{T^2}{2T_o^2}\right)$ of width T_o ($1/e$ intensity point) and propagating through a dispersive media for a distance z, the pulse gets stretched to width T_1 according to

$$T_1(z) = T_o\left[1 + \frac{GDD^2}{T_o^4}\right]^{1/2}$$

We use this expression to interpolate the GDD for the on-resonant sample as a function of the excitation fluence as shown in Figure 4.3b for an input reference pulse width of the planar sample.

The positive and relatively high GDD value is attributed in part to the multiple reflections inside the cavity increasing the pulse propagating length but more importantly to the high third-order nonlinearities in the RP phase of perovskites.[66,67] Dispersion plays a critical role in optical pulse propagation and therefore managing the several constituent spectral components that have their group velocity is important.

4.3. Conclusion

Superfluorescence is an exotic quantum process described by a macroscopic wavefunction owing to the many-body interaction with potential application in quantum information processing and novel light sources.[15,68] Metal halide perovskites presents a rich platform to study many-body correlation effects due to their strong columbic and lattice interaction however due to the stochastic origin of the SF pulse its realization into technologically relevant application has been hindered. In this work, we demonstrated statistical control over the expectation value of the delay time in the visible spectrum by utilizing a low-Q distributed feedback cavity. By tuning the cavity resonance to the materials resonance, the relaxation time of individual emitters can be engineered through the Purcell factor based on the detuning. This lifetime engineering is reflected in the Kerr dynamics of the SF peak where the on-resonant cavity has a significantly large delay time and pulse width when compared to the planar reference sample. Additionally, we also quantify the pulse dispersion as a function of the fluence which is a critical parameter to enable dispersion-less soliton propagation in perovskite medium. The fact that the SF characteristics – both delay time and pulse width – can be altered through a cavity provides a novel way to manipulate this quantum macroscopic phenomenon and as a result making it feasible to incorporate into application focused devices.

4.4. Supplementary Information

4.4.1. Film preparation

BABr (99.99%, metal basis), CsBr (99.999%, metal basis), $PbBr_2$ (99.999%, metal basis) from Sigma Aldrich and were mixed in the ratio 0.4:1:1 in DMSO for a 0.5 molar concentration. To this solution 5% of CsMeS salt was added with respect to $PbBr_2$ molar ratio to improve the film's morphology. The as-prepared solution was stirred on a hot plate at 60^{o} C for 2 hours and left stirring at room temperature overnight.

Glass substrates were cleaned using acetone followed by an IPA bath in an ultrasonicator for 15 minutes each. To improve wettability the glass substrate was treated with UVO plasma for 15 minutes. The solution was then spincoated on the cleaned glass substrate at 4000 rpm and chlorobenzene was dripped after 15s had elapsed from the initial spincoating for a cumulative time of 60s. The film was annealed at 90^{o} C for 10 minutes. The film was then encapsulated to prevent exposure to the ambient using another piece of hollowed glass. All the above steps were performed in a nitrogen gas-filled glovebox.

4.4.2. Sample preparation

To prepare the DFB grating, PDMS was mixed with 10% initiator and poured over the silicon master mold with specified grating pitch Λ. The PDMS was then cured on a hotplate at 80^{o} C for 20 minutes such that the pattern was copied onto the PDMS. A cleaned glass substrate was then spincoated with NOA 81 at 4000 rpm for 30s and the PDMS stamp was carefully pressed on the substrate and cured in UVO for 3 minutes. The PDMS stamp can then be peeled off with the cured and patterned epoxy left behind on the glass substrate.

To measure the cavity resonance, we used a home-built angle-resolved photoluminescence (ARPL) setup with the recorded spectra shown in Figure S4.3.

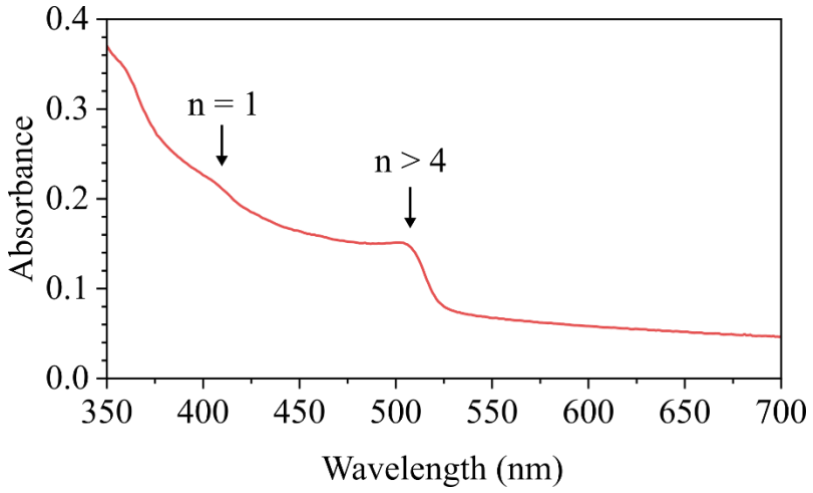

Figure S4.1: UV-VIS spectra of the quasi-2D perovskite with RP phase showing the 3D domain ($n > 4$) and the pure 2D domain ($n = 1$).

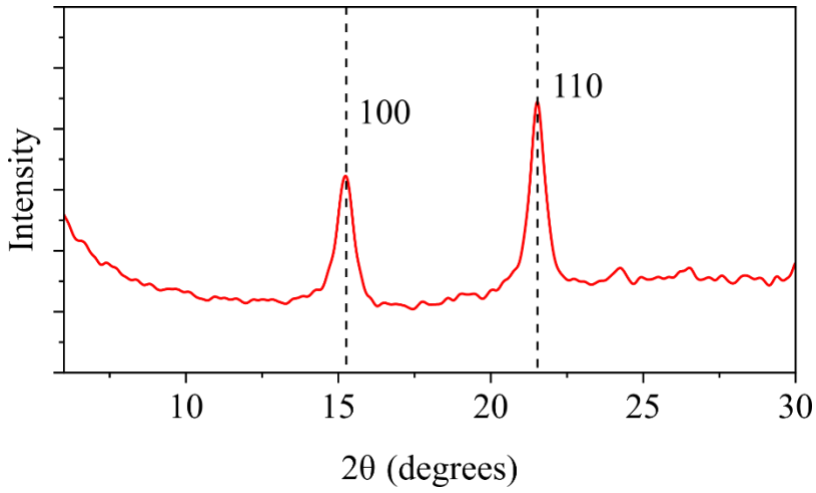

Figure S4.2: XRD data showing the (100) and (110) plane of the spincoated film

(a) (b)

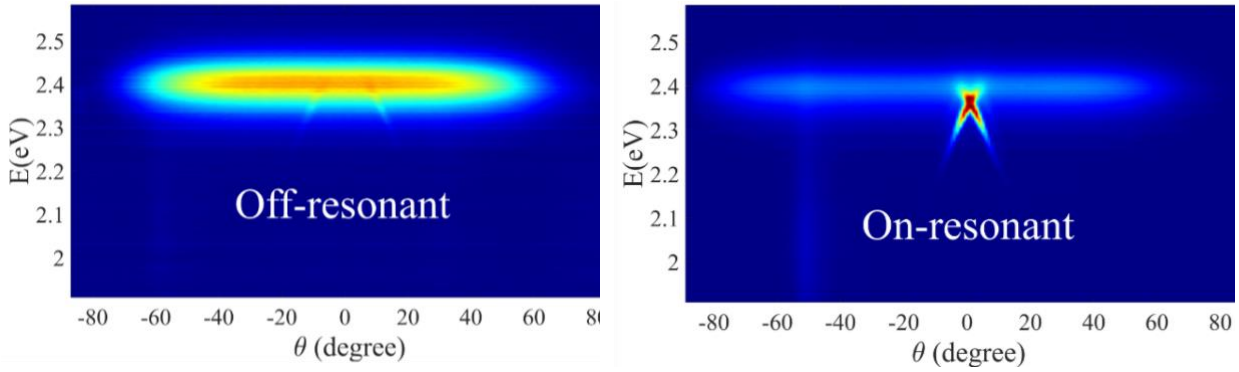

Figure S4.3: Shows the ARPL plot for the off-resonant ($\Lambda = 300\ nm$) and the on-resonant ($\Lambda = 300\ nm$) DFB grating. (a) The PL background is obvious in the off-resonant case at around 2.4 eV with a hint of cavity resonance as seen by the crossing on either side of the normal viewing angle (0 degrees). (b) the crossing feature at 2.38 eV is seen at a normal viewing angle after the PL background is suppressed.

4.5. References

1. Auffèves, A., Gerace, D., Portolan, S., Drezet, A. & França Santos, M. Few emitters in a cavity: from cooperative emission to individualization. *New J Phys* **13**, 093020 (2011).

2. Feld, M. S. & MacGillivray, J. C. Superradiance. in 7–57 (1980). doi:10.1007/978-3-642-81495-2_2.

3. Andreev, A. V, Emel'yanov, V. I. & Il'inskiĭ, Y. A. Collective spontaneous emission (Dicke superradiance). *Soviet Physics Uspekhi* **23**, 493–514 (1980).

4. Schuurmans, M. F. H., Vrehen, Q. H. F., Polder, D. & Gibbs, H. M. Superfluorescence. in 167–228 (1982). doi:10.1016/S0065-2199(08)60069-X.

5. Dicke, R. H. Coherence in spontaneous radiation processes. *Physical Review* **93**, 99–110 (1954).

6. Gross, M. & Haroche, S. Superradiance: An essay on the theory of collective spontaneous emission. *Phys Rep* **93**, 301–396 (1982).

7. Greiner, C., Boggs, B. & Mossberg, T. W. Superradiant Emission Dynamics of an Optically Thin Material Sample in a Short-Decay-Time Optical Cavity. *Phys Rev Lett* **85**, 3793–3796 (2000).

8. Haake, F. *et al.* Fluctuations in Superfluorescence. *Phys Rev Lett* **42**, 1740–1743 (1979).

9. Watson, E. A. *et al.* Quantum fluctuations and transverse effects in superfluorescence. *Phys Rev A (Coll Park)* **27**, 1427–1434 (1983).

10. Lax, M. & Louisell, W. H. Quantum Noise. XII. Density-Operator Treatment of Field and Population Fluctuations. *Physical Review* **185**, 568–591 (1969).

11. Sitek, A. & Manolescu, A. Dicke states in multiple quantum dots. *Phys Rev A (Coll Park)* **88**, 043807 (2013).

12. Rai, J. & Bowden, C. M. Quantum-statistical analysis of superfluorescence and amplified spontaneous emission in dense media. *Phys Rev A (Coll Park)* **46**, 1522–1529 (1992).

13. Meiser, D. & Holland, M. J. Steady-state superradiance with alkaline-earth-metal atoms. *Phys Rev A* **81**, (2010).

14. Carmele, A., Knorr, A. & Richter, M. Photon statistics as a probe for exciton correlations in coupled nanostructures. *Phys Rev B* **79**, 035316 (2009).

15. Biliroglu, M. *et al.* Room-temperature superfluorescence in hybrid perovskites and its origins. *Nat Photonics* **16**, 324–329 (2022).

16. Blancon, J.-C. *et al.* Scaling law for excitons in 2D perovskite quantum wells. *Nat Commun* **9**, 2254 (2018).

17. Gao, X. *et al.* Ruddlesden–Popper Perovskites: Synthesis and Optical Properties for Optoelectronic Applications. *Advanced Science* **6**, (2019).

18. Ding, Y.-F. *et al.* Strong thickness-dependent quantum confinement in all-inorganic perovskite Cs_2PbI_4 with a Ruddlesden–Popper structure. *J Mater Chem C Mater* **7**, 7433–7441 (2019).

19. Hanamura, E. Rapid radiative decay and enhanced optical nonlinearity of excitons in a quantum well. *Phys Rev B* **38**, 1228–1234 (1988).

20. Li, Z.-G. *et al.* Origin of Phase Transitions in Inorganic Lead Halide Perovskites: Interplay between Harmonic and Anharmonic Vibrations. *ACS Energy Lett* **8**, 3016–3024 (2023).

21. Cohen, A. *et al.* Diverging Expressions of Anharmonicity in Halide Perovskites. *Advanced Materials* **34**, (2022).

22. Nefedkin, N. E. *et al.* Superradiance of a subwavelength array of classical nonlinear emitters. *Opt Express* **24**, 3464 (2016).

23. Vrehen, Q. H. F. & Schuurmans, M. F. H. Direct measurement of the effective initial tipping angle in superfluorescence. *Phys Rev Lett* **42**, 224–227 (1979).

24. Florian, R., Schwan, L. O. & Schmid, D. Time-resolving experiments on Dicke superfluorescence of O2- centers in KCl. Two-color superfluorescence. *Phys Rev A (Coll Park)* **29**, 2709–2715 (1984).

25. Arecchi, F. T. & Courtens, E. Cooperative Phenomena in Resonant Electromagnetic Propagation. *Phys Rev A (Coll Park)* **2**, 1730–1737 (1970).

26. Temnov, V. V. & Woggon, U. Superradiance and subradiance in an inhomogeneously broadened ensemble of two-level systems coupled to a low-Q cavity. *Phys Rev Lett* **95**, (2005).

27. Strauf, S. *et al.* Self-Tuned Quantum Dot Gain in Photonic Crystal Lasers. *Phys Rev Lett* **96**, 127404 (2006).

28. Biolatti, E., Iotti, R. C., Zanardi, P. & Rossi, F. Quantum Information Processing with Semiconductor Macroatoms. *Phys Rev Lett* **85**, 5647–5650 (2000).

29. Drummond, P. D. & Raymer, M. G. Quantum theory of propagation of nonclassical radiation in a near-resonant medium. *Phys Rev A (Coll Park)* **44**, 2072–2085 (1991).

30. Ortiz-Gutiérrez, L. *et al.* Experimental Fock-State Superradiance. *Phys Rev Lett* **120**, 083603 (2018).

31. Imamog¯lu, A. *et al.* Quantum Information Processing Using Quantum Dot Spins and Cavity QED. *Phys Rev Lett* **83**, 4204–4207 (1999).

32. Yamamoto, Y. & Slusher, R. E. Optical Processes in Microcavities. *Phys Today* **46**, 66–73 (1993).

33. Purcell, E. M. Spontaneous Emission Probabilities at Radio Frequencies. *Physical Review* **69**, 681–681 (1946).

34. Agio, M. & Cano, D. M. Nano-optics: The Purcell factor of nanoresonators. *Nat Photonics* **7**, 674–675.

35. Sauvan, C., Hugonin, J. P., Maksymov, I. S. & Lalanne, P. Theory of the Spontaneous Optical Emission of Nanosize Photonic and Plasmon Resonators. *Phys Rev Lett* **110**, 237401 (2013).

36. Gerard, J.-M. & Gayral, B. Strong Purcell effect for InAs quantum boxes in three-dimensional solid-state microcavities. *Journal of Lightwave Technology* **17**, 2089–2095 (1999).

37. Ciuti, C., Bastard, G. & Carusotto, I. Quantum vacuum properties of the intersubband cavity polariton field. *Phys Rev B* **72**, 115303 (2005).

38. Moi, L. *et al.* Rydberg-atom masers. I. A theoretical and experimental study of super-radiant systems in the millimeter-wave domain. *Phys Rev A (Coll Park)* **27**, 2043–2064 (1983).

39. Bonifacio, R. & Lugiato, L. A. Superfluorescence in a cavity. *Opt Commun* **47**, 79–83 (1983).

40. Kaluzny, Y., Goy, P., Gross, M., Raimond, J. M. & Haroche, S. Observation of Self-Induced Rabi Oscillations in Two-Level Atoms Excited Inside a Resonant Cavity: The Ringing Regime of Superradiance. *Phys Rev Lett* **51**, 1175–1178 (1983).

41. Kirton, P. & Keeling, J. Superradiant and lasing states in driven-dissipative Dicke models. *New J Phys* **20**, 15009 (2018).

42. Sezaki, R., Ishikawa, A., Miyajima, K. & Kobayashi, K. Theory of superfluorescence-laser crossover in a cavity QED system. *Appl Phys A Mater Sci Process* **123**, (2017).

43. Mascarenhas, E., Gerace, D., Santos, M. F. & Auffèves, A. Cooperativity of a few quantum emitters in a single-mode cavity. *Phys Rev A* **88**, (2013).

44. Bazhanov, N. A. *et al.* Superradiance in a system of proton spins. *Journal of Experimental and Theoretical Physics* **70**, 1128 (1990).

45. Cong, K. *et al.* Dicke superradiance in solids [Invited]. *Journal of the Optical Society of America B* **33**, C80 (2016).

46. Haake, F. *et al.* Macroscopic Quantum Fluctuations in Superfluorescence. *Phys Rev Lett* **42**, 1740–1743 (1979).

47. M. G. Benedict, A. M. Ermolaev, V. A. Malyshev, I. V. Sokolov & E. D. Trifonov. *Super-radiance: Multiatomic Coherent Emission*. (CRC Press , 2019).

48. Kumarakrishnan, A., Chudasama, S. & Han, X. Collision-induced superfluorescence. *Journal of the Optical Society of America B* **22**, 1538 (2005).

49. Skinner, J. L. & Hsu, D. Pure dephasing of a two-level system. *J Phys Chem* **90**, 4931–4938 (1986).

50. Flusberg, A., Mossberg, T. & Hartmann, S. R. Observation of Dicke superradiance at 1.30 μm in atomic Tl vapor. *Phys Lett A* **58**, 373–374 (1976).

51. Gross, M., Fabre, C., Pillet, P. & Haroche, S. Observation of Near-Infrared Dicke Superradiance on Cascading Transitions in Atomic Sodium. *Phys Rev Lett* **36**, 1035–1038 (1976).

52. Skribanowitz, N., Herman, P., Macgillivray, J. C. & Feld, M. S. *Observation of Dicke Superradiance in Optically Pumped HF Gas~*. vol. 30 (1973).

53. MacGillivray, J. C. & Feld, M. S. Theory of superradiance in an extended, optically thick medium. *Phys Rev A (Coll Park)* **14**, 1169–1189 (1976).

54. Heinzen, D. J., Thomas, J. E. & Feld, M. S. Coherent ringing in superfluorescence. *Phys Rev Lett* **54**, 677–680 (1985).

55. Burnham, D. C. & Chiao, R. Y. Coherent Resonance Fluorescence Excited by Short Light Pulses. *Physical Review* **188**, 667–675 (1969).

56. Bonifacio, R., Gronchi, M., Lugiato, L. A. & Ricca, A. M. Superfluorescence: Maxwell-Bloch Equations, Mean-Field Approach and CS Experiment. in *Coherence and Quantum Optics IV* 939–951 (Springer US, 1978). doi:10.1007/978-1-4757-0665-9_95.

57. Heinzen, D. J., Thomas, J. E. & Feld, M. S. Coherent Ringing in Superfluorescence. *Phys Rev Lett* **54**, 677–680 (1985).

58. Bonifacio, R., Schwendimann, P. & Haake, F. Quantum Statistical Theory of Superradiance. I. *Phys Rev A (Coll Park)* **4**, 302–313 (1971).

59. Bonifacio, R. & Lugiato, L. A. Cooperative radiation processes in two-level systems: Superfluorescence. II. *Phys Rev A (Coll Park)* **12**, 587–598 (1975).

60. Schuurmans, M. F. H. Superfluorescence and amplified spontaneous emission in an inhomogeneously broadened medium. *Opt Commun* **34**, 185–189 (1980).

61. Phuong, L. Q., Miyajima, K., Maeno, K., Itoh, T. & Ashida, M. Transitions from spontaneous emission to stimulated emission and superfluorescence of biexcitons confined in CuCl quantum dots. *J Lumin* **133**, 77–80 (2013).

62. Haake, F., Haus, J., King, H., Schröder, G. & Glauber, R. Delay-time statistics and inhomogeneous line broadening in superfluorescence. *Phys Rev Lett* **45**, 558–561 (1980).

63. Govind P. Agrawal. *Nonlinear Fiber Optics*. (Academic Press, 2019).

64. Milorad Cvijetic. *Optical Transmission Systems Engineering*. (Artech House , 2003).

65. Govind P. Agrawal. *Nonlinear Fiber Optics By*. (Elsevier Science, 2019).

66. He, Y. *et al.* Dispersion of the third-order optical nonlinearities in 2D (PEA)2PbI4 perovskite film. *Opt Express* **31**, 34292 (2023).

67. Ferrando, A., Martínez Pastor, J. P. & Suárez, I. Toward Metal Halide Perovskite Nonlinear Photonics. *J Phys Chem Lett* **9**, 5612–5623 (2018).

68. Findik, G. *et al.* High-temperature superfluorescence in methyl ammonium lead iodide. *Nat Photonics* **15**, 676–680 (2021).

CHAPTER 5: Conclusion and future work

So far, we have seen the varied nature of light emission in devices and films that make use of the different material properties and device architecture to impose certain boundary conditions that favor a particular kind of light emission.

We started with spontaneous emission in an OLED device and by making use of carefully fabricated nanostructures we demonstrated directional and polarized light emission. The basic principle behind the device was to suppress the lambertian air-mode and extract the trapped waveguide modes using the nanostructures. This was first of its kind device demonstration and such an architecture can be implemented in virtual reality display with the advantage being that it does not require additional and often bulky optical elements to achieve the same effect. However, due to the back-emitting nature of the OLED (BEOLED) the device suffers from some drawbacks. However subsequent works by group members L. Zhu, Q. Dong, and S. Yin significantly improved the primitive device design and achieved an impressive EQE and forward luminescence.

We then demonstrated multimode stimulated light emission in hybrid MHP gain media enclosed in a novel optical cavity that simultaneously combines a lateral DFB cavity as the primary oscillator and a transverse Fabry-Perot for improved mode confinement. The small mode volume increased the PDOS because of which efficient light amplification was achieved. Attributed to the prolonged photon lifetime in the cavity as demonstrated by the slope efficiency data and verified by FDTD simulation.

Eventually, we demonstrate control over the non-classical light behavior in perovskite in the form of Superfluorescence light emission, a coherent and stochastic cooperative phenomenon. Its implementation in application suffers due to the random nature of this emission, driven by ground state quantum fluctuations. However, by encapsulating the material in a ‘bad’ cavity we

were able to statistically manipulate the time evolution of the SF burst. On further analysis, the group delay dispersion effect of these ultrashort light pulses was quantified which depends on higher-order nonlinear behavior of the perovskite medium.

There are 2 research themes that would require further in-depth study and analysis:

1. SF in organic small molecules
2. Lasing in blended Quasi-2D perovskites

5.1. SF in organic small molecule

To test the presence of SF phase transition behavior in other emissive systems we performed a similar time-resolved analysis on a well-studied combination of small organic molecules 4,4′-Bis(N-carbazolyl)-1,1′-biphenyl (CBP) and 4,4'-Bis(9-ethyl-3-carbazovinylene)-1,1'-biphenyl (BCzVBi). CBP is the host material with 5% doping of the fluorescent BCzVBi emitter. The film was deposited using thermal co-evaporation in vacuum on a planar glass substrate.

Steady-state continuous wave (CW) PL and UV-VIS spectroscopy data in Figure 5.2 with the band-edge and the PL peak in the blue region of the visible spectra. CW pumping was performed using a 410 nm diode laser The multiple peaks in the CW PL spectra correspond to different exciplex energy states.[1] The lack of a PL signature from the CBP host indicates efficient resonant energy transfer in the film.[2]

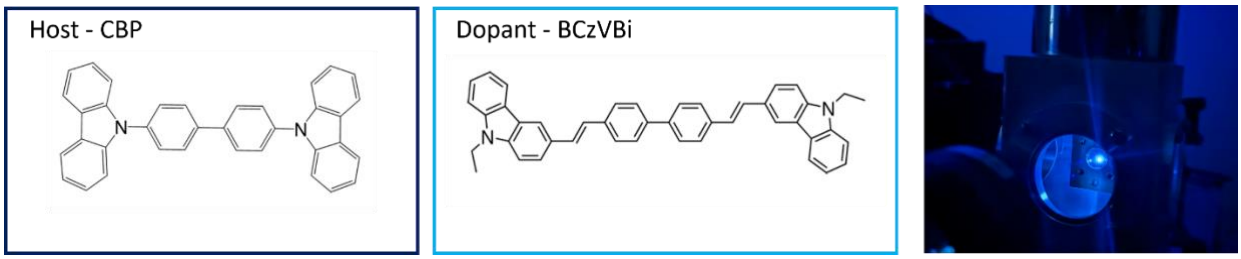

Figure 5.1: Shows the molecular structure of the host (CBP) and the dopant (BCzVBi) molecule. The two were thermally co-evaporated on a glass substrate with 5% doping ratio of the dopant molecule. A picture of the blue PL emission under laser excitation.

(a) (b)

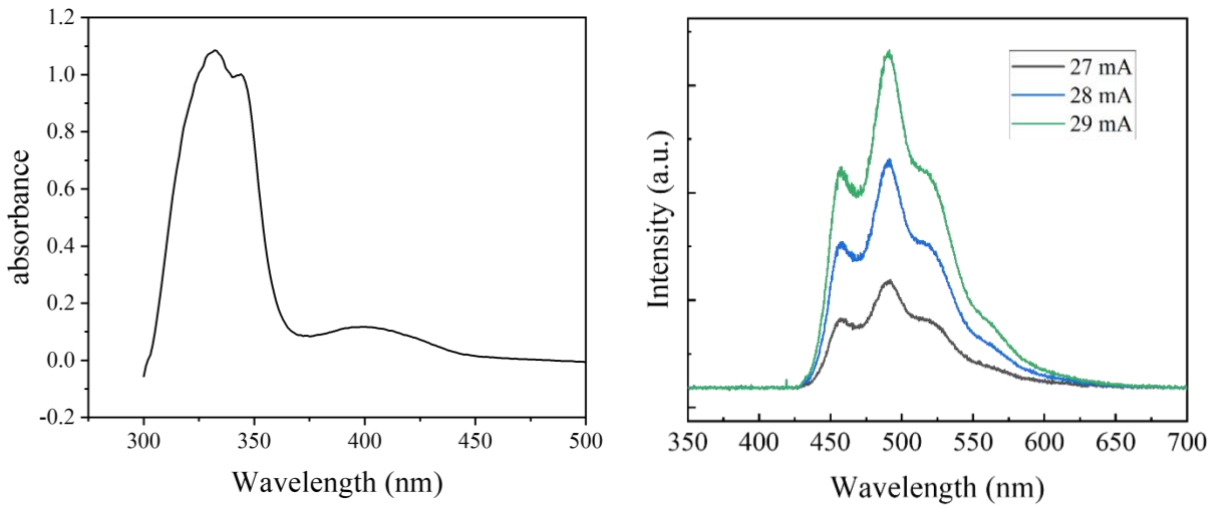

Figure 5.2: (a) UV-VIS spectra showing two dominant peaks corresponding to CBP at 330 nm and BCzVBi at 400 nm for 5% doping ratio of BCzVBi to CBP. (b) shows the CW excitation PL intensity as a function of the laser diode driving current. A 420 nm long pass filter was used to remove the 410 nm laser line.

Pulsed laser excitation was done using 400 nm pulses obtained from a frequency-doubled Ti-sapphire amplifier (Quantronix Integra-C; repetition rate, 1 kHz; central wavelength, 800 nm). As seen from Figure **5.3** there are obvious differences in the spectra when comparing it to CW

spectra in Figure 5.2b. The difference in the lineshape between CW and pulsed pumping is due to the density of the charge carrier generated using a highly intense pulsed pump causing inversion. The pulsed laser inverts the medium resulting in faster and efficient charge recombination with a nonlinear increase in intensity as a function of the excitation fluence as seen by the highlighted region of the spectra. Beginning from low excitation power, the peak at 475 nm undergoes blueshift as excitation power increases and eventually settles at 470 nm at 0.62 mW. We then performed time-resolved Kerr gate spectroscopy to track the time dynamics of this peak. In Figure 5.4a at excitation intensity just above the threshold, we see large signal undulation with respect to the background spontaneous emission an indication of SF phase transition. Meanwhile, at larger excitation intensity (Figure 5.4b) we see the characteristic delay time behavior with the signal appearing earlier in time as a function of increasing excitation intensity. Burnham-Chiao ringing can also be seen as the signal intensity rises corresponding to an increase in the coherent population participating in the SF process.

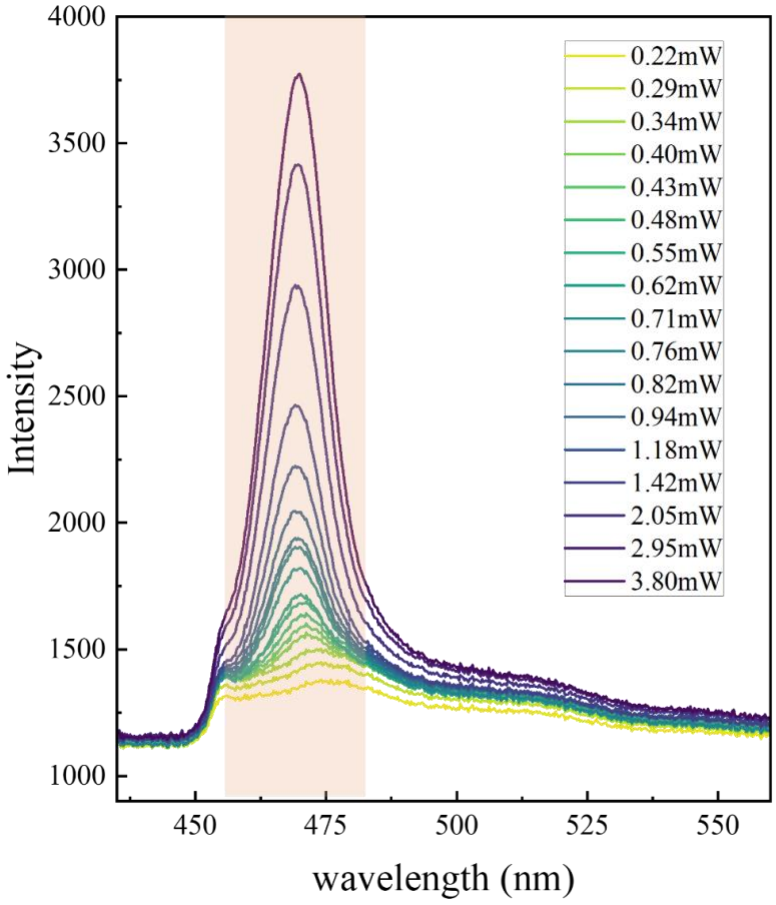

Figure 5.3: Pulsed laser PL spectra as a function of the excitation intensity. The highlighted region with a peak at 470 nm shows a non-linear increase in intensity while rest of the spectrum is pinned down and increases linearly. This abnormal increase in intensity is an indication of either SF or ASE process.

(a)

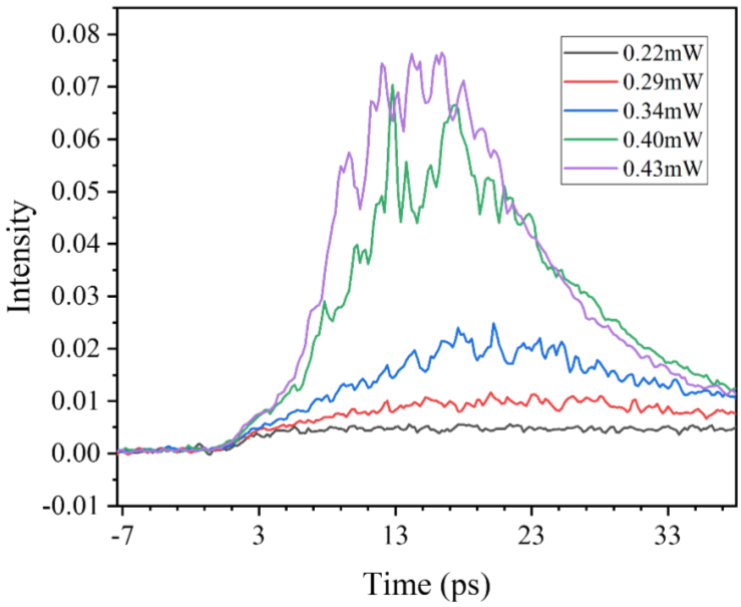

(b)

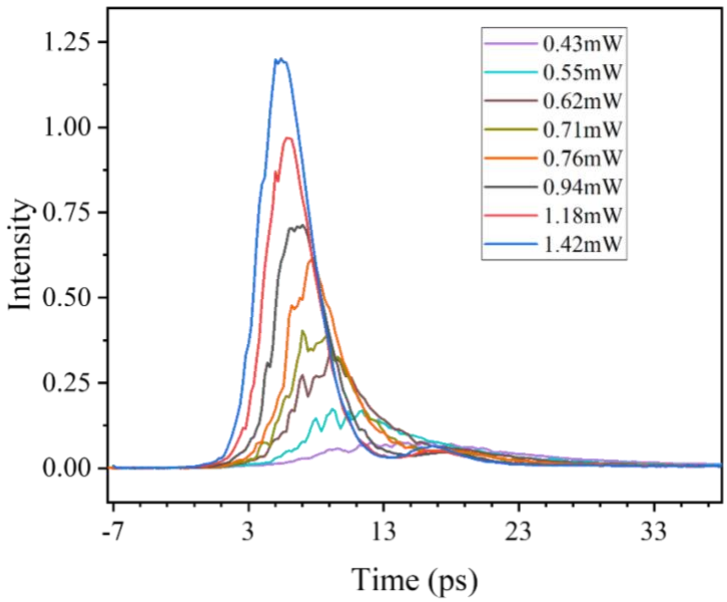

Figure 5.4: (a) Low-intensity Kerr data with spontaneous emission type exponential decay for an excitation power of 0.22 mW with clear signature of SF phase transition at powers greater than 0.34 mW. (b) shows high excitation power Kerr data with indication of reducing delay-time and increase in peak intensity

Additionally, to track the charge population of the claimed SF peak we also performed transient absorption measurement (TAS) and tracked their behavior as a function of time and

excitation intensity. As soon as the system is optically excited the charge carriers fill up the high-lying energy state as evident from charge charge-filling effect and since the emission is coherent the relaxation of the system by an SF burst is followed by almost complete depopulation of the charge carriers from the excited state.[3] We probe the corresponding SF peak population in Figure 5.5. At an excitation intensity of 0.10 mW, the time trace follows spontaneous emission behavior meanwhile at a slightly higher excitation density of 0.125 mW the population undergoes an abrupt drop in population after a certain waiting period. This waiting time has been speculated to be the time required for dipole synchronization to complete and is directly correlated to the delay-time.[4] This trend continues and is much more prominent at higher excitation density and follows well established semi-classical model for superfluorescent decay behavior.[5]

As seen from Kerr and the TAS data, most of the signatures indicating SF behavior are present but further analysis of the delay-time behavior and SF peak intensity is required to verify with confidence that the peak at 475 nm is indeed SF.

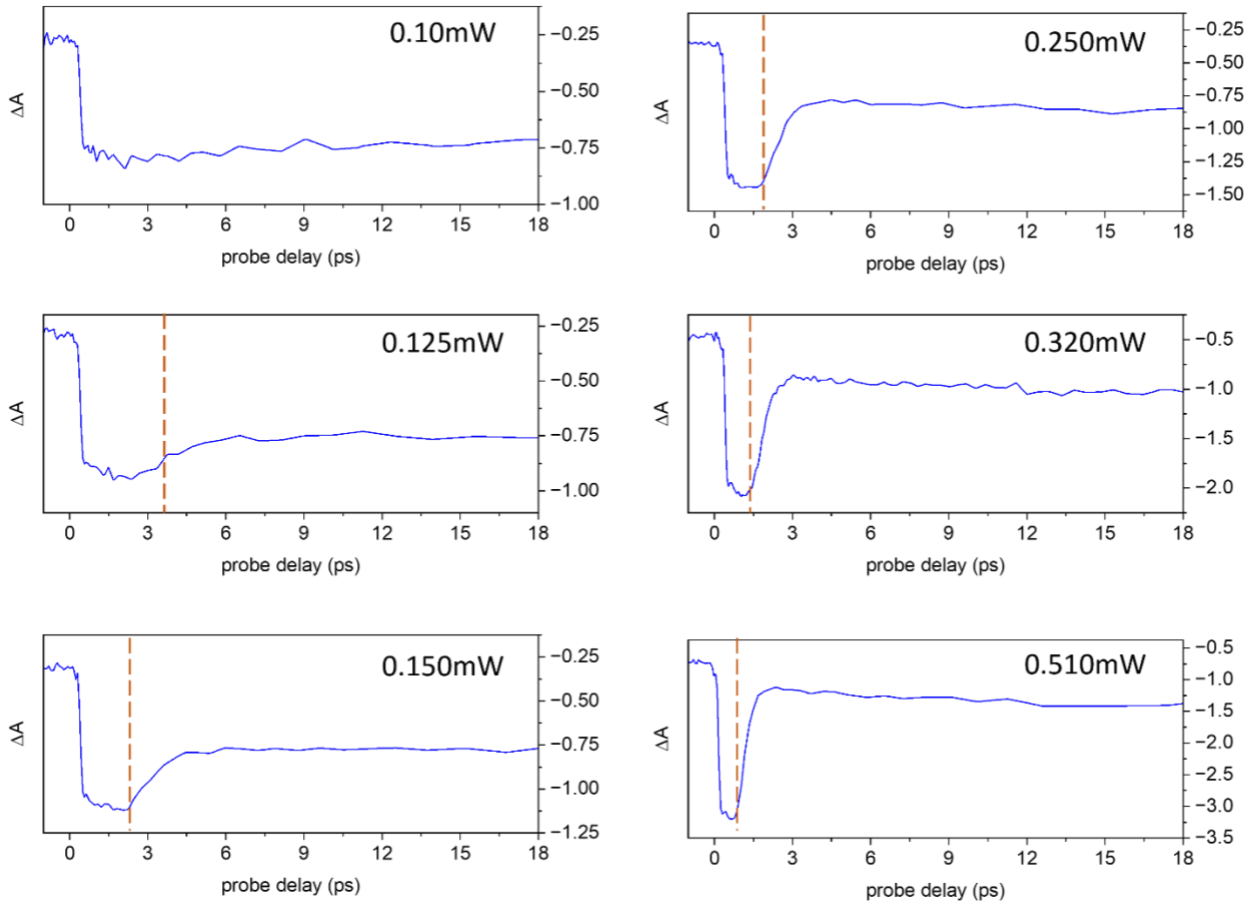

Figure 5.5: TAS intensity dynamics for the peak at 475 nm. At low excitation of 0.1 mW the dynamics follow spontaneous emission behavior. Starting at 0.125 mW we start seeing a phase transition to SF with an abrupt drop in intensity corresponding to complete to almost complete depletion of the excited state carriers.

5.2. Lasing in blended Quasi-2D perovskites

This project was part of a collaboration with Dr. Murali Gedda, postdoc in Prof. Thomas D. Anthopoulos at King Abdullah University of Science and Technology.

The objective of this project was to study the influence of small molecule additives on ASE performance of quasi-2D perovskites and eventually demonstrate lasing. Different domain dimensions of quasi-2D $PEA_2Cs_{n-1}Pb_nBr_{3n+1}$ were fabricated and blended with 0.25M ratio of 2,7-Dioctyl[1]benzothieno[3,2-b][1]benzothiophene (C8-BTBT) with respect to the Pb component in the film.

The superior light emission property of the blended films can be verified from the steady-state optical characterization as seen in Figure 5.6(c-d). The reason for the improved performance remains unconfirmed and requires further studies. However, we suspect that the addition of the small molecules improves the film orientation with respect to the substrate such that in-plane energy transfer between different phases becomes efficient. Based on the XRD data (Figure 5.7) the blended films show smaller FWHM and peak intensity and hence better crystallinity. The XRD plots for the neat films show an elevated background signal likely due to isotropic grain orientation. However, to confirm our hypothesis regarding the film's orientation Grazing-Incidence Wide-Angle X-ray Scattering (GIWAXS) needs to be performed.

We performed further optical studies to verify the light amplification capability of the two sets of samples under study and found that the blended films in general had a lower ASE threshold (Figure 5.8). To understand the effect of the small molecule additive it is critical to perform TAS measurements and analyze the charge dynamics and peak behavior of the various perovskite phases in the film.

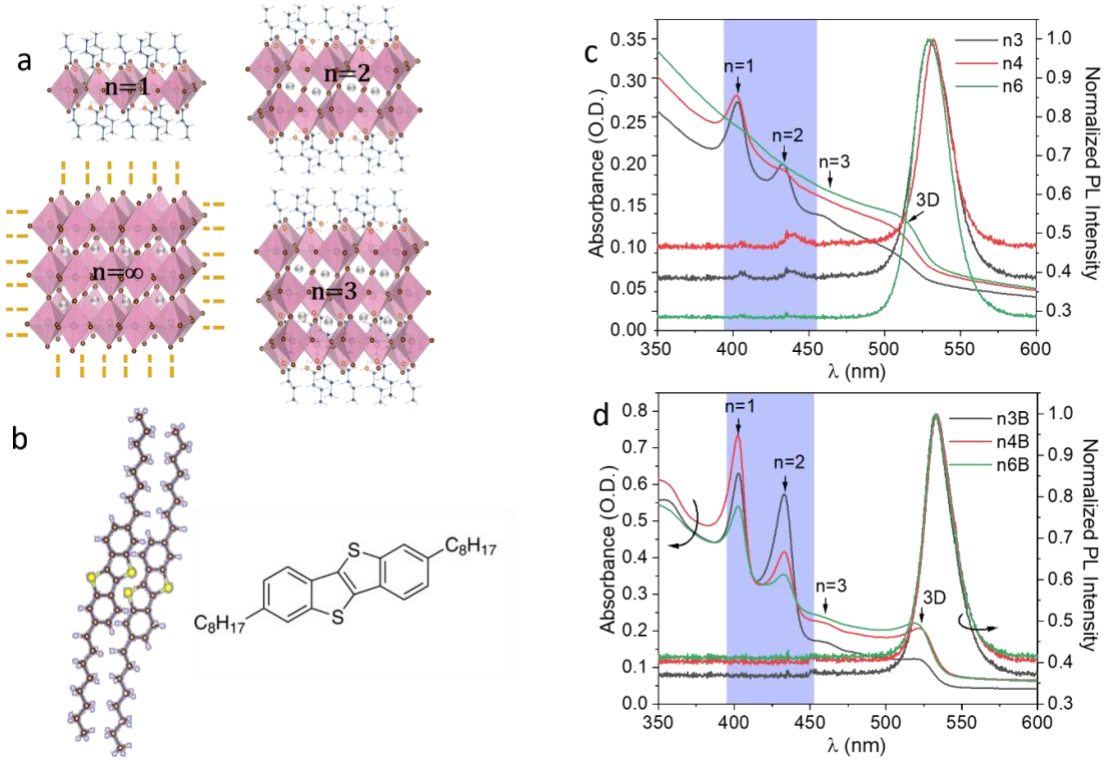

Figure 5.6: (a) shows the arrangement of the octahedral layer of quasi-2D perovskite and (b) shows the structure and molecular formula for C8-BTBT. (c) shows the PL and UV-VIS spectra of control films with film dimensionality n=3, n=4, and n=6 – hereafter noted as n3, n4, and n6. The lower dimensional phases are apparent from the UV-VIS data and their corresponding contribution to the PL. Much of the PL emission is from the 3D phase but the presence of lower dimensional phases in the spectrum implies sample inhomogeneity and inefficient charge funneling from lower to higher *n* phases. By blending the film with C8-BTBT (sample notation includes 'b' in the film's dimensionality) the sample dimensionality becomes homogeneous as proved by the lack of PL emission from lower dimensions. Also, from the UV-VIS data the oscillator strength or the binding energy increases resulting in higher radiative recombination efficiency

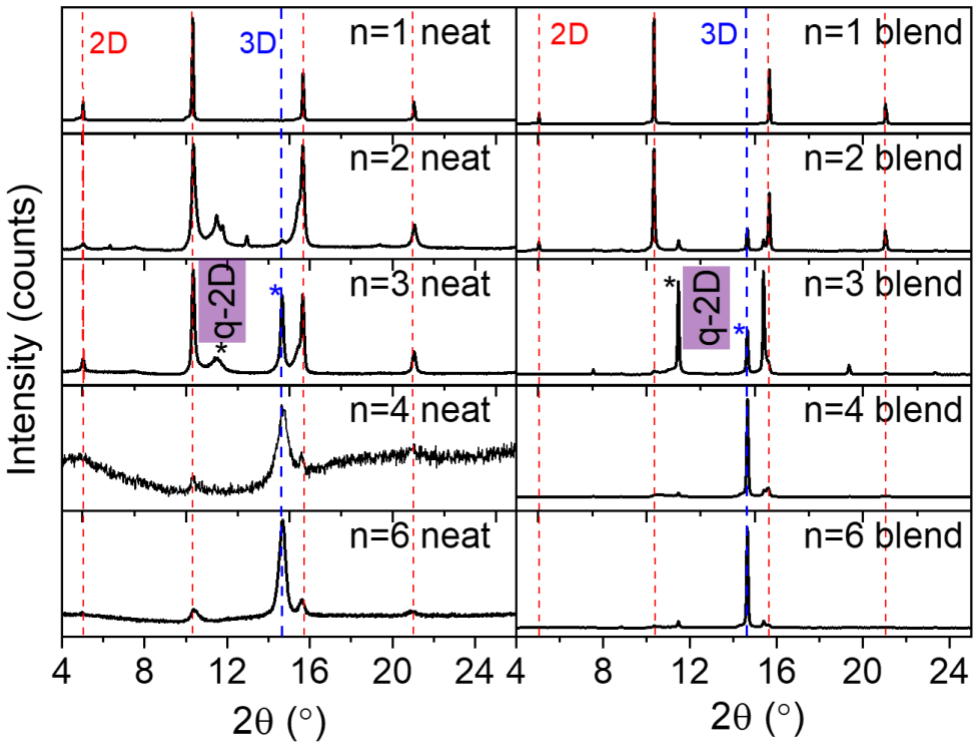

Figure 5.7: X-ray diffraction (XRD) data comparing the as prepared neat films (control) in the left column to the blended films in right column. As the layer number *n* increases, the 3D peak at 14.5º grows while the 2D peak at 10.2º slowly disappears as proof for the blended film transitioning to a more 3D nature while the 2D peaks in the neat films still have a significant contribution while the 3D peak has an inconsistent amorphous nature.

Figure 5.8: (a) - (c) and (d) - (f) evolution of the steady state PL spectra for differently engineered film dimensionality for the neat films and the blended films. All films show ASE secondary peak with differing threshold values (i)The blended films, in general, have a significantly lower threshold for ASE when compared to the neat films with the threshold increasing as the perovskite dimensionality increases. n=3 prepared film shows overall the lowest threshold for both the blend and the neat case. (g) The FWHM decreases as a function of the input excitation fluence and (h) the input-output curve for the n3B films shows a linear increase until the threshold after which the slope increases resulting in a kink in the integrated intensity curve.

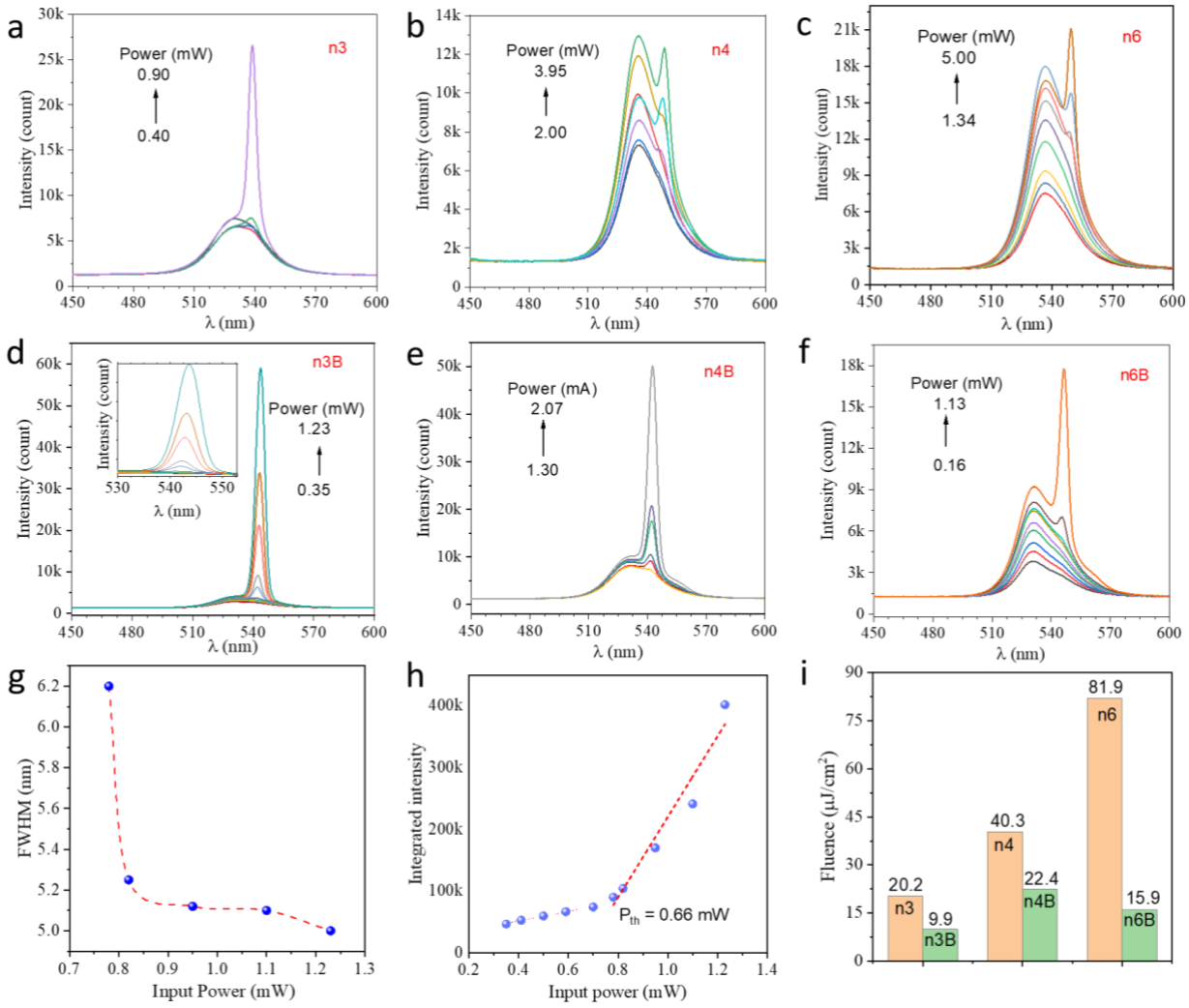
a
n3
Power (mW)
0.90
0.40
Intensity (count)
λ (nm)
b
n4
Power (mW)
3.95
2.00
c
n6
Power (mW)
5.00
1.34
d
n3B
Power (mW)
1.23
0.35
e
n4B
Power (mA)
2.07
1.30
f
n6B
Power (mW)
1.13
0.16
g
FWHM (nm)
Input Power (mW)
h
Integrated intensity
P_th = 0.66 mW
Input power (mW)
i
Fluence (μJ/cm²)
20.2
n3
9.9
n3B
40.3
n4
22.4
n4B
81.9
n6
15.9
n6B

5.3. References

1. Kim, N. H. *et al.* Color optimization of single emissive white OLEDs via energy transfer between RGB fluorescent dopants. *J Lumin* **143**, 723–728 (2013).

2. Song, W., Lee, I. & Lee, J. Y. Host Engineering for High Quantum Efficiency Blue and White Fluorescent Organic Light-Emitting Diodes. *Advanced Materials* **27**, 4358–4363 (2015).

3. Timothy Noe, G. *et al.* Giant superfluorescent bursts from a semiconductor magneto-plasma. *Nat Phys* **8**, 219–224 (2012).

4. Findik, G. *et al.* High-temperature superfluorescence in methyl ammonium lead iodide. *Nat Photonics* **15**, 676–680 (2021).

5. Bonifacio, R., Gronchi, M., Lugiato, L. A. & Ricca, A. M. Superfluorescence: Maxwell-Bloch Equations, Mean-Field Approach and CS Experiment. in *Coherence and Quantum Optics IV* 939–951 (Springer US, 1978). doi:10.1007/978-1-4757-0665-9_95.